CARDIOVASCULAR PHYSIOLOGY AND MEDICAL ASSESSMENTS: PHYSICS AND ENGINEERING PERSPECTIVES

EDITED BY: Dhanjoo Ghista, Kelvin Kian Loong Wong and Giancarlo Fortino
PUBLISHED IN: Frontiers in Physiology and Frontiers in Physics

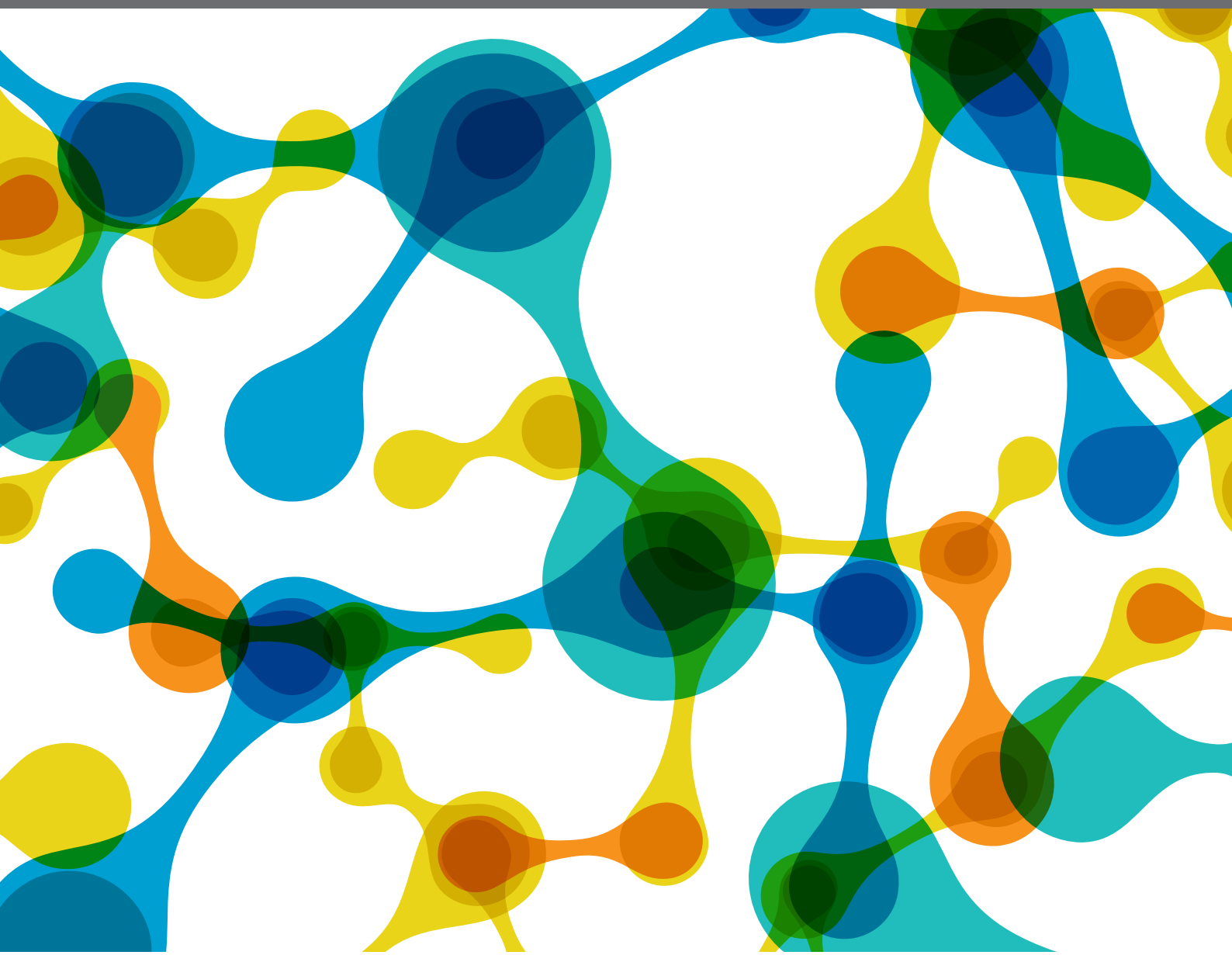

frontiers Research Topics

frontiers

ISSN 1664-8714
ISBN 978-2-88966-473-3
DOI 10.3389/978-2-88966-473-3

About Frontiers

Frontiers is more than just an open-access publisher of scholarly articles: it is a pioneering approach to the world of academia, radically improving the way scholarly research is managed. The grand vision of Frontiers is a world where all people have an equal opportunity to seek, share and generate knowledge. Frontiers provides immediate and permanent online open access to all its publications, but this alone is not enough to realize our grand goals.

Frontiers Journal Series

The Frontiers Journal Series is a multi-tier and interdisciplinary set of open-access, online journals, promising a paradigm shift from the current review, selection and dissemination processes in academic publishing. All Frontiers journals are driven by researchers for researchers; therefore, they constitute a service to the scholarly community. At the same time, the Frontiers Journal Series operates on a revolutionary invention, the tiered publishing system, initially addressing specific communities of scholars, and gradually climbing up to broader public understanding, thus serving the interests of the lay society, too.

Dedication to Quality

Each Frontiers article is a landmark of the highest quality, thanks to genuinely collaborative interactions between authors and review editors, who include some of the world's best academicians. Research must be certified by peers before entering a stream of knowledge that may eventually reach the public - and shape society; therefore, Frontiers only applies the most rigorous and unbiased reviews.
Frontiers revolutionizes research publishing by freely delivering the most outstanding research, evaluated with no bias from both the academic and social point of view. By applying the most advanced information technologies, Frontiers is catapulting scholarly publishing into a new generation.

What are Frontiers Research Topics?

Frontiers Research Topics are very popular trademarks of the Frontiers Journals Series: they are collections of at least ten articles, all centered on a particular subject. With their unique mix of varied contributions from Original Research to Review Articles, Frontiers Research Topics unify the most influential researchers, the latest key findings and historical advances in a hot research area! Find out more on how to host your own Frontiers Research Topic or contribute to one as an author by contacting the Frontiers Editorial Office: frontiersin.org/about/contact

CARDIOVASCULAR PHYSIOLOGY AND MEDICAL ASSESSMENTS: PHYSICS AND ENGINEERING PERSPECTIVES

Topic Editors:
Dhanjoo Ghista, Other, United States
Kelvin Kian Loong Wong, University of Adelaide, Australia
Giancarlo Fortino, University of Calabria, Italy

Citation: Ghista, D., Wong, K. K. L., Fortino, G., eds. (2021). Cardiovascular Physiology and Medical Assessments: Physics and Engineering Perspectives. Lausanne: Frontiers Media SA. doi: 10.3389/978-2-88966-473-3

Table of Contents

frontiers in Physics

EDITORIAL
published: 19 January 2021
doi: 10.3389/fphy.2020.626302

Editorial: Cardiovascular Physiology and Medical Assessments: Physics and Engineering Perspectives

Kelvin K. L. Wong[1]*, *Dhanjoo Ghista*[2] and *Giancarlo Fortino*[3]

[1]School of Electrical and Electronic Engineering, University of Adelaide, Adelaide, SA, Australia, [2]University 2020 Foundation, San Jose, CA, United States, [3]University of Calabria, Cosenza, Italy

Keywords: hemodynamics, physics and engineering perspectives, cardiovascular physiology, medical assessments, blood flow analysis

Editorial on the Research Topic

Cardiovascular Physiology and Medical Assessments: Physics and Engineering Perspectives

Physics and Engineering perspective plays an important role in cardiovascular physiology and medical assessments. It utilizes the theory of physics and engineering to carry out physiological analysis, detect physiological dysfunction, diagnose disease, and guide remedial surgery. The medical physics and engineering field has enabled a more in depth understanding of cardiovascular physiology.

Let us start with 'Neural Regulation of Cardiac function,' which is carried out by the sympathetic and parasympathetic divisions of the autonomic nervous system. The sympathetic nerves to the heart are facilitatory, whereas the parasympathetic nerves are inhibitory; in certain regions of the heart, such as the ventricular myocardium, the effects of the sympathetic division are more dominant. The mechanisms of neural regulation of the heart can be investigated into, extending from regulation of heart rate in regular activity and heart rate variability in athletic manoeuvres, to reperfusion of the ischemic myocardial tissue.

Then in 'Bioelectrical Process in the Heart' the electrical activity is initiated in the SA node, and the impulse spreads throughout the atria via specialized internodal pathways, to the atrial myocardial contractile cells and the atrioventricular node. From the AV node, the electrical impulse spreads through the bundle of His, bundle branches, and Purkinje fibres to myocardial contractile cells in the ventricles, causing ventricular contractility for initiating left ventricular ejection. This bioelectrical activity is characterized by electrocardiography (ECG), and its signal processing enables cardiac diagnostics.

Now let us discuss 'Cardiac Perfusion.' For computing intra-myocardial blood flow velocity and pressure patterns, we can carry out myocardial perfusion SPECT imaging, prescribe the myocardial conductivity, and then do intra-myocardial flow analysis to determine the blood pressure and velocity distributions in myocardial segments. In this way, we can quantify decreased blood flow in the ischemic areas of the myocardium, which can lead to decreased ventricular contractility.

Finally, let us enter the left ventricle. Therein, 'assessment of subjects at risk of heart failure' is carried out by means of the governing equations of fluid flow, by which we can determine the flow patterns of velocity and pressure distribution in the left ventricle (LV), and thereby show how if adequate pressure is generated to open the aortic valve. For this purpose, we can use the vector flow mapping technique to generate flow velocity vector fields, by post-processing the colour doppler echo images. This information is then transferred to monitors in real time, in order to visualize abnormal flow patterns and to guide cardiologists in their diagnosis [1].

OPEN ACCESS

Edited and reviewed by:
Ewald Moser,
Medical University of Vienna, Austria

***Correspondence:**
Kelvin K. L. Wong
kelvin.wong@ieee.org

Specialty section:
This article was submitted to Medical Physics and Imaging, a section of the journal Frontiers in Physics

Received: *05 November 2020*
Accepted: *27 November 2020*
Published: *19 January 2021*

Citation:
Wong KKL, Ghista D and Fortino G (2021) Editorial: Cardiovascular Physiology and Medical Assessments: Physics and Engineering Perspectives. Front. Phys. 8:626302. doi: 10.3389/fphy.2020.626302

This special issue focuses on how breakthroughs in physics and engineering have helped us to advance the understanding of cardiovascular physiology, and to make it more quantitative for the purpose of medical assessment [2]. Herein, we are providing a quantitative format of cardiovascular physiology and its medical assessment, based on physics and engineering perspective. This issue has four research articles, and we will now present the features of the papers.

In the first paper, 'Carotid Stiffness Assessment with Ultrafast Ultrasound Imaging in Case of Bicuspid Aortic Valve,' Goudot et al. have focused on the carotid stiffness assessment in the case of bicuspid aortic valve (BAV) by using ultrafast ultrasound imaging. Ultrasound imaging is the perfect follow-up implement for BAV patients, because of its radiation free technology, and its cost-effectiveness. Ultrafast ultrasound imaging (UF) permits show of the fit tissue movement at high time-related resolution, by utilizing plane wave transmitted with different tendency and a testing rate over 1,000 frames/s [3]. Then, Ultrafast Doppler acquired by processed data precisely evaluate the tissue velocities [4]. In this paper, they have compared the carotid flow parameters and carotid stiffness based on UF, in BAV patients and healthy subjects. Meanwhile, the deformation of the carotid arterial breadth during the cardiac cycle was described by UF-Doppler imaging. They measured the arterial distensibility, the maximal rate of systolic distension (MRSD), and wall shear stress (WSS). The computation of WSS was based on analysing the blood flow velocities near the carotid walls. A key point of the arterial wall remodelling is hemodynamic assessment of blood flow [5]. The absence of WSS alteration in the BAV patients could also clarify the lack of stiffness variation of the carotid wall. The specific morphology of the BAV could lead to the WSS modifications in the ascending aorta, with increased possibility of degenerative lesions observed in the aortic wall [6]. Compared with healthy subjects, it is remarkable that the carotid flow parameters and carotid stiffness are not changed in the case of BAV.

In recent years, many investigations have combined separate sensor sorts for pulse wave acquisition, such as pulse wave from the left forefinger, wrist, and second toe arteries. Although all these devices can detect and record arterial pulse waves, their operating modes and sensitivities are different, resulting in different shapes and timings of the pulse waves, leading to changes in diagnostic efficiency [7]. In the second paper, 'Quantitative Comparison of the Performance of Piezoresistive, Piezoelectric, Acceleration, and Optical Pulse Wave Sensors,' Wang et al. have compared and analyzed the radial, carotid, arterial femoral and digital signals under a series of conditions (three levels of contact force: light, medium, and heavy) and they used various pulse sensors to help make wise choices of the appropriate type sensor signals for recording arterial pulse waves. From the existing sensor types, they chose four: a piezoresistive strain gauge sensor (PESG) and a piezoelectric Millar tonometer (the first mentioned of two has the ability to scale contact force), a rounded diaphragm acceleration sensor, and an light reflection sensor. Thse four sensors were used to record the pulse wave signals of the left radial artery, carotid artery, femoral artery and digital artery of 60 subjects. In their studies, they found that the impact of contact pressure, measurement location, and ambient light on the pulse wave should be taken into account when monitoring the patients. Secondly, by comparing the four pulse wave sensors, it is found that the performance of the tonometer is the best, followed by the accelerometer, followed by PESG, and the optical sensor being the worst. Finally, there was significant difference among the four sensors in their waveform shapes and the timing of the arterial pulse wave and amplitude parameters. So in practice, different sensor types could be used, perhaps in combination according to the measurement site and the nature of the required signal analysis and in this way, the advantages of each can be better utilized.

The third paper is 'Topologic and Hemodynamic Characteristics of the Human Coronary Arterial Circulation,' authored by Schwarz et al. A fitting perception of the complex interplay of various factors contributing to coronary arterial flow needs a quantitative method based on the characteristics of the coronary network. Therefore, the purpose of their work is aimed at contributing a comprehensive quantification of the partial feature of the human coronary circulation. They employed a high-resolution imaging cryomicrotome to alternately cut and block-face the imaged frozen heart for 3D reconstruction of the left coronary circulation, and then analysed the flow in geometric topological, and topographic properties. Their model describes the flow at bifurcations of the vessel diameter. They have presented a method that dealt with the wide range of data on the partial features, to comopute the hemodynamics. Their findings set the stage for further research, containing structural conversion, integration of vasomotor responsiveness, and their effects on the supply to the left ventricle for its health maintenance.

The incidence of aortic dissection markedly increases with atherosclerosis and hypertension [8]. D-dimer, a specific degradation product of cross-linked fibrin, represents the coagulation and fibrinolytic system activation [9]. It is now commonly used in the diagnosis of pulmonary embolism [10], deep vein thrombosis [11], acute coronary syndrome [12], and acute aortic dissection [9,13,14]. The fourth paper, 'Association Between D-dimer and Early Adverse Events in Patients With Acute Type A Aortic Dissection Undergoing Arch Replacement and the Frozen Elephant Trunk Implantation: A Retrospective Cohort Study,' authored by Liu et al. is aimed to investigate the association between D-dimer levels and 90-day postoperative adverse events in patients undergoing arch replacement and frozen elephant trunk (FET), by using a multivariate Cox regression model containing all known associated major perioperative predictors. They have retrospectively analyzed the data of patients with acute type A aortic dissection undergoing aortic arch surgery and FET, from July 2017 to December 2018 at Beijing Anzhen Hospital. The D-dimer levels were evaluated within 24 h of admission. A total of 347 patients were included in the study. The median D-dimer level was 1.95 μg/ml (interquartile range, 0.77–3.16 μg/ml). The multivariable Cox regression analysis revealed that D-dimer level was independently associated with 90-day postoperative adverse events, after adjustment for confounding factors

(hazard ratio = 1.19 per 10 μg/ml increase in D-dimer, 95% confidence interval: 1.01–1.41; P = 0.039). The Kaplan–Meier analysis revealed that the highest tertile (median 6.27 μg/ml) had more 90-day postoperative adverse events, compared with the median and lowest tertiles (P = 0.0014). Their results showed that increased D-dimer levels at admission were associated with 90-day postoperative adverse events in patients with type A aortic dissection undergoing arch surgery with FET. This indicates that such high-risk patients deserve close medical monitoring.

In summary, these four interesting papers have focused on current state-of-the-art advances in physics and engineering perspective in cardiovascular physiology and medical assessment. Their results provide readers with valuable information on the application of the theory of physics and engineering in cardiovascular physiology and medical assessments. We hope that this special issue will provide a platform for researchers and clinical physicians to collaborate on some research areas with the aim of promoting a more scientific medical study of cardiovascular physiology.

AUTHOR CONTRIBUTIONS

KW collection, organizing, and review of the literature; DG and GF preparing the manuscript, and manuscript review and modification.

FUNDING

This work was funded by National Natural Science Foundation of China (Grant No. 81771927).

REFERENCES

1. Wong K, Fortino G, Abbott D. Deep learning-based cardiovascular image diagnosis: a promising challenge. *Future Gener Comput Syst* (2020) 110:802–11. doi:10.1016/j.future.2019.09.047
2. Piccialli F, Somma VD, Giampaolo F, Cuomo S, Fortino G. A survey on deep learning in medicine: why, how and when? *Information Fusion* (2021) 66: 111–37. doi:10.1016/j.inffus.2020.09.006
3. Tanter M, Fink M. Ultrafast imaging in biomedical ultrasound. *IEEE Trans Ultrason Ferroelectr Freq Control* (2014) 61:102–19. doi:10.1109/TUFFC.2014.6689779
4. Bercoff J, Montaldo G, Loupas T, Savery D, Mézière F, Fink M, et al. Ultrafast compound doppler imaging: providing full blood flow characterization. *IEEE Trans Ultrason Ferroelectr Freq Control* (2011) 58:134–47. doi:10.1109/TUFFC.2011.1780
5. Yassine NM, Shahram JT, Body SC. Pathogenic mechanisms of bicuspid aortic valve aortopathy. *Front Physiol* (2017) 8:687. doi:10.3389/fphys.2017.00687
6. Guzzardi DG, Barker AJ, Van Ooij P, Malaisrie SC, Puthumana JJ, Belke DD, et al. Valve-related hemodynamics mediate human bicuspid aortopathy: insights from wall shear stress mapping. *J Am Coll Cardiol* (2015) 66: 892–900. doi:10.1016/j.jacc.2015.06.1310
7. Zuo W, Wang P, Zhang D. Comparison of three different types of wrist pulse signals by their physical meanings and diagnosis performance. *IEEE J Biomed Health Inform* (2016) 20:119–27. doi:10.1109/JBHI.2014.2369821
8. Martens A, Beckmann E, Kaufeld T, Umminger J, Fleissner F, Koigeldiyev N, et al. Total aortic arch repair: risk factor analysis and follow-up in 199 patients. *Eur J Cardio-Thorac* (2016) 50:940–8. doi:10.1093/ejcts/ezw158
9. Suzuki T, Distante A, Zizza A, Trimarchi S, Villani M, Counselman F, et al. Diagnosis of acute aortic dissection by D-Dimer. *Circulation* (2009) 119:2702–7. doi:10.1161/CIRCULATIONAHA.108.833004
10. van der Hulle T, den Exter PL, Erkens PGM, van Es J, Mos ICM, Ten Cate H, et al. Variable D-dimer thresholds for diagnosis of clinically suspected acute pulmonary embolism. *J Thromb Haemost* (2013) 11:1986–92. doi:10.1111/jth.12394
11. Faller N, Limacher A, Méan M, Righini M, Aschwanden M, Beer JH, et al. Predictors and causes of long-term mortality in elderly patients with acute venous thromboembolism: a prospective cohort study. *Am J Med* (2017) 130: 198–206. doi:10.1016/j.amjmed.2016.09.008
12. Bayes-Genis A, Mateo J, Santaló M, Oliver A, Guindo J, Badimon L, et al. D -Dimer is an early diagnostic marker of coronary ischemia in patients with chest pain. *Am Heart J* (2000) 140:379–84 doi:10.1067/mhj.2000.108823
13. Akutsu K, Sato N, Yamamoto T, Morita N, Takagi H, Fujita N., et al. A rapid bedside D-dimer assay (cardiac D-dimer) for screening of clinically suspected acute aortic dissection. *Circ J* (2005) 69:397–403. doi:10.1253/circj.69.397
14. Shao N, Xia S, Wang J, Zhou X, Huang Z, Zhu W, et al. The role of D-dimers in the diagnosis of acute aortic dissection. *Mol Biol Rep* (2014) 41:6397–403. doi:10.1007/s11033-014-3520-z

Conflict of Interest: The authors declare that the research was conducted in the absence of any commercial or financial relationships that could be construed as a potential conflict of interest.

frontiers in Physiology

ORIGINAL RESEARCH
published: 23 October 2019
doi: 10.3389/fphys.2019.01330

Carotid Stiffness Assessment With Ultrafast Ultrasound Imaging in Case of Bicuspid Aortic Valve

Guillaume Goudot[1,2], Tristan Mirault[1,2,3], Lina Khider[1,2], Olivier Pedreira[1], Charles Cheng[2,3], Jonathan Porée[1], Maxime Gruest[1], Xavier Jeunemaître[2,3], Mathieu Pernot[1] and Emmanuel Messas[2,3]**

[1] Physics for Medicine Paris, INSERM U1273, ESPCI Paris, CNRS FRE 2031, PSL Research University, Paris, France, [2] VASC European Research Network, Centre de Référence des Maladies Vasculaires Rares, Hôpital Européen Georges-Pompidou, AP-HP, Paris, France, [3] INSERM U970 PARCC, Paris Descartes University – USPC Sorbonne Paris Cité University, Paris, France

Aims: To compare the carotid stiffness and flow parameters by ultrafast ultrasound imaging (UF), in bicuspid aortic valve (BAV) patients to first-degree relatives (controls).

Methods: BAV patients (n = 92) and controls (n = 48) were consecutively included at a reference center for BAV. Aortic valve and ascending aorta were evaluated by echocardiography. Common carotid arteries were evaluated by UF with a linear probe. A high frame rate (2,000 frames/s) was used to measure the pulse wave velocity (PWV). The arterial diameter change over the cardiac cycle was obtained by UF-Doppler imaging. This allowed us to measure the distensibility and the maximal rate of systolic distension (MRSD). The wall shear stress (WSS) was measured based on the same acquisitions, by analyzing blood flow velocities close to the carotid walls.

Results: BAV patients had significantly larger aortic diameters ($p < 0.001$) at the Valsalva sinus and at the tubular ascending aorta but no larger carotid diameters. No significant differences were found in carotid stiffness parameters (distensibility, MRSD, and PWV), even though these patients had a higher aortic stiffness. Carotid stiffness correlated linearly with age and similar slopes were obtained for BAV patients and controls. No difference in carotid WSS was found between BAV patients and controls.

Conclusion: Our results clearly show that the carotid stiffness and flow parameters are not altered in case of BAV compared with controls.

Keywords: bicuspid aortic valve, arterial stiffness, ultrafast ultrasound imaging, carotid, wall shear stress

OPEN ACCESS

Edited by:
Kelvin Kian Loong Wong,
The University of Adelaide, Australia

Reviewed by:
Simon Auguste Lambert,
Université Claude Bernard Lyon 1, France
Wazir Muhammad,
Yale University, United States

****Correspondence:***
Guillaume Goudot
guillaume.goudot@aphp.fr
Emmanuel Messas
emmanuel.messas@aphp.fr

Specialty section:
This article was submitted to Medical Physics and Imaging, a section of the journal Frontiers in Physiology

Received: *19 May 2019*
Accepted: *04 October 2019*
Published: *23 October 2019*

Citation:
Goudot G, Mirault T, Khider L, Pedreira O, Cheng C, Porée J, Gruest M, Jeunemaître X, Pernot M and Messas E (2019) Carotid Stiffness Assessment With Ultrafast Ultrasound Imaging in Case of Bicuspid Aortic Valve. Front. Physiol. 10:1330. doi: 10.3389/fphys.2019.01330

INTRODUCTION

Bicuspid aortic valve (BAV) is associated with alterations of the aortic wall that lead to a higher risk of aortic aneurysm and acute aortic events (Verma and Siu, 2014). The decision to replace the ascending aorta by prophylactic surgery is currently only based on the aortic diameter (Aboyans et al., 2017). Due to early histological changes in the aortic wall, particularly affecting elastin fibers, it has been suggested that aortic stiffness may be a prognostic marker of dilatation (Nistri et al., 2008; Aquaro et al., 2017; Goudot et al., 2019a). The involvement of common carotid arteries in the aortic remodeling process in case of BAV remains controversial. Carotid dissections seem

indeed to be part of the BAV spectrum (Schievink and Mokri, 1995) and Li et al. (2016) found a reduced arterial distensibility at the common carotid artery site. This finding was not confirmed by Santarpia et al. (2012) nor, more recently, by Kim et al. (2017) using tissue Doppler velocities. Nevertheless, common carotid arteries share a common embryological origin with the ascending aorta from the neural crest (Le Lièvre and Le Douarin, 1975; Majesky, 2007). More accessible to ultrasound imaging, their evaluation could therefore constitute a useful prognostic marker to predict acute aortic syndromes. More explorations are, however, required to ascertain the presence of a "carotidopathy" associated with the BAV.

Ultrasound imaging is the ideal tool for the follow-up of patients with BAV, due to its availability, its low cost, and its radiation free technology. Ultrafast ultrasound imaging (UF), using plane wave transmits with multiple inclinations and a sampling rate over 1,000 frames/s, allows to display the fine tissue displacements at high temporal resolution (Tanter and Fink, 2014) and Ultrafast Doppler, obtained by post-processing the same data, estimates precisely the tissue velocities (Bercoff et al., 2011). This new imaging modality gives access to local parameters of arterial stiffness, such as the pulse wave velocity (PWV) and the arterial wall distensibility. The PWV measurement with UF was initially presented and validated *in vivo* in healthy volunteers by Couade et al. (2011). A good agreement with other techniques was then established: distensibility using a high-resolution echo-tracking device (MyLab 70, ART. LAB, Esaote, Italy) (Marais et al., 2019) and the carotid-femoral PWV obtained by SphygmoCor® (Mirault et al., 2015).

New biomarkers developed with UF, such as arterial stiffening over the cardiac cycle, may also help better define the arterial phenotype, as it has been done in the case of vascular Ehlers-Danlos syndrome (Mirault et al., 2015; Goudot et al., 2018).

In this work, we aimed at evaluating the changes in carotid biomechanical properties associated with BAV. We also evaluated the influence of the wall shear stress. As systematic screening of BAV in the family of the patient is performed in our center, we collected data from non-BAV relatives using the same protocol. This method allowed us to compare cases with controls sharing the same genetic background but without BAV.

MATERIALS AND METHODS

Population

This study is a cross-sectional study of 140 consecutive patients undergoing dedicated consultation, between December 2017 and December 2018 at the European hospital Georges-Pompidou, a reference center for BAV disease. Patients with BAV have been prospectively evaluated at the National Reference Centre for Rare Vascular Diseases in a dedicated consultation. First-degree healthy relatives, i.e., with a tricuspid aortic valve, were used as controls. The ethical committee approved this study and patients signed a written informed consent form (CPP Île-de-France VI, n°2017-A01508-45). Confirmation of BAV was retained in case of the short-axis view of the aortic valve with the presence of only two functional cusps. First-degree relatives were also prospectively included and were considered as controls if a tricuspid aortic valve was found. In case of doubt about the diagnosis, the cardiac ultrasound loops were proofread by an expert physician, and a cardiac magnetic resonance imaging (MRI) was requested to evaluate the morphology of the aortic valve more precisely.

Transthoracic Cardiac Ultrasound

Transthoracic echocardiography was performed using commercial available equipment [IU22®, S5-1 (5–1 MHz; 80 elements) probe, Philips Medical Systems©, Andover, MA, United States]. Analysis of the aortic valve and the ascending aorta was systematically performed following a dedicated protocol previously published (Goudot et al., 2019b).

Carotid Wall Ultrafast Ultrasound Imaging

Bilateral evaluation of common carotid arteries by UF was performed using an Aixplorer© device (Supersonic Imagine©, Aix-en-Provence, France) and a linear probe (15–4 MHz, 256 elements, 0.2 mm pitch). The ultrafast acquisition was carried out using plane wave successively emitted at three tilted angles (–5°, 0°, and 5°), with a frame rate of 2,000 s^{-1}. The acquisitions duration was 507 ms, and was triggered at the start of the QRS. The maximum depth of the image, between 10 and 40 mm was set by the operator, depending on the image obtained with conventional B-mode. Data analysis was performed using MatLab® software (Version R2013b, The MathWorks©, Natick, MA, United States). For each transmitted plane wave, the backscattered ultrasonic echoes were recorded and assembled to reconstitute the 2D image using conventional delay-and-sum beamforming and spatial compounding (Montaldo et al., 2009). Tissue Doppler velocities (**Figure 1A**) were obtained at each point of the image at a high frame rate (Movie in **Supplementary Video S1**). The anterior and posterior walls of the acquisitions of adequate quality were manually segmented by an independent observer, following the signal of the carotid wall on the B-mode image obtained with UF (**Supplementary Figure S1**). From the initial manual delimitation of the carotid artery, the arterial diameter variation rate curve was automatically determined by calculating the difference in tissue Doppler velocities between the anterior and posterior walls over the cardiac cycle. The arterial diameter variation curve was then obtained from temporal integration of the variation rate during the cardiac cycle (**Figure 2A**).

Distensibility

Carotid distensibility was calculated according to the following formula:

$$Dist = 2 \times \frac{SD - DD}{DD \times (SBP - DBP)}$$

Dist, Distensibility ($mmHg^{-1}$); SD, Systolic diameter (mm); DD, Diastolic diameter (mm); SBP, Systolic blood pressure (mmHg); and DBP, Diastolic blood pressure (mmHg).

An oscillometric device measured brachial blood pressure. Measurements were performed on both arms and the higher

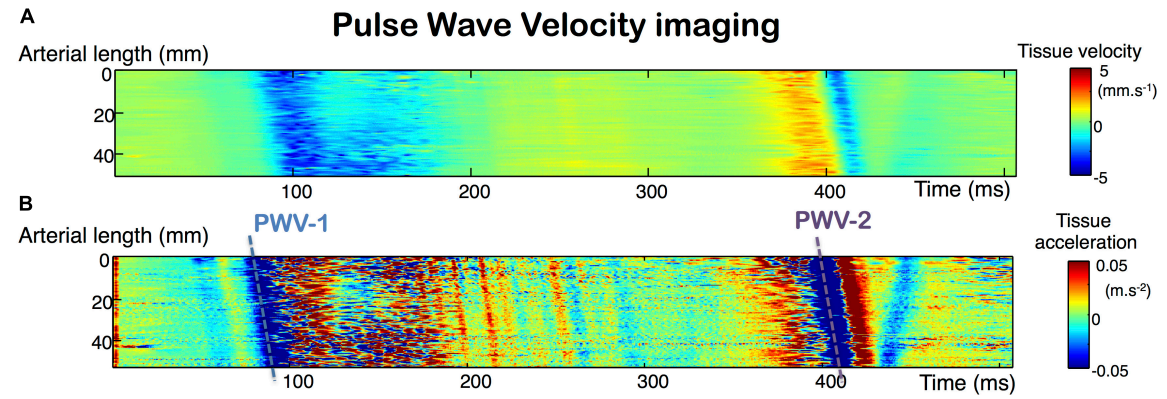

FIGURE 1 | Ultrafast tissue Doppler imaging along the arterial wall over the cardiac cycle. Analysis of the tissue Doppler velocities of the arterial walls over time provides access to pulse wave velocity (PWV) measurements **(A)**. The measurement is obtained by the automated calculation of the slope of the main tissue Doppler acceleration peaks **(B)**.

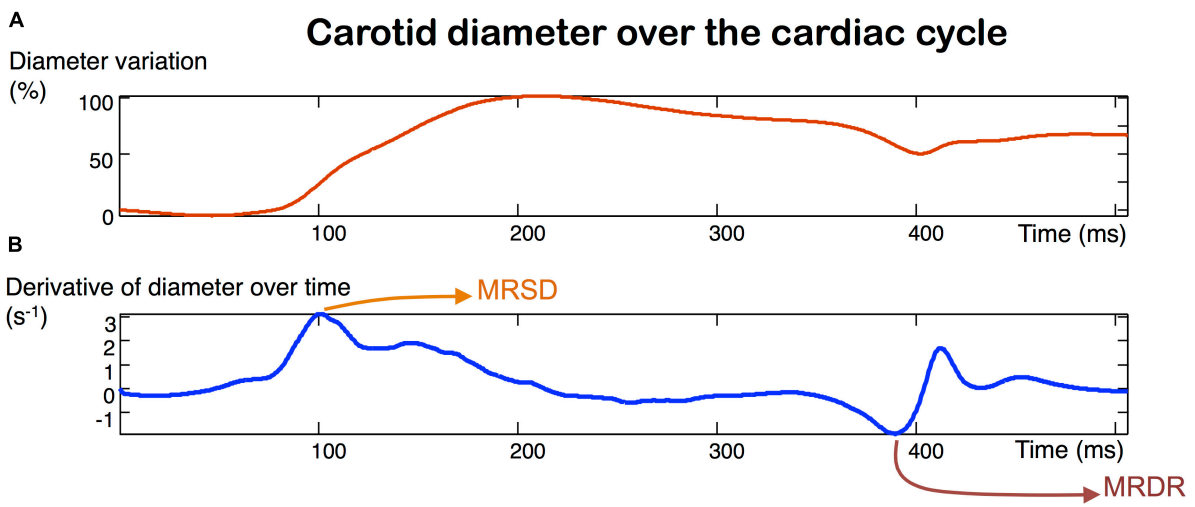

FIGURE 2 | Carotid strain obtained with ultrafast ultrasound imaging **(A)**. MRSD (maximum rate of systolic distension) and MRDR (maximum rate of diastolic recoil) **(B)** are derived from the measurement of the diameter variation over time.

value was selected. The diameter variation curve was obtained at each transversal section of the artery.

Pulse Wave Velocity (PWV)

The time shift of the diameter variation curve from the proximal part of the carotid to the distal part allowed us to measure the velocity of each component of the pulse wave, as suggested and measured by Couade et al. (2011):

(1) PWV 1 is the propagation velocity of the foot of the pulse wave, corresponding to the displacement of the main acceleration peak of the arterial diameter increase (**Figure 1B**).
(2) PWV 2 is the propagation velocity of the dicrotic notch, corresponding to the displacement of the main acceleration peak of the arterial diameter recoil (**Figure 1B**).

The precise measurement of each of these PWV components was based on the diameter acceleration signal (derived from the speed at which the wall moves over time). We were thus able to better identify the precise movement of the same signal along the arterial wall. For each acceleration signal, identified as corresponding to PWV 1 or 2 (**Figure 1B**), a linear regression of the space-time coordinates of the acceleration peaks was performed and the PWV was determined by calculating the slope of the regression. Average of right and left carotid values were done for further analyses. The ability of ultrafast ultrasound imaging to accurately evaluate the velocity of an elastic wave propagating at several meters per second within the arterial wall has been validated *in vitro* using the shear wave elastography with the same scanner used in our study (Couade et al., 2010; Maksuti et al., 2016). As well as with the shear wave elastography, PWV measurement is performed using tissue Doppler imaging on the entire length of the probe to track precisely the propagation of the

pulse wave along the arterial segment and has already been used in human studies (Mirault et al., 2015; Marais et al., 2019).

Arterial Stiffness and Stiffening Biomarkers

Ultrafast ultrasound imaging acquisitions give access to the measurement of several complementary arterial stiffness indicators. At the carotid level, the longitudinal view of the carotid artery allowed us to measure the PWV 1, generated at diastolic arterial pressure (DBP) and PWV 2, at the time of the systolic arterial pressure peak (SBP). Since the PWV value is dependent on the level of blood pressure, each PWV value is shown divided by its corresponding blood pressure. Distensibility, maximum rate of systolic distension (MRSD) and maximum rate of diastolic recoil (MRDR), as defined by Aquaro et al. (2011) with MRI, can be measured in the same sequence, by analyzing the change in vessel diameter, obtained by tracking the wall with ultrafast tissue Doppler (**Figure 2B**).

Carotid Flow Velocities and Wall Shear Stress (WSS)

To evaluate the WSS along the arterial wall, the same sequences were processed to produce vector flow images of the arterial flow. An adaptive spatiotemporal singular value decomposition (SVD) clutter filter was then used to separate tissue from blood (Baranger et al., 2018). Tissue Doppler was computed in order to track automatically the wall over the entire sequence and thus avoid WSS discrepancies due to arterial motion during the cardiac cycle. Multi-directional (−10°, 0°, 10°) color-Doppler images were assessed using sub-aperture beamforming, and used to compute flow vectors inside the lumen area. Lastly, considering blood as a Newtonian fluid, the WSS was derived using the following formula:

$$\tau = \mu . ||\vec{\nabla} \times \vec{v}||_{\partial\Omega} = \mu . |- \frac{\partial v_x}{\partial z} + \frac{\partial v_z}{\partial x}|_{\partial\Omega}$$

With τ(Pa): the Wall Shear Stress, μ (Pa.s): the blood viscosity, $\vec{\nabla}$: the gradient operator, $\vec{v}\,(m.s^{-1})$: the blood velocity, Ω describes the region of the lumen and $\partial\Omega$ its boundary.

Statistical Analysis

Continuous data are presented as a mean ± standard deviation. Comparisons were done using a Student *t*-test. To assess the correlation between age and arterial stiffness parameters, we used the linear correlations with Pearson's coefficients and covariance analysis (ANCOVA), according to BAV status. The categorical variables were compared using the Chi-square test. Statistical significance was considered at the 0.05 level. Analyses were performed using R® software (R-Studio, version 3.4.1, Boston, MA, United States).

RESULTS

Population

Ninety-two non-operated patients with BAV and forty-eight controls were consecutively assessed for their carotids in addition to their cardiac evaluation. Patients' characteristics are presented in **Table 1**. BAV patients only differed from controls on gender, aortic diameters and stiffness. Men were more represented in BAV patients than in controls.

Aortic Stiffness in BAV and Controls

Diameters were larger at the sinus of Valsalva and at the tubular level of the ascending aorta in BAV patients compared with controls. It is important to note that the systolic and diastolic blood pressure values, key elements for the interpretation of the arterial stiffness indicators, did not differ between the two groups. Segmental aortic distensibility, measured by conventional echocardiography, was significantly lower in case of BAV ($p < 0.001$ at the sinus of Valsalva level and $p = 0.018$ at the tubular aortic level, **Table 1**).

Carotid Stiffness Between Patients With BAV and Controls

The carotid stiffness parameters, PWV raw values as well as values divided by the corresponding blood pressure, as reported by Mirault et al. (2015) are presented in **Table 2**. In univariate analysis, no significant difference was found between patients with BAV and controls for each carotid stiffness parameter (**Table 2**). Due to the influence of age on the arterial stiffness, correlations between stiffness indicators (*Y*-axis) and age (*X*-axis) are shown in **Figures 3–5**. A poor correlation was found for PWV1 with age (R^2 = 0.087 for BAV and R^2 = 0.004 for controls), but no correlation for PWV 1/DBP with age (R^2 = 0.005 for BAV and R^2 = 0.001 for controls) (**Figure 3**). Greater correlations with age were established for PWV 2 (R^2 = 0.283 for BAV and R^2 = 0.556 for controls), and to a lesser extend for PWV 2/SBP (R^2 = 0.050 for BAV and R^2 = 0.039 for controls). A significant correlation was found between arterial stiffening over the cardiac cycle, measured by Delta-PWV and Delta-PWV/PP, and age (**Figure 4**).

TABLE 1 | Characteristics of BAV patients and controls.

	BAV patients *N* = 92	Controls *N* = 48	*p*
Age (years)	47.5 ± 16.6	42.6 ± 17.6	0.107
Men	62 (67)	18 (38)	<0.001
Sinus of Valsalva diameter (mm)	35.3 ± 6.6	27.8 ± 5.8	<0.001
Tubular ascending aorta diameter (mm)	36.6 ± 8.3	28.4 ± 4.6	<0.001
Mean carotid arterial diameter (mm)	6.84 ± 0.82	6.56 ± 0.82	0.066
Sinus of Valsalva distensibility (10^3.mmHg^{-1})	1.86 ± 1.66	3.65 ± 2.19	<0.001
Tubular aorta distensibility (10^3.mmHg^{-1})	2.70 ± 2.11	3.69 ± 2.21	0.018
DBP (mmHg)	71.5 ± 10.7	69.8 ± 10.1	0.370
SBP (mmHg)	120.2 ± 16.3	117.6 ± 15.0	0.362
PP (mmHg)	48.6 ± 12.5	47.5 ± 10.8	0.616

Results are mean ± standard deviation, or number (percentage). BAV, bicuspid aortic valve; DBP, diastolic aortic pressure; SBP, systolic aortic pressure; PP, pulse pressure. P-values are from Student t-test and Chi-square test for sex comparison.

TABLE 2 | Carotid stiffness parameters of BAV patients and controls.

	BAV patients $N = 92$	Controls $N = 48$	p
PWV-1 ($m.s^{-1}$)	4.40 ± 1.06	4.14 ± 1.07	0.188
PWV-2 ($m.s^{-1}$)	6.42 ± 1.98	6.02 ± 2.05	0.293
Delta–PWV ($m.s^{-1}$)	2.01 ± 1.87	1.88 ± 1.92	0.723
PWV-1/DBP ($cm.s^{-1}.mmHg^{-1}$)	6.82 ± 1.47	6.38 ± 1.18	0.084
PWV-2/SBP ($cm.s^{-1}.mmHg^{-1}$)	5.29 ± 1.63	5.24 ± 1.39	0.660
Delta–PWV/PP ($cm.s^{-1}.mmHg^{-1}$)	2.87 ± 3.08	3.38 ± 2.81	0.353
Distensibility ($mmHg^{-1}$)	26.1 ± 21.0	27.6 ± 15.6	0.503
MRSD (s^{-1})	1.89 ± 1.10	2.15 ± 1.07	0.177
MRDR (s^{-1})	1.00 ± 0.59	1.01 ± 0.52	0.942

Results are mean ± standard deviation. BAV, bicuspid aortic valve; DBP, diastolic aortic pressure; SBP, systolic aortic pressure; PP, pulse pressure; PWV, pulse wave velocity; MRSD, maximal rate of systolic distension; MRDR, maximal rate of diastolic recoil. P-values are from Student t-test.

Carotid diameters did not differ in BAV patients compared with controls. Concerning the indicators based on the carotid diameter variation (distensibility, MRSD, and MRDR), the correlations obtained with age were much better than those obtained by measuring the PWV. MRSD and MRDR values correlated well with age (**Figure 5**). No significant difference was found in any of the parameters evaluated between patients with BAV and controls (**Table 2**).

Carotid Flow Parameters Between Patients With BAV and Controls

No difference in peak systolic velocity was observed between BAV patients and controls. The measurement of the WSS over the cardiac cycle allowed us to determine the maximal peak of WSS as well as the average of WSS over the whole sequence (time average WSS). There was no significant difference between BAV patients and controls for each of these parameters (**Table 3**, **Supplementary Figure S2**, and **Supplementary Table S1**).

DISCUSSION

The multiparametric analysis of carotid stiffness and carotid stiffening over the cardiac cycle did not provide any specific biomechanical change of the common carotid arteries in BAV patients, although they had a segmental aortopathy compared

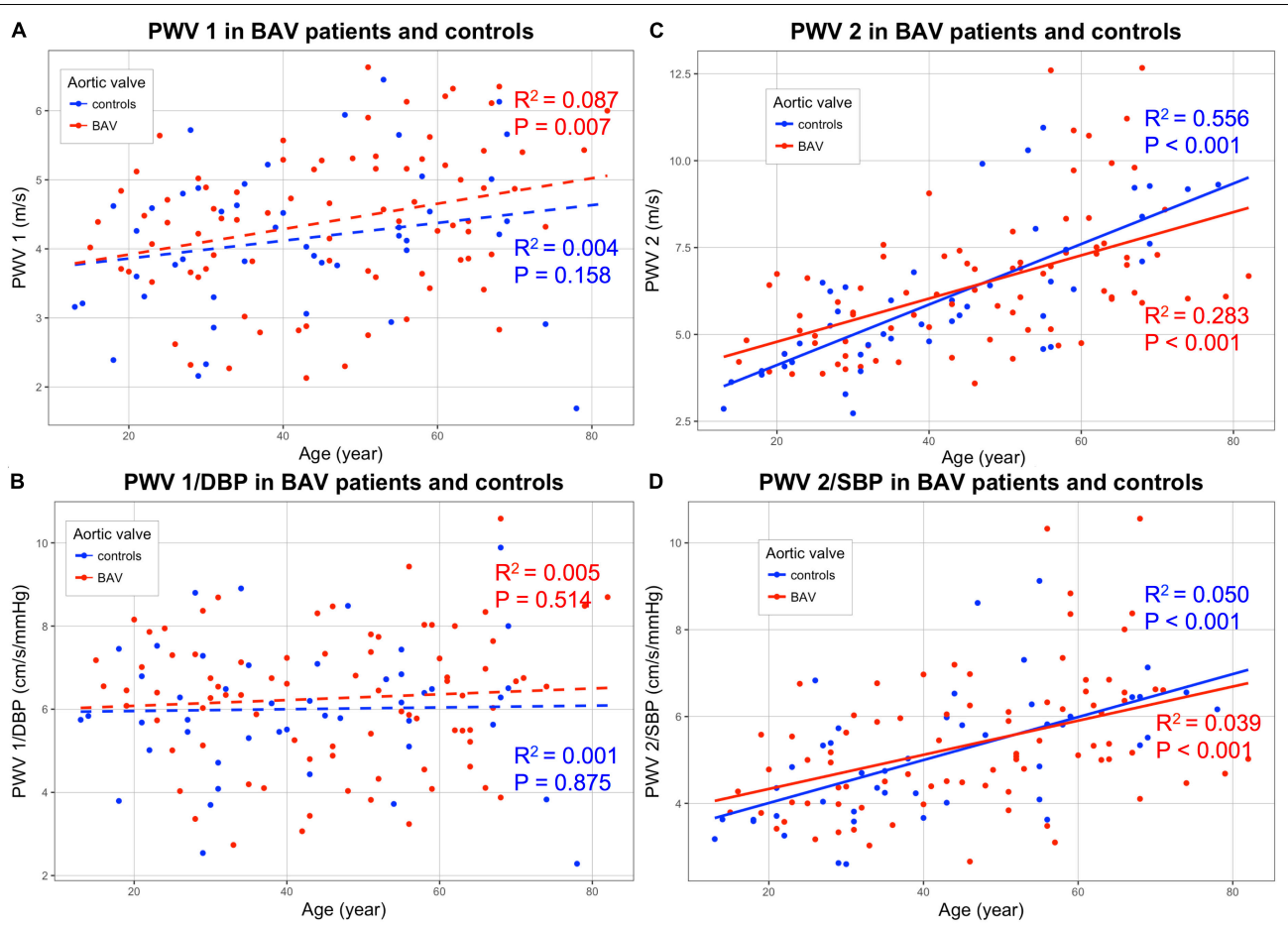

FIGURE 3 | Correlations of following stiffening indicators (*Y*-axis) with age (*X*-axis): PWV 1 **(A)**; (PWV1/DBP) **(B)**; PWV2 **(C)** and PWV2/SBP **(D)**, for patients with bicuspid aortic valve (BAV) (red) and controls (blue). BAV, bicuspid aortic valve; PWV, pulse wave velocity; DBP, diastolic blood pressure; SBP, systolic blood pressure.

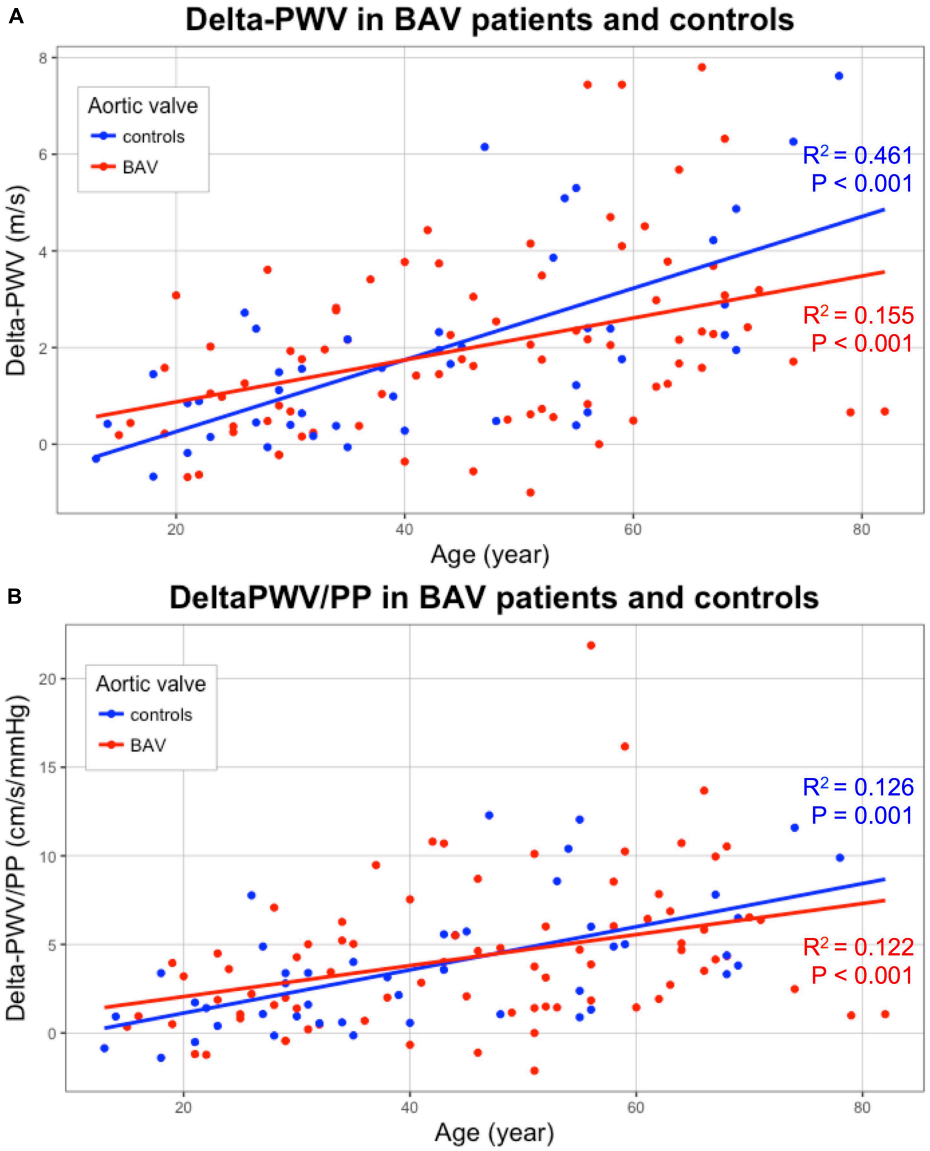

FIGURE 4 | Correlation of carotid stiffening indicators (*Y*-axis) with age (*X*-axis): Delta-PWV **(A)** and Delta-PWV/PP **(B)**, for patients with bicuspid aortic valve (BAV) (red) and controls (blue). BAV, bicuspid aortic valve; PWV, pulse wave velocity; PP, pulse pressure.

with controls. The study of carotid walls in case of BAV has been poorly conducted and the results presented in the literature are contradictory. A lower carotid distensibility was found using conventional ultrasound imaging by Li et al. (2016). The carotid distensibility, evaluated with B mode by the authors, remains however, a variable measurement with a low reproducibility, since it is difficult to follow precisely the carotid walls and determine exactly the minimum and maximum diameters. Kim et al. (2017) did not find any difference in carotid morphology (diameter and thickness intima-media), distensibility and peak tissue velocity using tissue Doppler on the carotid wall. This technology may be more accurate than the classic B-mode to assess distensibility. The tissue Doppler allows indeed a more precise measurement of small displacements of the arterial wall because it is based on a very precise estimate of the displacement velocity. It allows to quantify sub-wavelength displacements (much less than the mm) which is not possible with the speckle tracking (Bonnefous and Pesqué, 1986).

Our results converge toward the absence of the common carotid artery involvement in BAV-associated vascular remodeling, which appears to affect only the ascending aorta, and particularly the sinus of Valsalva (Goudot et al., 2019b). From an embryological point of view, the smooth muscle cells forming the aortic valve and the sinus of Valsalva come from the second cardiac field, while the smooth muscle cells forming the tubular aorta and the common carotid arteries come from the neural crest (Yassine et al., 2017). This divergent

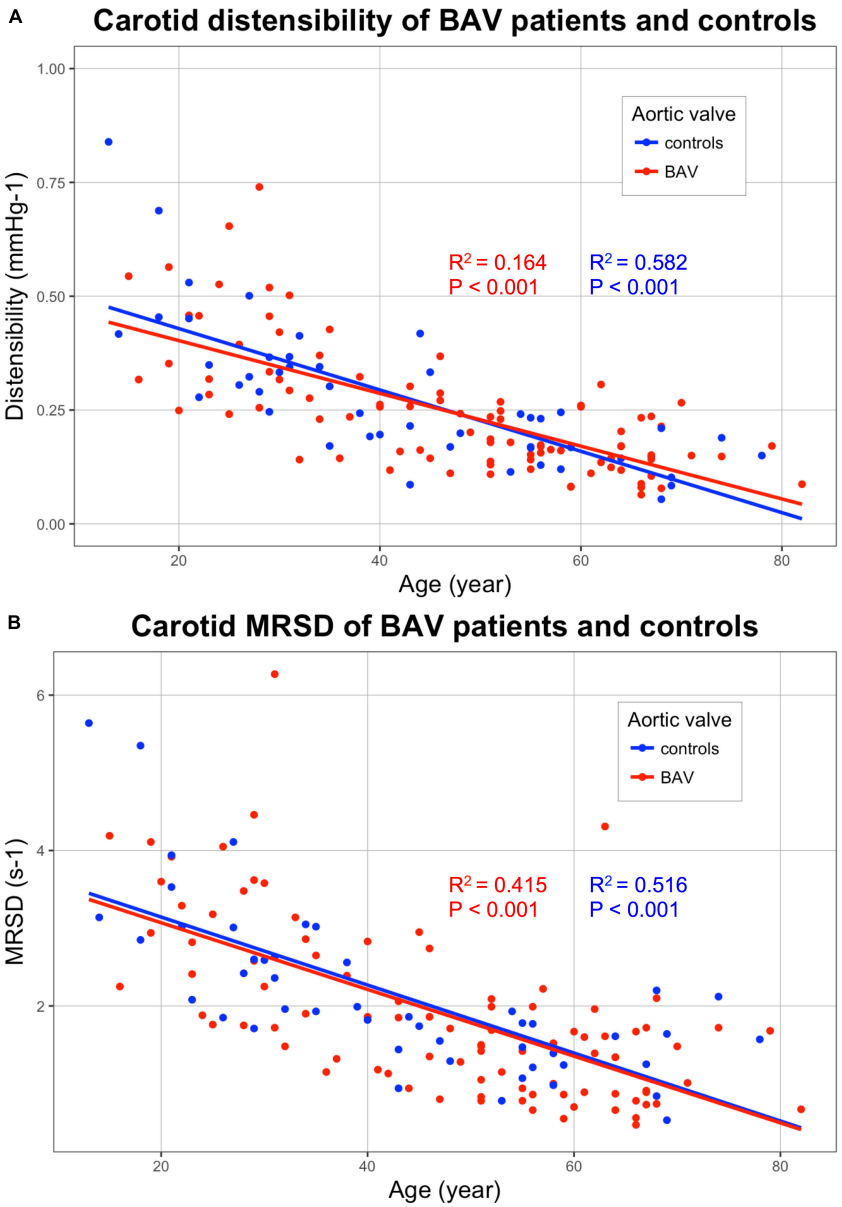

FIGURE 5 | Correlations of the following stiffness indicators (*Y*-axis) with age (*X*-axis): Distensibility **(A)** and MRSD **(B)**, for patients with bicuspid aortic valve (BAV) (red) and controls (blue). BAV, bicuspid aortic valve; MRSD, maximal rate of systolic distension.

TABLE 3 | Flow parameters of BAV patients and controls.

	BAV patients *N* = 92	**Controls *N* = 48**	**p**
Maximal WSS (Pa)	1.80 ± 0.46	1.86 ± 0.44	0.497
Time average WSS (Pa)	0.95 ± 0.23	0.95 ± 0.20	0.870
PSV ($cm.s^{-1}$)	116 ± 36	124 ± 39	0.266

Results are mean ± standard deviation. BAV, bicuspid aortic valve; WSS, wall shear stress; PSV, peak systolic velocity. P-values are from Student t-test.

embryological lineage could explain the results obtained on all the vascular walls studied: on the one hand, a more important stiffness of the sinus of Valsalva appearing at a younger age, with a stiffness acquired later, dependent on dilatation of the tubular aorta, and, on the other hand, no damage to the common carotid arteries nor to the abdominal aorta (Goudot et al., 2019b). New technical settings are mandatory to be able to assess the ascending aorta by transthoracic ultrafast ultrasound imaging. The evaluation of similar morphological biomarkers with ultrasound would provide a simple and easily accessible tool, which could be rapidly integrated into the follow-up of patients with BAV, usually performed only by echocardiography. The aortic stiffness could thus be an additional measure to the usual measures of the aortic diameters at the different segments of the ascending aorta (Erbel et al., 2014).

Lastly, we provide a technological innovation regarding the combined evaluation of WSS and carotid stiffness. Hemodynamic assessment of blood flow is an important factor in the arterial wall remodeling (Yassine et al., 2017). The lack of WSS change in case of BAV could thus explain the absence of stiffness modification of the carotid wall. WSS modifications in the ascending aorta related to the specific morphology of the BAV appear to be indeed responsible for a significant proportion of degenerative lesions observed in the aortic wall (Guzzardi et al., 2015). Developing ultrasound imaging combining stiffness and WSS measurements would therefore be particularly relevant to assess aortopathy associated with BAV.

Limitations

All the stiffness data were only processed after examining the patient. The distensibility is indeed not currently available on the commercialized UF ultrasound scanner. The automated method for collecting stiffness parameters in real time could be however, quickly implemented. The study of first-degree relatives as control patients is also a limitation. BAV first-degree relatives cannot indeed be considered completely free from minor aortic involvement. In our series, even though we have shown no difference in carotid stiffness, there were, however, significant differences in diameter and aortic distensibility between BAV patients and controls.

CONCLUSION

Ultrafast ultrasound imaging allows an automated simultaneous evaluation of carotid stiffness and flow parameters over the cardiac cycle. No difference was found for stiffness and stiffening parameters between BAV patients and controls at the common carotid level. An aortic evaluation, using a dedicated phased array probe, would provide the parameters of aortic distensibility, MRSD, and PWV. This study is progressing, with a specific sequence for a phased array probe currently being developed.

DATA AVAILABILITY STATEMENT

The datasets generated for this study are available on request to the corresponding author.

ETHICS STATEMENT

The studies involving human participants were reviewed and approved by CPP Île-de-France VI (2017-A01508-45). Written informed consent to participate in this study was provided by the participants' legal guardian/next of kin.

AUTHOR CONTRIBUTIONS

GG, CC, and LK carried out the dedicated consultations and collected the data. OP, JP, MG, and MP analyzed the data. GG and TM performed the statistical analysis and wrote the manuscript. MP, XJ, and EM proofread the manuscript. EM organized this study, supervised the cardiac ultrasounds, performed final approval of the version to be published, and agreed to be accountable for all aspects of the work in ensuring that questions related to the accuracy and integrity of any part of the work are appropriately investigated and resolved.

ACKNOWLEDGMENTS

We thank the SFC (French Society of Cardiology) and INSERM for the funding support.

SUPPLEMENTARY MATERIAL

The Supplementary Material for this article can be found online at: https://www.frontiersin.org/articles/10.3389/fphys.2019.01330/full#supplementary-material

FIGURE S1 | Longitudinal section of a common carotid artery with ultrafast ultrasound B-mode imaging. The segmentations of the anterior (blue line) and posterior (red line) walls are indicated in the picture.

FIGURE S2 | Correlations of the wall shear stress (WSS) parameters (*Y*-axis) with age (*X*-axis): Maximal WSS **(A)** and time-average WSS **(B)**, for BAV patients (red) and controls (blue). BAV: bicuspid aortic valve. Pearson's coefficients square (R^2) and *P*-values for each correlation line are presented.

TABLE S1 | Linear correlations of maximal wall shear stress (WSS) and time average WSS, with age.

VIDEO S1 | Ultrafast ultrasound imaging of a common carotid artery. Representation of the tissue Doppler data (color scale). The propagation of the pulse wave components (PWV1 and PWV2) is notified on the ECG recording.

REFERENCES

Aboyans, V., Ricco, J.-B., Bartelink, M.-L. E. L., Björck, M., Brodmann, M., Cohnert, T., et al. (2017). 2017 ESC guidelines on the diagnosis and treatment of peripheral arterial diseases, in collaboration with the european society for vascular surgery (ESVS). *Eur. Heart J.* 39, 763–816. doi: 10.1093/eurheartj/ehx095

Aquaro, G. D., Ait-ali, L., and Basso, M. L. (2011). Elastic properties of aortic wall in patients with bicuspid aortic. *AJC* 108, 81–87. doi: 10.1016/j.amjcard.2011.03.005

Aquaro, G. D., Briatico Vangosa, A., Toia, P., Barison, A., Ait-Ali, L., Midiri, M., et al. (2017). Aortic elasticity indices by magnetic resonance predict progression of ascending aorta dilation. *Eur. Radiol.* 27, 1395–1403. doi: 10.1007/s00330-016-4501-5

Baranger, J., Tanter, M., Baud, O., Perren, F., Demene, C., and Arnal, B. (2018). Adaptive spatiotemporal SVD clutter filtering for ultrafast doppler imaging using similarity of spatial singular vectors. *IEEE Trans. Med. Imaging* 37, 1574–1586. doi: 10.1109/tmi.2018.2789499

Bercoff, J., Montaldo, G., Loupas, T., Savery, D., Mézière, F., Fink, M., et al. (2011). Ultrafast compound doppler imaging: providing full blood flow characterization. *IEEE Trans. Ultrason. Ferroelectr. Freq. Control* 58, 134–147. doi: 10.1109/TUFFC.2011.1780

Bonnefous, O., and Pesqué, P. (1986). Time domain formulation of pulse-doppler ultrasound and blood velocity estimation by cross

correlation. *Ultrason. Imaging* 8, 73–85. doi: 10.1177/016173468600800201

Couade, M., Pernot, M., Messas, E., Emmerich, J., Hagege, A., Fink, M., et al. (2011). Ultrafast imaging of the arterial pulse wave. *IRBM* 32, 106–108. doi: 10.1016/j.irbm.2011.01.012

Couade, M., Pernot, M., Prada, C., Messas, E., Emmerich, J., Bruneval, P., et al. (2010). Quantitative assessment of arterial wall biomechanical properties using shear wave imaging. *Ultrasound Med. Biol.* 36, 1662–1676. doi: 10.1016/j.ultrasmedbio.2010.07.004

Erbel, R., Aboyans, V., Boileau, C., Bossone, E., Di Bartolomeo, R., Eggebrecht, H., et al. (2014). 2014 ESC guidelines on the diagnosis and treatment of aortic diseases. *Eur. Heart J.* 35, 2873–2926. doi: 10.1093/eurheartj/ehu281

Goudot, G., Mirault, T., Bruneval, P., Soulat, G., Pernot, M., and Messas, E. (2019a). Aortic wall elastic properties in case of bicuspid aortic valve. *Front. Physiol.* 10:299. doi: 10.3389/fphys.2019.00299

Goudot, G., Mirault, T., Rossi, A., Zarka, S., Albuisson, J., Achouh, P., et al. (2019b). Segmental aortic stiffness in patients with bicuspid aortic valve compared with first-degree relatives. *Heart* 105, 130–136. doi: 10.1136/heartjnl-2018-313232

Goudot, G., Papadacci, C., Dizier, B., Baudrie, V., and Ferreira, I. (2018). Arterial stiffening with ultrafast ultrasound imaging gives new insight into arterial phenotype of vascular ehlers-danlos mouse models. *Ultraschall Med.* doi: 10.1055/a-0599-0841 [Epub ahead of print].

Guzzardi, D. G., Barker, A. J., Van Ooij, P., Malaisrie, S. C., Puthumana, J. J., Belke, D. D., et al. (2015). Valve-related hemodynamics mediate human bicuspid aortopathy: insights from wall shear stress mapping. *J. Am. Coll. Cardiol.* 66, 892–900. doi: 10.1016/j.jacc.2015.06.1310

Kim, M., Shim, C. Y., You, S., Cho, I., Hong, G., Ha, J. W., et al. (2017). Characteristics of carotid artery structure and mechanical function and their relationships with aortopathy in patients with bicuspid aortic valves. *Front. Physiol.* 8:622. doi: 10.3389/fphys.2017.00622

Le Lièvre, C. S., and Le Douarin, N. M. (1975). Mesenchymal derivatives of the neural crest: analysis of chimaeric quail and chick embryos. *J. Embryol. Exp. Morphol.* 34, 125–154.

Li, Y., Deng, Y.-B., Bi, X.-J., Liu, Y.-N., Zhang, J., and Li, L. (2016). Evaluation of myocardial strain and artery elasticity using speckle tracking echocardiography and high-resolution ultrasound in patients with bicuspid aortic valve. *Int. J. Cardiovasc. Imaging* 32, 1063–1069. doi: 10.1007/s10554-016-0876-2

Majesky, M. W. (2007). Developmental basis of vascular smooth muscle diversity. *Arterioscler. Thromb. Vasc. Biol.* 27, 1248–1258. doi: 10.1161/ATVBAHA.107.141069

Maksuti, E., Widman, E., Larsson, D., Urban, M. W., Larsson, M., and Bjällmark, A. (2016). Arterial stiffness estimation by shear wave elastography: validation in phantoms with mechanical testing. *Ultrasound Med. Biol.* 42, 308–321. doi: 10.1016/j.ultrasmedbio.2015.08.012

Marais, L., Pernot, M., Khettab, H., Tanter, M., Messas, E., Zidi, M., et al. (2019). Arterial stiffness assessment by shear wave elastography and ultrafast pulse wave imaging: comparison with reference techniques in normotensives and hypertensives. *Ultrasound Med. Biol.* 45, 758–772. doi: 10.1016/j.ultrasmedbio.2018.10.032

Mirault, T., Pernot, M., Frank, M., Couade, M., Niarra, R., Azizi, M., et al. (2015). Carotid stiffness change over the cardiac cycle by ultrafast ultrasound imaging in healthy volunteers and vascular Ehlers-Danlos syndrome. *J. Hypertens.* 33, 1890–1896. doi: 10.1097/HJH.0000000000000617

Montaldo, G., Tanter, M., Bercoff, J., Benech, N., and Fink, M. (2009). Coherent plane-wave compounding for very high frame rate ultrasonography and transient elastography. *IEEE Trans. Ultrason. Ferroelectr. Freq. Control* 56, 489–506. doi: 10.1109/TUFFC.2009.1067

Nistri, S., Grande-Allen, J., Noale, M., Basso, C., Siviero, P., Maggi, S., et al. (2008). Aortic elasticity and size in bicuspid aortic valve syndrome. *Eur. Heart J.* 29, 472–479. doi: 10.1093/eurheartj/ehm528

Santarpia, G., Scognamiglio, G., Di Salvo, G., D'Alto, M., Sarubbi, B., Romeo, E., et al. (2012). Aortic and left ventricular remodeling in patients with bicuspid aortic valve without significant valvular dysfunction: a prospective study. *Int. J. Cardiol.* 158, 347–352. doi: 10.1016/j.ijcard.2011.01.046

Schievink, W. I., and Mokri, B. (1995). Familial aorto-cervicocephalic arterial dissections and congenitally bicuspid aortic valve. *Stroke* 26, 1935–1940. doi: 10.1161/01.STR.26.10.1935

Tanter, M., and Fink, M. (2014). Ultrafast imaging in biomedical ultrasound. *IEEE Trans. Ultrason. Ferroelectr. Freq. Control* 61, 102–119. doi: 10.1109/TUFFC.2014.6689779

Verma, S., and Siu, S. C. (2014). Aortic dilatation in patients with bicuspid aortic valve. *N. Engl. J. Med.* 370, 1920–1929. doi: 10.1056/NEJMra1207059

Yassine, N. M., Shahram, J. T., and Body, S. C. (2017). Pathogenic mechanisms of bicuspid aortic valve aortopathy. *Front. Physiol.* 8:687. doi: 10.3389/fphys.2017.00687

Conflict of Interest: The authors declare that the research was conducted in the absence of any commercial or financial relationships that could be construed as a potential conflict of interest.

frontiers in Physiology

ORIGINAL RESEARCH
published: 14 January 2020
doi: 10.3389/fphys.2019.01563

Quantitative Comparison of the Performance of Piezoresistive, Piezoelectric, Acceleration, and Optical Pulse Wave Sensors

Hongju Wang[1], Lu Wang[2], Nannan Sun[1], Yang Yao[1], Liling Hao[1], Lisheng Xu[1,3] and Stephen E. Greenwald[4]*

[1] College of Medicine and Biomedical Information Engineering, Northeastern University, Shenyang, China, [2] School of Computer Science and Engineering, Northeastern University, Shenyang, China, [3] Neusoft Research of Intelligent Healthcare Technology, Co. Ltd., Shenyang, China, [4] Blizard Institute, Barts and The London School of Medicine and Dentistry, Queen Mary University of London, London, United Kingdom

OPEN ACCESS

Edited by:
Kelvin Kian Loong Wong, The University of Adelaide, Australia

Reviewed by:
Nizam Uddin Ahamed, University of Pittsburgh, United States
Guanghao Sun, University of Electro-Communications, Japan
Mariana Amorim Fraga, Federal University of São Paulo, Brazil
Zine Ghemari, University of M'sila, Algeria

***Correspondence:**
Lisheng Xu
xuls@bmie.neu.edu.cn

Specialty section:
This article was submitted to Computational Physiology and Medicine, a section of the journal Frontiers in Physiology

Received: *10 June 2019*
Accepted: *12 December 2019*
Published: *14 January 2020*

Citation:
Wang H, Wang L, Sun N, Yao Y, Hao L, Xu L and Greenwald SE (2020) Quantitative Comparison of the Performance of Piezoresistive, Piezoelectric, Acceleration, and Optical Pulse Wave Sensors. Front. Physiol. 10:1563. doi: 10.3389/fphys.2019.01563

The accurate measurement of the arterial pulse wave is beneficial to clinical health assessment and is important for the effective diagnosis of many types of cardiovascular disease. A variety of sensors have been developed for the non-invasive detection of these waves, but the type of sensor has an impact on the measurement results. Therefore, it is necessary to compare and analyze the signals obtained under a range of conditions using various pulse sensors to aid in making an informed choice of the appropriate type. From the available types we have selected four: a piezoresistive strain gauge sensor (PESG) and a piezoelectric Millar tonometer (the former with the ability to measure contact force), a circular film acceleration sensor, and an optical reflection sensor. Pulse wave signals were recorded from the left radial, carotid, femoral, and digital arteries of 60 subjects using these four sensors. Their performance was evaluated by analyzing their susceptibilities to external factors (contact force, measuring site, and ambient light intensity) and by comparing their stability and reproducibility. Under medium contact force, the peak-to-peak amplitude of the signals was higher than that at high and low force levels and the variability of signal waveform was small. The optical sensor was susceptible to ambient light. Analysis of the intra-class correlation coefficients (ICCs) of the pulse wave parameters showed that the tonometer and accelerometer had good stability (ICC $>$ 0.80), and the PESG and optical sensor had moderate stability (0.46 $<$ ICC $<$ 0.86). Intra-observer analysis showed that the tonometer and accelerometer had good reproducibility (ICC $>$ 0.75) and the PESG and optical sensor had moderate reproducibility (0.42 $<$ ICC $<$ 0.91). Inter-observer analysis demonstrated that the accelerometer had good reproducibility (ICC $>$ 0.85) and the three other sensors had moderate reproducibility (0.52 $<$ ICC $<$ 0.96). We conclude that the type of sensor and measurement site affect pulse wave characteristics and the careful selection of appropriate sensor and measurement site are required according to the research and clinical need. Moreover, the influence of external factors such as contact pressure and ambient light should be fully taken into account.

Keywords: pulse wave, sensor, performance, reproducibility, stability, quantitative analysis

INTRODUCTION

The arterial pulse wave contains much physiological and pathological information and its accurate measurement can improve the diagnosis of cardiovascular disease (Ma et al., 2013; Papaioannou et al., 2016), now a major public health problem worldwide (Yang et al., 2016). Many types of sensors have been developed for the non-invasive detection of pulse waves (Schafer and Vagedes, 2013; Meidert et al., 2014; Stea et al., 2014; Boutry et al., 2015; Kamshilin et al., 2016). One of the earliest devices used for this purpose was the applanation tonometer, first used clinically in 1902 (Mackenzie, 1902; O'Rourke, 2016). Commercial products appeared in 1970, of which the CBM series produced by the Colin Company in Japan were among the most widely used (Kemmotsu et al., 1994). Subsequently, many other types of sensors have been developed and used in a clinical setting. These include piezoresistive and piezoelectric devices as well as photoelectric sensors. Chen et al. (2016) presented an ultra-flexible strain sensor for the long-term measurement of pulse waves. Murphy et al. (2011) proposed a piezoelectric sensor based on polyvinyl difluoride (PVDF) for the measurement of pulse wave velocity (PWV) in hypertensive patients. Clemente et al. (2010) designed a piezo-film-based measurement method to reconstruct the blood pressure waveform. Lovinsky (2006) presented an optical pulse sensor system to monitor arterial oxygen saturation and Loukogeorgakis et al. (2002) proposed a new method for measuring PWV using reflectance photoplethysmography. Li et al. (2018) used photoplethysmography to investigate the changes of arterial waveform characteristics in pregnant women.

In the last few years, some studies have combined different sensor types for pulse acquisition. For example, Huotaril et al. (2013) used electro-mechanical film (EMFi) and photoplethysmographic (PPG) sensors to measure pulse waves from the left forefinger, wrist, and second toe arteries, and compared the pulse wave decomposition parameters between EMFi and PPG to obtain information about arterial elasticity. Wang et al. (2015) combined a pressure sensor with a photoelectric sensor array to make a multichannel device and demonstrated that this device was more effective than previous pulse acquisition platforms. These and other studies demonstrate the increasing use of pulse wave analysis derived from different types of sensors to obtain prognostic and diagnostic information from patients with cardiovascular disease, especially hypertension (Townsend et al., 2015) and are a sign of the increasing need to provide screening of at-risk patients in a primary care setting, thus relieving pressure on specialist centers. By analyzing pulse wave characteristics, these devices can be used to obtain useful diagnostic information such as PWV, peripheral resistance, vascular compliance, and blood flow changes. The above parameters can be used to determine the degree of vascular stiffness, reflect cardiovascular status, and predict the onset or track the progression of cardiovascular disease.

Although all these devices can detect and record the arterial pulse wave, their mode of operation and sensitivity differ, leading to differences in the shape and timing of the pulse wave and thus to variations in their diagnostic effectiveness (Zuo et al., 2016). Therefore, to exploit the advantages of each type of sensor and to optimize their effectiveness, it is necessary to analyze their stability and repeatability, the influence of external factors on their performance as well as their overall design. At present, there is a lack of literature directly comparing the performance of different sensor types.

In this study, we chose the three kinds of sensors that are most widely used in clinical practice, pressure sensor, PPG sensor, and acceleration sensor. In order to verify the influence of contact force the acquired signal, we also added a sensor developed by our laboratory that can measure contact pressure. Firstly, a circular film acceleration sensor which measures the acceleration perpendicular to the skin by detecting the dilation of underlying arteries to record the pulse wave (Elgendi, 2014; Muehlsteff et al., 2015); secondly, a PPG sensor in which a photodiode produces light, some of which is absorbed by blood in superficial vessels below the skin. By detecting the time varying reflection due to blood volume changes during the cardiac cycle, a representation of the pulse wave is obtained (Hertzman, 1937); thirdly, a piezoresistive strain gauge sensor (PESG) designed in our laboratory, which converts pressure signals from the arteries into a change in the strain-dependent resistance, in a bridge circuit to produce a varying voltage which corresponds to the pulse wave signal (Wang et al., 2013; Xu et al., 2014; He et al., 2017); finally, a piezoelectric Millar tonometer which operates in a similar manner. An effective sensor must be robust, stable, and give reproducible signals. Many factors can affect their performance, including the way in which they are applied to the skin, the contact force between the sensor and the skin (Teng and Zhang, 2006), and the measuring site (Lukas et al., 2014; Hartmann et al., 2019). Therefore, we have analyzed the four sensors' susceptibilities to these external factors and compared their stability and reproducibility.

MATERIALS AND METHODS

Subjects

The study included 60 healthy college students (30 females and 30 males) with mean age 24 ± 2 years, mean height 167.5 ± 5.7 cm, mean weight 59.3 ± 9.2 kg, mean heart rate 69 ± 8 bmp, mean systolic blood pressure 119 ± 9 mmHg, and mean diastolic blood pressure 78 ± 8 mmHg. All participants were fully informed about the study and gave their informed consent. The study was designed in accordance with the Helsinki Declaration and was approved by the local ethics committee. All measurements were taken after 24 h without alcohol or caffeine with an otherwise normal diet. Smokers, and those on any medication were excluded from the study and none of the subjects had exercised vigorously within 1 h before the measurement.

Protocol

All measurements were performed in a quiet environment after a rest period of 15 min, during which personal information (age, height, weight) was obtained and the study protocol was explained. For the radial artery measurements, subjects were seated with the left arm bent at the elbow to an angle of 90 ± 5°

and the forearm resting on a table. Subjects were asked to keep their palms relaxed. Signals were recorded for 30 s from a point above the radial artery near the wrist where the strongest pulse was found (in the order: PESG, tonometer, accelerometer, and optical probe, explained in more detail below), and the study protocol was repeated for each subject three times.

The accelerometer is an inertial device, which records the pulse wave by detecting displacement of the skin over the artery under investigation (Elgendi, 2014). In this study, the accelerometer sensor was interfaced to a multichannel physiological recorder BL-420S (Taimeng Software, Chengdu, China), sampling at a frequency of 1 kHz. The tonometer is a pressure sensor using the principle of applanation tonometry (SphygmoCor, AtCor Medical, Sydney, NSW, Australia) (Crilly et al., 2007a), sampling frequency 128 Hz. The PESG, sampling at 1 kHz was designed and constructed in our laboratory, and held against the skin by a strap. The contact pressure is measured by a resistive element and can be adjusted by tightening or loosening the strap by means of a screw. The optical sensor contains an infrared-emitting diode and a phototransistor to detect the light and acts as a photoplethysmograph (Jingfan Technology, Tianjin, China) (von Wowern et al., 2015). The sampling frequency was 70 Hz.

The tonometer was used as a hand-held device whereas the other sensors were held in contact with the skin by means of a strap. Due to the limitations of the sensor measurement principles, not all sites could be measured by all sensors. For example, the PESG can only measure the pulse wave of the carotid and the radial arteries owing to the length of the strap and sensor size limitations, the finger area was too small for the sensor, and the femoral artery, even when traversing the inguinal ligament, was too deep to give good quality signals. The sites measured by each sensor are listed in **Table 1**.

The experimental design was as follows. First, as shown in **Table 2**, at the wrist, three levels of contact force (light, medium, and heavy) were applied during acquisition of the subject's pulse wave from the left radial artery. The contact force was measured by the PESG, optical probe, and accelerometer. In this study, light contact was defined as a force between 0.6 and 1 N, medium in the range (1.6–2 N), and heavy, in the range (2.8–3.2 N). Due to the shape of the tonometer it was not feasible to measure contact force. Therefore, when using the tonometer, we were only able to subjectively judge the contact force. Then, to allow comparison of the four sensors, each was used in turn to obtain pulse waves (the type of sensor, acquisition position, pressure size, and measurement times are shown in **Table 3**). Finally, the pulse wave was acquired from the left radial artery by the optical sensor at two different ambient light levels, i.e., full room lighting (LED lighting), external daylight only.

TABLE 1 | Measurement sites and the corresponding pulse sensors.

	Site			
Sensor	**Radial**	**Carotid**	**Femoral**	**Digital**
PESG	√	√	–	–
Tonometer	√	√	√	–
Optical probe	√	√	–	√
Accelerometer	√	√	√	√

TABLE 2 | The sequence of pulse wave acquisition at the three levels of contact force (where, L, M, and H represent light, medium, and heavy force, respectively).

Sensor	**PESG**			**Tonometer**			**Optical probe**			**Accelerometer**		
Site	Radial			Radial			Radial			Radial		
Force	L	M	H	L	M	H	L	M	H	L	M	H
Number of measurements	1			1			1			1		

TABLE 3 | The sequence of pulse wave acquisitions (* marks the measurement position for the reproducibility and stability analysis).

Sensor	**PESG**	**Tonometer**	**Optical probe**	**Accelerometer**
Site	Radial*, carotid	Radial*, carotid, femoral	Radial*, carotid, digital	Radial*, carotid, digital, femoral
Force	Medium	Medium	Medium	Medium
Number of measurements	3	3	3	3

Reproducibility refers to the variability between results measured under the same conditions from a given subject during repeated measurements. Two observers measured pulse waves sequentially using the same probe types for the analysis of inter-observer reproducibility. To assess intra-observer reproducibility, the pulse wave was measured three times, in the radial artery only, by the same observer, with no interval between the measurements (Chen et al., 1997; Crilly et al., 2007b). Stability is the ability of a sensor to maintain its performance parameters for a period of time. For the stability assessment, the pulse wave was measured three times, again only in the radial artery, by the same observer in 1 h. For each subject the pulse wave for each sensor on the radial artery was measured by the same observer for 30 s, and the sequences of pulse waves were ensemble averaged to one cycle. Then, the time and amplitude of the pulse wave were normalized to the range 0–1. The dynamic time warping (DTW) algorithm, which is sensitive to the amplitude of the pulse signal, was used to analyze the similarity of the two normalized waveforms (Jeong and Jayaraman, 2015).

Figure 1 shows the pulse wave parameters included in this study. They are defined as follows: (h_1-normalized amplitude of the systolic maximum, h_2-normalized incisura minimum); (h_3-maximum following the dicrotic notch); t_{up}-time interval from foot to systolic maximum; t_i-time interval from foot to incisura; and T-cardiac cycle. Five additional parameters were derived from the measurements: h_2/h_1, h_3/h_1, t_{up}/T; K-value; SER-spectral energy ratio.

The K-value is a characteristic quantity based on the amplitude of the pulse wave, and is defined as (Luo et al., 2006):

$$K = \frac{P_m - P_d}{P_s - P_d} \quad (1)$$

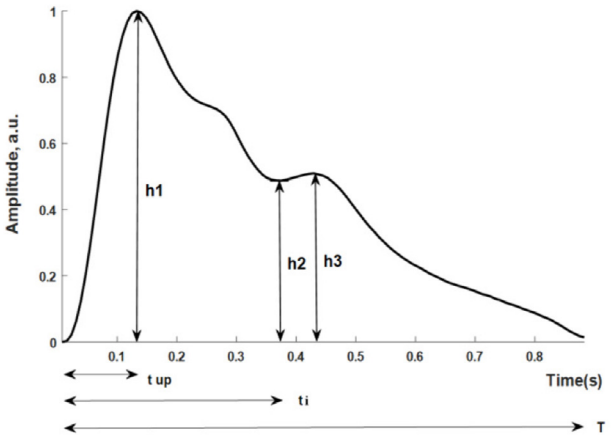

FIGURE 1 | Parameters directly determined from the measured pulse wave.

where P_m is mean arterial pressure of $P(t)$, defined over a cardiac cycle (T) as:

$$P_m = \frac{1}{T}\sum P(t)\Delta(t) \quad (2)$$

and $P(t)$ is the arterial pressure at point t in the cardiac cycle; P_d is diastolic blood pressure; and P_s is the systolic blood pressure.

Spectral energy ratio has been used to describe differences between pulse wave shapes (Thakker and Vyas, 2010). The instantaneous frequency spectrum is defined as:

$$S_k(k) = F[W(n)\cdot x(n)] \quad (3)$$

$$W(n) = \frac{1}{2}\cdot\{1-\cos[2\pi n/(N-1)]\} \quad (4)$$

where $F[]$ represents the Discrete Fourier transform, $W(n)$ is a Hanning window function, and $x(n)$ is the pulse wave signal.

The power spectrum is defined as:

$$S_{xx}(k) = \overline{S_x'(k)\cdot S_x(k)} = \overline{|S_x|^2} \quad (5)$$

where $S_x'(k)$ is the complex conjugate of S_k (k).

The spectral energy within the range of 0 to i Hz is defined as:

$$E(i) = \int_0^i S_{xx}(f)\mathrm{d}f. \quad (6)$$

In this analysis, we introduce the SER:

$$\mathrm{SER} = \frac{E_1}{E_2} = \frac{\int_0^5 S_{xx}(f)\mathrm{d}f}{\int_0^{20} S_{xx}(f)\mathrm{d}f} \quad (7)$$

where E_1 is the energy within the frequency range 0 and 5 Hz; E_2 is the total energy between 0 and 20 Hz.

Statistical Analysis

Data analysis was performed in MATLAB (MathWorks, Natick, MA, United States), first, the pulse wave signals measured by the four sensors were pre-processed to remove baseline drift and reduce noise. The baseline drift was removed by applying "db7" wavelet decomposition (Xu et al., 2005), and de-noised by decomposing the pulse signal at level 4 and eliminating all the details (Mallat, 1989). Then, feature points (onsets, peak points, and dicrotic notch points of the pulse wave) were extracted by windowing methods to further analyze the pulse wave parameters (Yao et al., 2017).

All statistical analysis was performed using SPSS (version 19.0). All subsequently tested variables were assessed for the normality of their distribution using the Shapiro–Wilkes test. Values were expressed as mean ± standard deviation. Pearson's correlation analysis and determination of coefficient of variation were performed to assess the effect of external factors on the pulse wave. Analysis of variance (ANOVA) was performed to examine whether different sensors would affect the calculation of dynamic time warp distance. The intra-class correlation coefficient (ICC) has been used as a standard for measuring the reproducibility of continuous data in several clinical studies (Papaioannou et al., 2007). ICC was calculated for the assessment of intra-observer reproducibility and stability (Bland and Altman, 1986). Values of $p < 0.05$ were considered to indicate statistical significance. It is generally considered that an ICC value > 0.75 implies good reproducibility; $0.4 <$ ICC ≤ 0.75, medium reproducibility; and ICC ≤ 0.4, poor reproducibility (Perloff et al., 1993).

RESULTS

Factors Influencing Sensor Performance

The Effect of Contact Force on the Pulse Wave

As shown in **Figure 2**, for each sensor type, when the contact force was increased from light to medium, the peak-to-peak amplitude of the signal increased. However, a further increase in the application pressure reduced the amplitude. In general, medium contact force was found to produce the highest signal amplitude and, compared with those obtained under lighter and heavier contact forces, the waveform difference of the four sensors under medium pressure is small. Given the dependence of signal amplitude on contact force, it is important to carefully control this to optimize the signal to noise ratio. **Figure 3** shows the effect of changing the probe contact pressure on the normalized waveforms from each sensor type. As shown in **Figure 3**, the optical probe signals are the most strongly affected by probe contact pressure.

The Effect of Measurement Site on the Pulse Wave

As shown in **Table 4**, the coefficients of variation of the parameters (t_{up}/T, h_2/h_1, and K-values) for the radial pulse wave were less than those of the carotid pulse wave, which revealed that the quality of the measurements from the radial artery was better, at least in terms of more consistent beat-to-beat stability. In general, the coefficients of variation for carotid artery measurements with all probes were higher than those of the radial artery. With the probes from which measurements were obtained, the coefficients of variation for the digital and femoral arteries were less than the corresponding carotid and radial values. The accelerometer was able to obtain pulse wave signals from all four measurement sites, and the tonometer worked satisfactorily at the

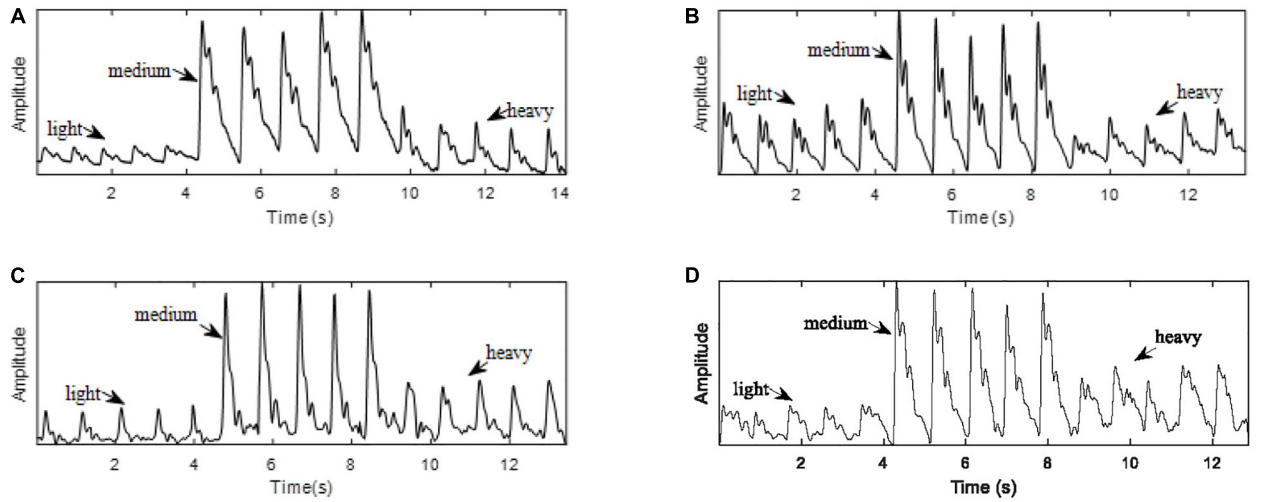

FIGURE 2 | Pulse waves acquired with light, medium, and heavy contact forces. **(A)** PESG. **(B)** tonometer, **(C)** optical sensor, and **(D)** accelerometer.

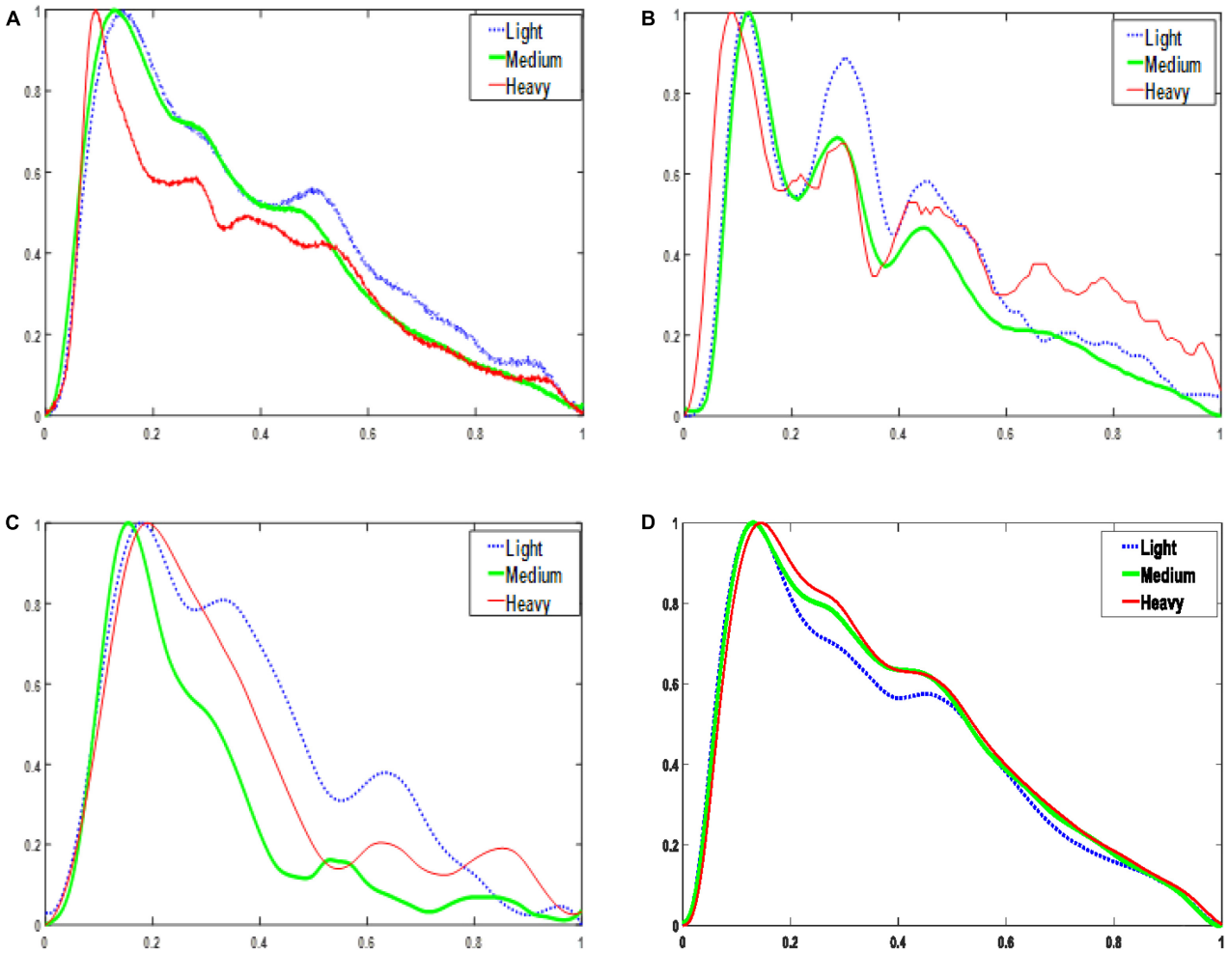

FIGURE 3 | Normalized one-period pulse waves acquired at three magnitudes of contact force. **(A)** PESG. **(B)** tonometer, **(C)** optical sensor, and **(D)** accelerometer.

TABLE 4 | Coefficients of variation for the derived pulse wave parameters, acquired by the four kinds of pulse sensors from the four measuring sites (missing values relate to probe/site combinations for which measurements were impracticable).

		Sensor			
Site	**Parameter**	**PESG**	**Tonometer**	**Optical probe**	**Accelerometer**
Radial	t_{up}/T	0.039	0.014	0.028	0.016
	h_2/h_1	0.048	0.044	0.047	0.059
	K	0.044	0.027	0.055	0.039
Carotid	t_{up}/T	0.058	0.019	0.036	0.022
	h_2/h_1	0.067	0.045	0.078	0.105
	K	0.101	0.031	0.057	0.041
Digital	t_{up}/T	–	–	0.019	0.013
	h_2/h_1	–	–	0.034	0.066
	K	–	–	0.025	0.032
Femoral	t_{up}/T	–	0.008	–	0.017
	h_2/h_1	–	0.074	–	0.065
	K	–	0.038	–	0.033

TABLE 5 | ICC of the derived parameters.

	Parameter					
Sensor type	t_{up}	t_i	t_{up}/T	h_2/h_1	h_3/h_1	**SER**
PESG	**0.86**	**0.79**	0.72	0.68	0.65	0.64
Tonometer	**0.88**	**0.91**	**0.91**	**0.92**	**0.88**	**0.98**
Optical probe	**0.80**	0.72	0.70	0.64	0.46	0.51
Accelerometer	**0.88**	**0.82**	**0.87**	**0.89**	**0.91**	**0.84**

Bold text indicates the items with better results and performance.

radial and femoral sites. The analysis below was confined to data from the radial artery because this location is more convenient for measurements of contact force.

The Effect of Ambient Light Intensity on the Pulse Wave

For the optical sensor, it was found that the amplitude of the main peak was significantly correlated with the intensity of the ambient light ($r = 0.26$, $P < 0.05$). Since the other sensors detected either pressure or acceleration, the ambient light intensity had no effect.

Stability Analysis

As shown in **Table 5**, the ICC results obtained by the tonometer were in the range 0.88–0.98. For the accelerometer the corresponding figures were 0.82–0.91, so the stability of these two sensors was good. The ICC results obtained for the PESG were between 0.64 and 0.86, suggesting a moderate level of stability and the results obtained for the optical sensor ranged between 0.46 and 0.80, implying only poor stability.

Reproducibility Analysis

Intra-Observer Reproducibility

Table 6 shows that the ICC of the frequency and time domain parameters obtained from the tonometer and accelerometer was >0.75, implying good reproducibility. The ICC results obtained from the optical probe and PESG were as follows: ICC (SER) was <0.75, ICC (t_{up}, t_i, and t_{up}/T) was >0.75, and ICC (h_2/h_1, h_3/h_1) was between 0.40 and 0.75, indicating poor reproducibility. The shapes of the acquired waves were assessed by measuring the magnitude and timing of several fiducial points and further compared by a DTW approach (von Wowern et al., 2015). The intra-observer reproducibility was assessed by the DTW method as described in below.

TABLE 6 | ICC of the parameters in the time and frequency domains for intra-observer reproducibility.

	Parameter					
Sensor type	t_{up}	t_i	t_{up}/T	h_2/h_1	h_3/h_1	**SER**
PESG	**0.82**	**0.88**	**0.91**	0.62	0.64	0.71
Tonometer	**0.80**	**0.93**	**0.89**	**0.92**	**0.89**	**0.78**
Optical probe	**0.80**	**0.82**	**0.80**	0.42	0.50	0.61
Accelerometer	**0.85**	**0.88**	**0.92**	**0.95**	**0.96**	**0.84**

Bold text indicates the items with better results and performance, having good reproducibility.

TABLE 7 | ICC of the parameters in the time and frequency domains for inter-observer reproducibility.

	Parameter					
Sensor type	t_{up}	t_i	t_{up}/T	h_2/h_1	h_3/h_1	**SER**
PESG	**0.9**	**0.87**	0.43	0.61	0.47	0.55
Tonometer	**0.96**	**0.83**	**0.80**	0.52	0.65	**0.86**
Optical probe	**0.92**	**0.89**	**0.92**	**0.81**	0.66	**0.96**
Accelerometer	**0.92**	**0.90**	**0.80**	**0.80**	**0.82**	**0.97**

Bold text indicates the items with better results and performance, having good reproducibility.

Inter-Observer Reproducibility

Table 7 shows that the ICC of the frequency and time domain parameters obtained from the accelerometer was >0.80, implying good reproducibility. The ICC results obtained from the tonometer sensor, optical probe, and PESG were as follows: ICC (t_{up}/T, h_2/h_1, h_3/h_1, and SER) of PESG was <0.75, indicating moderate reproducibility. ICC (t_{up}, t_i, t_{up}/T, and SER) of tonometer was >0.80, ICC (t_{up}, t_i, t_{up}/T, h_2/h_1, and SER) of optical probe and tonometer was >0.80, indicating good reproducibility.

Morphological Analysis of the Entire Waveform

In this study the DTW method was used to compare two pulse trains captured successively by a single observer, from which intra-observer reproducibility was quantified.

The DTW distance is defined as (Izakian et al., 2015):

$$\mathrm{DTW}(X_n, Y_m) = d(x_n, y_m) + \min\{\mathrm{DTW}(X_{n-1}, Y_m), \mathrm{DTW}(X_{n-1}, Y_{m-1}), \mathrm{DTW}(X_n, Y_{m-1})\} \quad (8)$$

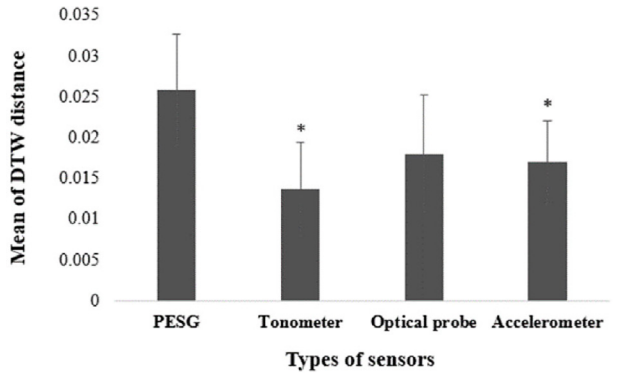

FIGURE 4 | Mean of DTW distance measured with the four sensors [* marks significant differences in comparison with PESG ($p < 0.05$)].

where d is a distance matrix in which each element $d(x_i, y_j)$ represents the distance between two sample points (x_i, y_j) from the signal $X_n = [x_1, x_2, \ldots, x_n]$ and $Y_m = [y_1, y_2, \ldots, y_m]$.

To test if there were significant differences in the calculated mean and standard deviation of the DTW distance using ANOVA, 20 groups of left radial artery data from the same subject were collected by the same observer using the four sensors, as shown in **Figure 4**. The mean value of the DTW distance of the PESG was the largest, at 0.026 ± 0.007; the optical sensor ranked second, at 0.018 ± 0.007; the accelerometer ranked third, at 0.017 ± 0.005; and the tonometer was the smallest, at 0.014 ± 0.006. The ANOVA results showed that the optical sensor was not significantly different when compared to the PESG on DTW distance ($p = 0.08$), and that the DTW values for the tonometer and accelerometer were significantly lower than that of the PESG ($p < 0.05$). This suggests that the intra-observer reproducibility of the overall waveform shape acquired by the tonometer was the highest, the accelerometer ranked second, the optical sensor ranked third, and the PESG device had the lowest reproducibility.

Analysis of the Timing and Amplitude Parameters

Figure 5 shows the waveforms from the four sensors recorded from one beat of the same subject (the sensors were used in the sequence: PESG, tonometer, optical sensor, and accelerometer) and normalized in amplitude and time. It can be seen that the dicrotic notch in the waves acquired by the PESG, tonometer, and accelerometer was more prominent than that acquired by the optical sensor. The post-systolic pressure wave acquired by the optical probe was much less prominent that that generated by the other probes. The detailed differences between the waveforms acquired by the four sensors are discussed below.

As shown in **Table 8**, the mean and low SD values of the parameters obtained from the radial artery by four sensors for 60 subjects, and by the relatively small error bars (**Figure 6**), the beat-to-beat variability of t_{up}, t_{up}/T was small, the coefficients of variation being <3%, and the reproducibility of these parameters was good. A slightly larger variability was shown by t_i, SER, and k-values. The coefficients of variation were 6–8%, and the reproducibility was medium. A larger variability was observed for h_2/h_1. The coefficients of variation were 10–15%, and the reproducibility was poor. The similarity of the feature parameters acquired by the four sensors was poor, and the measurement difference of h_2/h_1, h_3/h_1, SER, and k-values was obvious.

DISCUSSION

We analyzed signals recorded over the radial, carotid, digital, and femoral arteries of 60 subjects with four sensors, and extracted seven pulse wave parameters: t_{up}, t_i, t_{up}/T, h_2/h_1, h_3/h_1, K-values, and SER. The reason for selecting these parameters is that t_{up}, t_i, and t_{up}/T can reflect the degree of atherosclerosis (Weber et al., 2010); h_2/h_1 and h_3/h_1 can reflect the level of peripheral resistance (Korpas et al., 2009); the K-value can reflect changes in blood flow variables, such as peripheral resistance, vascular wall elasticity, and blood viscosity, and thus can independently detect the presence of cardiovascular disease. Finally, SER has been used to discriminate between healthy subjects and those with gastrointestinal disorders, which are characterized by significant differences in the SER power spectra (Thakker and Vyas, 2010).

External Factors Influencing Sensor Performance

We also analyzed the effect of some external factors (i.e., contact force, measuring site, and ambient light intensity) that affect signal shape and quality. The PESG can measure the contact force quantitatively, while the contact force exerted by the other sensors can only be assessed subjectively by the operator, unless mounted above a pressure sensor, as described in this study. We observed significant differences in pulse wave morphology among the three levels of applied force (light, medium, and heavy). As the force increases from light to medium, peak to peak amplitude of the signal increases. However, a further increase of contact force reduces the peak to peak amplitude. These findings are consistent with those of Thakker et al. (2010) and Teng and

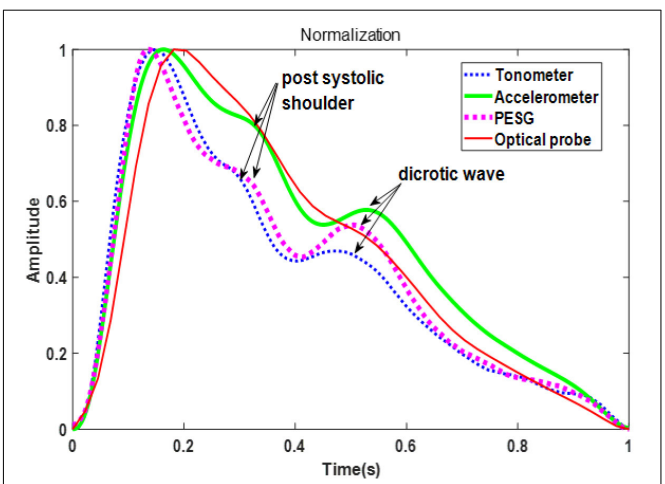

FIGURE 5 | Comparison of the normalized waveforms from each sensor.

TABLE 8 | Comparison of the mean ± SD of the parameters obtained by all four sensors for all subjects.

	Parameter						
Sensor type	t_{up}	t_i	t_{up}/T (%)	h_2/h_1 (%)	h_3/h_1 (%)	SER (%)	k
PESG	0.12 ± 0.01	0.35 ± 0.01	13.21 ± 0.1	47.14 ± 4.02	57.58 ± 2.3	69.26 ± 5.26	0.42 ± 0.03
Tonometer	0.12 ± 0.01	0.32 ± 0.01	16.68 ± 0.3	43.30 ± 4.1	47.33 ± 3.2	93.93 ± 1.87	0.37 ± 0.03
Optical probe	0.13 ± 0.02	0.30 ± 0.01	19.63 ± 0.34	56.98 ± 5.97	56.98 ± 5.97	79.28 ± 7.9	0.40 ± 0.06
Accelerometer	0.12 ± 0.01	0.32 ± 0.01	16.69 ± 0.49	51.76 ± 4.64	57.79 ± 3.28	66.51 ± 5.23	0.47 ± 0.03

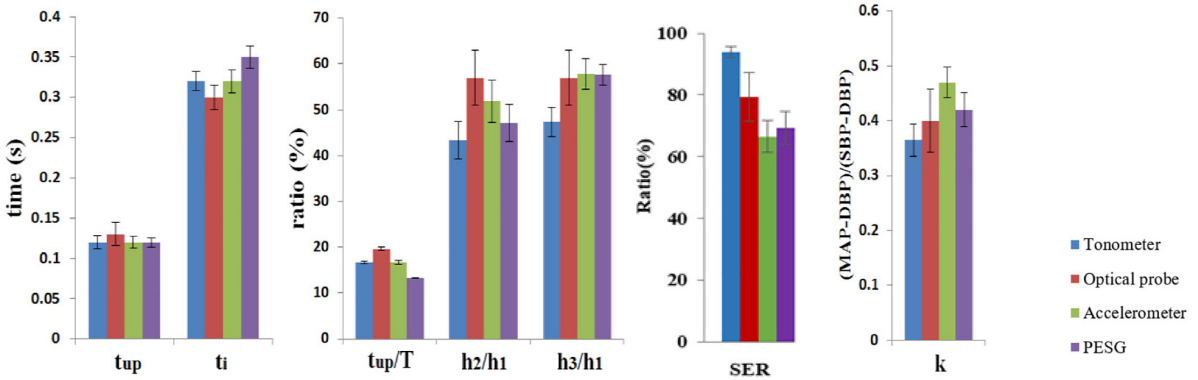

FIGURE 6 | Comparison of the mean ± SD of the parameters obtained by all four sensors for all subjects.

Zhang (2004). Further theoretical work by Teng and colleagues has shown that not only is the amplitude of the PPG signal dependent on probe pressure but also is its timing with respect to the arterial pulse. They found that pulse transit times increased with increasing pressure, until the transmural pressure was zero and that there was little further change as the probe pressure exceeded the arterial pressure and the transmural pressure thus became negative (Teng and Zhang, 2006, 2007). Given the strong effect of probe contact pressure on the shape and timing of the arterial pulse wave it is clearly important to establish an optimal and widely accepted standard for measurements of this type. This has been suggested by others for PPG measurements (Grabovskis et al., 2013), but there have been few reports describing the effect of contact pressure on tonometric recordings. Indeed, signal optimization in commercial tonometry systems is left in the hands of the experienced operator.

Not surprisingly, we observed that the quality of pulse wave measurement is affected by the measuring site. The finding is consistent with those of Hartmann et al. (2019). The stability of the pulse wave obtained from the carotid artery is worse than that of the radial artery (Adji et al., 2006). The accelerometer can obtain pulse wave signals at multiple measurement sites, and the tonometer is able to obtain pulse waves from the radial and femoral arteries. However, for PWV dual-channel acquisition devices the usefulness of radial artery measurements is limited, because carotid–radial PWV is not a good marker of large artery stiffness or, therefore, of general vascular health. Furthermore, because of the limitations of the experimental equipment in this study, the analysis approach adopted here, while of value to those concerned with analyzing the shape of the pulse wave, is of limited utility for PWV measurements. Nevertheless, there is value in using the radial pulse in PWV measurements because it has been shown that when combined with signals from the ankle, this ankle brachial "PWV" (abPWV) is significantly correlated with more direct measurement of large artery elasticity, such as carotid femoral PWV (Sugawara et al., 2005), and may even be more strongly correlated with overall cardiovascular health than carotid–femoral PWV. Therefore, because abPWV is easier to measure with simple and inexpensive equipment, it could be more suitable than carotid–femoral PWV for large-scale screening of at-risk populations in spite of the obvious theoretical drawback that abPWV is not a true velocity: in the sense that the distance used to calculate the velocity from the pulse transit time is not the actual distance traveled by the pulse.

Another important use of the radial artery pulse, especially when measured by tonometry, is as an adjunct to peripherally obtained blood pressure in monitoring hypertensive patients. Using the so-called generalized inverse transfer function, this approach can compensate for the amplification of the peripheral pressure pulse and not only obtain aortic pressure but also visualize the central pulse waveform (O'Rourke et al., 2001). It is also used in the measurement of PWV clinically (Yoon et al., 2000; O'Rourke and Seward, 2006; Salvi et al., 2008).

It was found that the optical sensor is affected by ambient light intensity, but available PPG systems commonly compensate electronically for changes in ambient light by alternately sampling the ambient light and the biological signal and subtracting the

former from the latter (Rajaguru and Prabhakar, 2015) so this problem is minimized, although not entirely absent. Therefore, in practice it is prudent, when using optical probes, to minimize the problem by carrying out measurements under constant artificial light.

Most of the energy in cardiovascular signals (excluding ECG) is found at frequencies below 20 Hz (Wang and Xiang, 2002; Wei and Chow, 2007). Therefore, a sampling frequency of no <40 Hz should be adequate to faithfully reproduce all information of pathophysiological interest. Thus, for the optical sensor, the manufacturer's choice of 70 Hz, although unusual, is more than adequate to reproduce the signal faithfully enough for analyzing its shape. Of course, this sampling rate is not adequate when measuring pulse transit times in the order of a few tens of milliseconds. In this study we have not measured pulse transit times although in future work concerning PWV the sample rate would have to be increased or another device used.

Stability and Reproducibility

In terms of stability and reproducibility, the tonometer is superior to the other sensors, but it still has some shortcomings. For instance, unlike wristband or finger sensors, it normally functions as a hand-held device, thus requiring the operator to keep the probe static during the measurement period. As mentioned above, the effect of pressure to the skin and underlying artery has a strong effect on the signal characteristics. The acceleration sensor is integrated with a multi-channel data acquisition system (Nelson et al., 2010) and can simultaneously obtain pulse wave signals from multiple measurement sites, while the hardware supplied with the other sensors used in this study allows single channel use only.

Morphological analysis shows that there is a significant difference between the waveforms acquired by the four sensors. This is not unexpected as they are measuring different physical properties. The optical sensor, for instance, is detecting blood volume changes in micro-vessels (Challoner, 1979; Wang et al., 2014), although PPG pulse sensors produce their strongest signals when positioned over large superficial arteries, which suggests that under these conditions their movement greatly augments the micro-vessel signals (Loukogeorgakis et al., 2002).

Photoplethysmographic technology has widespread clinical application and has been used in commercially available medical devices for measuring oxygen saturation, vascular assessment, assessing autonomic function, and also detecting peripheral vascular disease (Allen, 2007; Gil et al., 2010). The accelerometer detects skin movement where the skin is minimally loaded, and the two pressure sensors derive their signals directly from the blood pressure in the large arteries on which they are pressing. Piezoresistive and piezoelectric sensors can be easily implemented in various wearable devices, which can detect subtle physiological signal changes before and after exercise (Luo et al., 2016).

The PESG is used in the quantitative analysis of pulse characteristics and can investigate changes in the shape of the pulse waves under varying contact pressure (Luo et al., 2012; Bae et al., 2013; Chu et al., 2014), while the contact force exerted by the other sensors can only be assessed subjectively by the operator. The acceleration sensor has been applied to simultaneously obtain pulse wave signals at multiple measurement sites (Gardosi et al., 1991), and wearable optical pulse sensors have been commercially developed (Tamura et al., 2014). To fully exploit the advantages of each type of measurement system it would be useful to develop a versatile data acquisition unit compatible with a variety of sensor types including but possibly not limited to those described here.

CONCLUSION

The above results show that firstly, the effect of contact pressure, measuring site, and ambient light on the pulse wave should be considered when carrying out measurements on patients. Secondly, comparison of the four kinds of pulse wave sensors shows that, overall, the performance of the tonometer is the best, the accelerometer ranks second, the PESG, third, and the optical sensor is the poorest. Finally, there is significant difference among the four sensors in their waveform shapes and the timing and amplitude parameters.

In terms of stability and reproducibility, the tonometer is superior to the others although it normally functions as a hand-held device. Unlike wristband or digital sensors for instance, it requires the operator to keep the probe static during the measurement period. Furthermore, the tonometer is not equipped to measure the contact pressure so this can only be assessed subjectively by the operator. However, in practice, different sensor types could be used, perhaps in combination according to the measurement site and the nature of the required signal analysis and in this way, the advantages of each can be more easily exploited.

Recommendation

Researchers can reasonably select sensor types according to their own experimental requirements. Obviously, the main factor determining choice of sensor type and measurement position is what type of cardiovascular pathology is being investigated: central or peripheral disease, response to treatment acute measurements, or longer-term monitoring. In addition, when the data are being recorded, external factors that affect the experimental results, such as contact pressure, measurement position, ambient light, etc., need to be considered to rationally design the experimental environment. For the assessment of arterial stiffness, by measuring PWV, consensus documents have been published which specify the optimal measuring sites, how to measure path length, and acceptable levels of repeatability (Laurent et al., 2006; Wilkinson, 2010; Van Bortel et al., 2012). However, in other areas, such as the general field of analyzing the shape of the pulse wave or the assessment of peripheral arterial disease there remains a lack of authoritative guidelines.

DATA AVAILABILITY STATEMENT

All datasets generated for this study are included in the article/supplementary material.

ETHICS STATEMENT

The studies involving human participants were reviewed and approved by the Ethics Committee of Medicine and Biomedical Information Engineering College, Northeastern University, Shenyang, China. The patients/participants provided their written informed consent to participate in this study.

AUTHOR CONTRIBUTIONS

HW and NS contributed to the conception and design of the study and wrote the manuscript. LX and SG contributed to the manuscript revision, read, and approved the submitted version of the manuscript. YY, LW, and LH provided some suggestions. All authors contributed to the manuscript revision, read, and approved the submitted version of the manuscript.

FUNDING

The research reported here was, in part, supported by the National Natural Science Foundation of China (Nos. 61773110, 61374015, and 61701099), and the Fundamental Research Funds for the Central Universities (Nos. N161904002 and N172008008). This work was also supported by the Open Program of Neusoft Research of Intelligent Healthcare Technology, Co. Ltd., Item No. NRIHTOP1801. The authors declare that this study received funding from the Open Program of Neusoft Research of Intelligent Healthcare Technology, Co. Ltd., and the funders had no role in study design, data collection and analysis, decision to publish, or preparation of the manuscript.

REFERENCES

Adji, A., Hirata, K., and O'rourke, M. F. (2006). Clinical use of indices determined non-invasively from the radial and carotid pressure waveforms. *Blood Press. Monit.* 11, 215–221. doi: 10.1097/01.mbp.0000218001.50333.b7

Allen, J. (2007). Photoplethysmography and its application in clinical physiological measurement. *Physiol. Meas.* 28, R1–R39.

Bae, J.-H., Jeon, Y. J., Kim, J. Y., and Kim, J. U. (2013). New assessment model of pulse depth based on sensor displacement in pulse diagnostic devices. *Evid. -Based Complement. Alternat. Med.* 2013:938641. doi: 10.1155/2013/938641

Bland, J. M., and Altman, D. (1986). Statistical methods for assessing agreement between two methods of clinical measurement. *Lancet* 327, 307–310. doi: 10.1016/s0140-6736(86)90837-8

Boutry, C. M., Nguyen, A. K., Lawal, Q. O., Chortos, A., Rondeau-Gagn, S., and Bao, Z. (2015). A Sensitive and Biodegradable Pressure Sensor Array for Cardiovascular Monitoring. *Adv. Mater.* 27, 6954–6961. doi: 10.1002/adma.201502535

Challoner, A. (1979). Photoelectric plethysmography for estimating cutaneous blood flow. *NonInvasive Physiol. Meas.* 1, 125–151.

Chen, C.-H., Nevo, E., Fetics, B., Pak, P. H., Yin, F. C., Maughan, W. L., et al. (1997). Estimation of central aortic pressure waveform by mathematical transformation of radial tonometry pressure: validation of generalized transfer function. *Circulation* 95, 1827–1836. doi: 10.1161/01.cir.95.7.1827

Chen, Y., Lu, B., Chen, Y., and Feng, X. (2016). Biocompatible and Ultra-Flexible inorganic strain sensors attached to skin for long-term vital signs monitoring. *IEEE Electron Device Lett.* 37, 496–499. doi: 10.1109/led.2016.2536036

Chu, Y.-W., Luo, C.-H., Chung, Y.-F., Hu, C.-S., and Yeh, C.-C. (2014). Using an array sensor to determine differences in pulse diagnosis—Three positions and nine indicators. *Eur. J. Integr. Med.* 6, 516–523. doi: 10.1016/j.eujim.2014.04.003

Clemente, F., Arpaia, P., and Cimmino, P. (2010). A piezo-film-based measurement system for global haemodynamic assessment. *Physiol. Meas.* 31, 697–714. doi: 10.1088/0967-3334/31/5/007

Crilly, M., Coch, C., Bruce, M., Clark, H., and Williams, D. (2007a). Indices of cardiovascular function derived from peripheral pulse wave analysis using radial applanation tonometry: a measurement repeatability study. *Vasc. Medi.* 12, 189–197. doi: 10.1177/1358863x07081134

Crilly, M., Coch, C., Clark, H., Bruce, M., and Williams, D. (2007b). Repeatability of the measurement of augmentation index in the clinical assessment of arterial stiffness using radial applanation tonometry. *Scand. J. Clin. Lab. Investig.* 67, 413–422. doi: 10.1080/00365510601131946

Elgendi, M. (2014). Detection of c, d, and e waves in the acceleration photoplethysmogram. *Comput. Methods Programs Biomed.* 117, 125–136. doi: 10.1016/j.cmpb.2014.08.001

Gardosi, J., Schram, C., and Symonds, E. (1991). Adaptation of pulse oximetry for fetal monitoring during labour. *Lancet* 337, 1265–1267. doi: 10.1016/0140-6736(91)92928-u

Gil, E., Orini, M., Bailon, R., Vergara, J. M., Mainardi, L., and Laguna, P. (2010). Photoplethysmography pulse rate variability as a surrogate measurement of heart rate variability during non-stationary conditions. *Physiol. Meas.* 31, 1271–1290. doi: 10.1088/0967-3334/31/9/015

Grabovskis, A., Marcinkevics, Z., Rubins, U., and Kviesis-Kipge, E. (2013). Effect of probe contact pressure on the photoplethysmographic assessment of conduit artery stiffness. *J. Biomed. Opt.* 18:027004. doi: 10.1117/1.JBO.18.2.027004

Hartmann, V., Liu, H., Chen, F., Qiu, Q., Hughes, S., and Zheng, D. (2019). Quantitative comparison of photoplethysmographic waveform characteristics: effect of measurement site. *Front. Physiol.* 10:198. doi: 10.3389/fphys.2019.00198

He, D., Wang, L., Fan, X., Yao, Y., and Qian, W. (2017). A new mathematical model of wrist pulse waveforms characterizes patients with cardiovascular disease – A pilot study. *Med. Eng. Phys.* 48, 142–149. doi: 10.1016/j.medengphy.2017.06.022

Hertzman, A. B. (1937). Observations on the finger volume pulse recorded photoelectrically. *Am. J. Physiol.* 119, 334–335.

Huotaril, M., Vehkaojaz, A., Maattal, K., Kostamovaaral, J., and Roningl, J. (2013). Arterial pulse waves measured with EMFi and PPG sensors and comparison of the pulse waveform spectral and decomposition analysis in healthy young and elderly subjects. *Model Med. Biol.* 17, 3–11.

Izakian, H., Pedrycz, W., and Jamal, I. (2015). Fuzzy clustering of time series data using dynamic time warping distance. *Eng. Appl. Artif. Intell.* 39, 235–244. doi: 10.1371/journal.pone.0197499

Jeong, Y.-S., and Jayaraman, R. (2015). Support vector-based algorithms with weighted dynamic time warping kernel function for time series classification. *Knowl. Based Syst.* 75, 184–191. doi: 10.1016/j.knosys.2014.12.003

Kamshilin, A. A., Sidorov, I. S., Babayan, L., Volynsky, M. A., Giniatullin, R., and Mamontov, O. V. (2016). Accurate measurement of the pulse wave delay with imaging photoplethysmography. *Biomed. Opt. Express.* 7, 5138–5147. doi: 10.1364/BOE.7.005138

Kemmotsu, O., Ohno, M., Takita, K., Sugimoto, H., Otsuka, H., Morimoto, Y., et al. (1994). Noninvasive, continuous blood pressure measurement by arterial tonometry during anesthesia in children. *Anesthesiology* 81, 1162–1168. doi: 10.1097/00000542-199411000-00009

Korpas, D., Halek, J., and Doležal, L. (2009). Parameters describing the pulse wave. *Physiol. Res.* 58, 473–479.

Laurent, S., Cockcroft, J., Van Bortel, L., Boutouyrie, P., Giannattasio, C., Hayoz, D., et al. (2006). Expert consensus document on arterial stiffness: methodological issues and clinical applications. *Eur. Heart J.* 27, 2588–2605. doi: 10.1093/eurheartj/ehl254

Li, K., Zhang, S., Yang, L., Jiang, H., Chi, Z., Wang, A., et al. (2018). Changes of arterial pulse waveform characteristics with gestational age during normal pregnancy. *Sci. Rep.* 8:15571. doi: 10.1038/s41598-018-33890-1

Loukogeorgakis, S., Dawson, R., Phillips, N., Martyn, C. N., and Greenwald, S. E. (2002). Validation of a device to measure arterial pulse wave velocity by a photoplethysmographic method. *Physiol. Meas.* 23, 581–596. doi: 10.1088/0967-3334/23/3/309

Lovinsky, L. S. (2006). Urgent problems of metrological assurance of optical pulse oximetry. *IEEE Trans. Instrum. Meas.* 55, 869–875. doi: 10.1109/tim.2006.873784

Lukas, P., Norbert, N., and Cerny, M. (2014). A review of methods for non-invasive and continuous blood pressure monitoring: Pulse transit time method is promising? *IRBM* 35, 271–282. doi: 10.3390/jcm8111827

Luo, C.-H., Chung, Y.-F., Hu, C.-S., Yeh, C.-C., Si, X.-C., Feng, D.-H., et al. (2012). Possibility of quantifying TCM finger-reading sensations: I. Bi-sensing pulse diagnosis instrument. *Eur. J. Integr. Med.* 4, e255–e262. doi: 10.1016/j.eujim.2012.03.003

Luo, N., Dai, W., Li, C., Zhou, Z., and Ni, Z. (2016). Flexible piezoresistive sensor patch enabling ultralow power cuffless blood pressure measurement. *Adv. Func. Mater.* 26, 1178–1187. doi: 10.1002/adfm.201504560

Luo, Z.-C., Zhang, S., and Yang, Y. (2006). *Engineering Analysis for Pulse Wave and Its Application in Clinical Practice*. Beijing: Science Press.

Ma, Z.-C., Zhang, Y.-L., Ni, C.-M., He, Z.-J., Cao, Q.-Q., and Sun, Y.-N. (2013). A new method for determining subendocardial viability ratio from radial artery pressure waves. *J. Mech. Med. Biol.* 13:1350060. doi: 10.1142/s0219519413500607

Mackenzie, B. J. (1902). The study of the pulse, arterial, venous, and hepatic, and of the movements of the heart. *Indian Med. Gaz.* 37, 287–287.

Mallat, S. E. G. (1989). A theory of multiresolution signal decomposition: the wavelet representation. *IEEE Trans. Patt. Analytic. Mach. Intell.* 11, 674–639.

Meidert, A. S., Huber, W., Muller, J. N., Schofthaler, M., Hapfelmeier, A., Langwieser, N., et al. (2014). Radial artery applanation tonometry for continuous non-invasive arterial pressure monitoring in intensive care unit patients: comparison with invasively assessed radial arterial pressure. *Br. J. Anaesth.* 112, 521–528. doi: 10.1093/bja/aet400

Muehlsteff, J., Dellimore, K., Aarts, V., Derkx, R., Peiker, C., and Meyer, C. (2015). "Pulse detection with a single accelerometer placed at the carotid artery: performance in a real-life diagnostic test during acute hypotension," in *Proceedings of the International Conference of the IEEE Engineering in Medicine and Biology Society*, Milan, 434–437.

Murphy, J. C., Morrison, K., Mclaughlin, J., Manoharan, G., and Adgey, A. A. J. (2011). An innovative piezoelectric-based method for measuring pulse wave velocity in patients with hypertension. *J. Clin. Hypertens.* 13, 497–505. doi: 10.1111/j.1751-7176.2011.00433.x

Nelson, M. R., Stepanek, J., Cevette, M., Covalciuc, M., Hurst, R. T., and Tajik, A. J. (2010). Noninvasive measurement of central vascular pressures with arterial tonometry: clinical revival of the pulse pressure waveform? *Mayo. Clin. Proc.*. 85, 460–472. doi: 10.4065/mcp.2009.0336

O'Rourke, M. F. (2016). Carotid artery tonometry: pros and cons. *Am. J. Hypertens.* 29, 296–298.

O'Rourke, M. F., Pauca, A., and Jiang, X. J. (2001). Pulse wave analysis. *Br. J. Clin. Pharmacol.* 51:S147.

O'Rourke, M. F., and Seward, J. B. (2006). Central arterial pressure and arterial pressure pulse: new views entering the second century after Korotkov. *Mayo Clin. Proc.* 81, 1057–1068. doi: 10.4065/81.8.1057

Papaioannou, T. G., Karageorgopoulou, T. D., Sergentanis, T. N., Protogerou, A. D., Psaltopoulou, T., Sharman, J. E., et al. (2016). Accuracy of commercial devices and methods for noninvasive estimation of aortic systolic blood pressure a systematic review and meta-analysis of invasive validation studies. *J. Hypertens.* 34, 1237–1248. doi: 10.1097/HJH.0000000000000921

Papaioannou, T. G., Karatzis, E. N., Karatzi, K. N., Gialafos, E. J., Protogerou, A. D., Stamatelopoulos, K. S., et al. (2007). Hour-to-hour and week-to-week variability and reproducibility of wave reflection indices derived by aortic pulse wave analysis: implications for studies with repeated measurements. *J. Hypertens.* 25, 1678–1686. doi: 10.1097/hjh.0b013e3281ab6c58

Perloff, D., Grim, C., Flack, J., Frohlich, E. D., Hill, M., Mcdonald, M., et al. (1993). Human blood pressure determination by sphygmomanometry. *Circulation* 88, 2460–2470. doi: 10.1161/01.cir.88.5.2460

Rajaguru, H., and Prabhakar, S. K. (2015). A comprehensive review on photoplethysmography and its application for heart rate turbulence clinical diagnosis. *Adv. Sci. Lett.* 21, 3602–3604. doi: 10.1166/asl.2015.6541

Salvi, P., Magnani, E., Valbusa, F., Agnoletti, D., Alecu, C., Joly, L., et al. (2008). Comparative study of methodologies for pulse wave velocity estimation. *J. Hum. Hypertens.* 22, 669–677. doi: 10.1038/jhh.2008.42

Schafer, A., and Vagedes, J. (2013). How accurate is pulse rate variability as an estimate of heart rate variability? A review on studies comparing photoplethysmographic technology with an electrocardiogram. *Int. J. Cardiol.* 166, 15–29. doi: 10.1016/j.ijcard.2012.03.119

Stea, F., Bozec, E., Millasseau, S., Khettab, H., Boutouyrie, P., and Laurent, S. (2014). Comparison of the complior analyse device with sphygmocor and complior SP for pulse wave velocity and central pressure assessment. *J. Hypertens.* 32, 873–880. doi: 10.1097/HJH.0000000000000091

Sugawara, J., Hayashi, K., Yokoi, T., Cortez-Cooper, M. Y., DeVan, A. E., Anton, M. A., et al. (2005). Brachial-ankle pulse wave velocity: an index of central arterial stiffness? *J. Hum. Hypertens.* 19, 401–406.

Tamura, T., Maeda, Y., Sekine, M., and Yoshida, M. (2014). Wearable photoplethysmographic sensors—past and present. *Electronics* 3, 282–302. doi: 10.3390/electronics3020282

Teng, X. F., and Zhang, Y. T. (2004). The effect of contacting force on photoplethysmographic signals. *Physiol. Meas.* 25:1323. doi: 10.1088/0967-3334/25/5/020

Teng, X. F., and Zhang, Y. T. (2006). The effect of applied sensor contact force on pulse transit time. *Physiol. Meas.* 27, 675–684. doi: 10.1088/0967-3334/27/8/002

Teng, X. F., and Zhang, Y.-T. (2007). Theoretical study on the effect of sensor contact force on pulse transit time. *IEEE Trans. BioMed. Eng.* 54:1490. doi: 10.1109/tbme.2007.900815

Thakker, B., and Vyas, A. L. (2010). "Frequency domain analysis of radial pulse in abnormal health conditions," in *2010 IEEE EMBS Conference on Biomedical Engineering and Sciences* (Kuala Lumpur).

Thakker, B., Vyas, A. L., and Tripathi, D. (2010). "Radial pulse analysis at deep pressure in abnormal health conditions," in *2010 3rd International Conference on Biomedical Engineering and Informatics* (Yantai).

Townsend, R. R., Black, H. R., Chirinos, J. A., Feig, P. U., Ferdinand, K. C., Germain, M., et al. (2015). Clinical use of pulse wave analysis: proceedings from a symposium sponsored by North American Artery. *J. Clin. Hypertens.* 17, 503–513. doi: 10.1111/jch.12574

Van Bortel, L. M., Stephane, L., Pierre, B., Phil, C., Cruickshank, J. K., Tine, D. B., et al. (2012). Expert consensus document on the measurement of aortic stiffness in daily practice using carotid-femoral pulse wave velocity. *J. Hypertens.* 30, 445–458. doi: 10.1097/HJH.0b013e32834fa8b0

von Wowern, E., stling, G., Nilsson, P. M., and Olofsson, P. (2015). Digital photoplethysmography for assessment of arterial stiffness: repeatability and comparison with applanation tonometry. *PloS one* 10:e0135659. doi: 10.1371/journal.pone.0135659

Wang, B., and Xiang, J. (2002). Detecting system and power-spectral analysis of pulse signals of human body. *Fourth Int. Conf. Signal Proc.*. 2, 1646–1649.

Wang, D., Zhang, D., and Lu, G. (2015). An optimal pulse system design by multichannel sensors fusion. *IEEE J. f Biomed. Health Inform.* 20, 450–459. doi: 10.1109/JBHI.2015.2392132

Wang, L., Xu, L., Feng, S., Meng, Q. H., and Wang, K. (2013). Multi-Gaussian fitting for pulse waveform using weighted least squares and multi-criteria decision making method. *Comput. Biol. Med.* 43, 1661–1672. doi: 10.1016/j.compbiomed.2013.08.004

Wang, P., Zuo, W., and Zhang, D. (2014). A compound pressure signal acquisition system for multichannel wrist pulse signal analysis. *IEEE Trans. Instrum. Meas.* 63, 1556–1565. doi: 10.1109/tim.2013.2267458

Weber, T., O'rourke, M. F., Lassnig, E., Porodko, M., Ammer, M., Rammer, M., et al. (2010). Pulse waveform characteristics predict cardiovascular events

and mortality in patients undergoing coronary angiography. *J. Hypertens.* 28, 797–805. doi: 10.1097/HJH.0b013e328336c8e9

Wei, L. Y., and Chow, P. (2007). Frequency distribution of human pulse spectra. *IEEE Trans. Biomed. Eng.* 32, 245–246. doi: 10.1109/tbme.1985.325537

Wilkinson, I. B. (2010). ARTERY Society guidelines for validation of non-invasive haemodynamic measurement devices: part 1, arterial pulse wave velocity. *Artery Res.* 4, 34–40. doi: 10.1016/j.artres.2010.03.001

Xu, L., Yang, Y., Hao, W., Dianning, H., Lu, W., and Yongsheng, J. (2014). Morphology variability of radial pulse wave during exercise. *BioMed. Mater. Eng.* 24:3605. doi: 10.3233/BME-141187

Xu, L., Zhang, D., and Wang, K. (2005). Wavelet-based cascaded adaptive filter for removing baseline drift in pulse waveforms. *IEEE Trans. BioMed. Eng.* 52, 1973–1975. doi: 10.1109/tbme.2005.856296

Yang, X., Li, J., Hu, D., Chen, J., Li, Y., Huang, J., et al. (2016). Predicting the 10-year risks of atherosclerotic cardiovascular disease in Chinese Population: the China-PAR Project (Prediction for ASCVD Risk in China). *Circulation* 134, 1430–1440. doi: 10.1161/circulationaha.116.022367

Yao, Y., Hao, L., Xu, L., Zhang, Y., Qi, L., Sun, Y., et al. (2017). Diastolic augmentation index improves radial augmentation index in assessing arterial stiffness. *Sci Rep.* 7:5864. doi: 10.1038/s41598-017-06094-2

Yoon, Y.-Z., Lee, M.-H., and Soh, K.-S. (2000). Pulse type classification by varying contact pressure. *IEEE Eng. Med. Biol. Mag.* 19, 106–110. doi: 10.1109/51.887253

Zuo, W., Wang, P., and Zhang, D. (2016). Comparison of three different types of wrist pulse signals by their physical meanings and diagnosis performance. *IEEE J. Biomed. Health Inform.* 20, 119–127. doi: 10.1109/JBHI.2014.2369821

Conflict of Interest: LX was partly employed by Neusoft Research of Intelligent Healthcare Technology, Co. Ltd., Shenyang, China.

The remaining authors declare that the research was conducted in the absence of any commercial or financial relationships that could be construed as a potential conflict of interest.

frontiers in Physiology

ORIGINAL RESEARCH
published: 21 January 2020
doi: 10.3389/fphys.2019.01627

Association Between D-dimer and Early Adverse Events in Patients With Acute Type A Aortic Dissection Undergoing Arch Replacement and the Frozen Elephant Trunk Implantation: A Retrospective Cohort Study

Tong Liu[1†], Jun Zheng[2], You-Cong Zhang[2], Kai Zhu[2], Hui-Qiang Gao[2], Kai Zhang[2], Xiu-Feng Jin[2] and Shang-Dong Xu[2]*

[1] Department of Cardiology, Beijing Anzhen Hospital, Capital Medical University, Beijing, China, [2] Department of Cardiac Surgery, Beijing Aortic Disease Center, Beijing Anzhen Hospital, Capital Medical University, Beijing, China

OPEN ACCESS

Edited by:
Gerald A. Meininger,
University of Missouri, United States

Reviewed by:
Barbara Ruszkowska-Ciastek,
Nicolaus Copernicus University in Toruń, Poland
Sivareddy Kotla,
University of Texas MD Anderson Cancer Center, United States

***Correspondence:**
Shang-Dong Xu
xushangdong@126.com

[†]First author

Specialty section:
This article was submitted to Vascular Physiology, a section of the journal Frontiers in Physiology

Received: 17 August 2019
Accepted: 24 December 2019
Published: 21 January 2020

Citation:
Liu T, Zheng J, Zhang Y-C, Zhu K, Gao H-Q, Zhang K, Jin X-F and Xu S-D (2020) Association Between D-dimer and Early Adverse Events in Patients With Acute Type A Aortic Dissection Undergoing Arch Replacement and the Frozen Elephant Trunk Implantation: A Retrospective Cohort Study. Front. Physiol. 10:1627. doi: 10.3389/fphys.2019.01627

Objective: In the present study, we investigated the associations between D-dimer levels at admission and early adverse events in patients with acute type A aortic dissection undergoing arch replacement and the frozen elephant trunk (FET).

Methods: We retrospectively analyzed data of patients with acute type A aortic dissection undergoing aortic arch surgery and FET from July 2017 to December 2018 at Beijing Anzhen Hospital. D-dimer levels were evaluated within 24 h of admission. Multivariate Cox regression analysis was used to determine independent predictors of early postoperative adverse events.

Results: A total of 347 patients were included in the study. The average age of the patients was 48.07 ± 10.56 years, with male predominance (79.25%). The incidence of 90-day postoperative adverse events was 18.7%, consisting of 14.7% mortality and 4.0% permanent neurological dysfunction (PND). The median D-dimer level was 1.95 ug/ml (interquartile range, 0.77–3.16 ug/ml). Multivariable Cox regression analysis revealed that D-dimer level was independently associated with 90-day postoperative adverse events after adjustment for confounding factors (hazard ratio = 1.19 per 10 ug/ml increase in D-dimer, 95% confidence interval: 1.01–1.41; P = 0.039). Kaplan–Meier analysis revealed that the highest tertile (median 6.27 ug/ml) had more 90-day postoperative adverse events compared with the median and lowest tertiles (P = 0.0014). Sub-analysis found that the association remained unchanged.

Conclusion: Increased D-dimer levels at admission were associated with 90-day postoperative adverse events in patients with acute type A aortic dissection undergoing arch replacement and FET. These results may help clinicians optimize the risk evaluation and perioperative clinical management to reduce early adverse events.

Key Question: Explore the relationship between D-dimer and early outcomes in patients with aortic dissection with arch replacement.

Key Findings: Increased D-dimer at admission was associated with adverse events in patients with aortic dissection with arch surgery.

Take-Home Message: The high-risk patients deserve close medical monitoring.

Keywords: D-dimer, predictor, 90-day postoperative adverse events, aortic arch replacement, frozen elephant trunk

INTRODUCTION

The incidence of aortic dissection markedly increases with atherosclerosis and hypertension. Although surgical treatment significantly reduces the mortality of patients with aortic dissection compared with medical management, short-term mortality (30-day or in-hospital mortality) remains high (13–17%) (Mussa et al., 2016).

D-dimer, a specific degradation product of cross-linked fibrin, represents the coagulation and fibrinolytic system activation (Suzuki et al., 2009). It is now commonly used in the diagnosis of pulmonary embolism (van der Hulle et al., 2013), deep vein thrombosis (Faller et al., 2017), acute coronary syndrome (Bayes-Genis et al., 2000), and acute aortic dissection (Akutsu et al., 2005; Suzuki et al., 2009; Shao et al., 2014). For acute aortic dissection, the mechanisms of coagulation and fibrinolytic system activation might be (1) coagulant material from the aortic wall released into the circulation and (2) an accumulation of clotting factors at the site of the lesion, secondary to the local exposition of tissue factors from the torn arterial wall (Ten Cate et al., 1975). Thus, the D-dimer level is elevated in patients with acute aortic dissection. Weber et al. (2003) first observed that D-dimer levels tended to be higher in patients with acute aortic dissection, but no relation was observed between D-dimer levels and in-hospital outcome. On the other hand, Wen et al. (2013) and Huang et al. (2015) found that an elevated D-dimer level was associated with increased in-hospital mortality (Wen et al., 2013; Huang et al., 2015). Nevertheless, the sample size in these two previous studies was relatively small, and the largest sample size was 212 patients. Further, these study populations with aortic dissection not only underwent surgical treatment, but also medical treatment. In addition, few studies have evaluated the association between D-dimer levels and 90-day postoperative adverse events in patients with acute type A aortic dissection undergoing arch replacement and FET.

For these reasons, we conducted a retrospective cohort study to investigate the association between D-dimer levels and 90-day postoperative adverse events in patients undergoing arch replacement and FET using a multivariate Cox regression model containing all known associated major perioperative predictors. Our hypothesis was that the risk of 90-day postoperative adverse events would increase as D-dimer levels increased.

MATERIALS AND METHODS

Study Design and Study Population

From July 1, 2017, to December 31, 2018, consecutive patients with aortic disease undergoing aortic arch surgery were retrospectively identified at the aortic center in the Beijing Anzhen Hospital (Capital Medical University of Beijing, China). Patients with acute type A aortic dissection who underwent total arch replacement and the frozen elephant trunk (FET) technique were recruited into this observational retrospective cohort study. Patients who (1) underwent hemi-arch replacement (n = 31), (2) suffered from chronic aortic disease (n = 69), (3) had redo sternotomy (n = 19), (4) did not undergo the FET technique (n = 40), or (5) did not have D-dimer values (n = 4) were excluded.

Study Endpoint

The endpoint of this observational retrospective study was defined as early all-cause mortality or permanent neurological dysfunction (PND) during the hospital stay or within 90 days after surgery. PND was defined as the presence of permanent neurologic deficits, including abnormal movement of limbs, coma, and sensory loss affecting one side of the body, within postoperative 90-day. Confirmation of the diagnosis was made by a neurologist or by means of computed tomographic scanning or magnetic resonance imaging of the brain.

Definition and Procedure

The type of aortic dissection was classified according to Stanford classification (Daily et al., 1970). Acute dissection was defined as clinical symptoms lasting less than 14 days (Hagan et al., 2000). Hypertension was defined by a clinical record of systolic or diastolic blood pressure greater than 140 or 90 mmHg on admission, or the use of anti-hypertension drugs. Diabetes mellitus was defined as treatment with oral hypoglycemic agents or insulin, or as having a fasting blood glucose level $\geq$7.0 mmol/L (126 mg/dl). Smoking status was defined as smoking within

the preceding 1 year based on information in medical records. Renal insufficiency was defined as estimated glomerular filtration rate (eGFR) <60 mL/min per 1.73 m^2, calculated using the Chronic Kidney Disease Epidemiology Collaboration (CKD-EPI) equation (Levey et al., 2009). A diagnosis of cardiac artery disease was considered if patients had a history of myocardial infarction or previous PCI or coronary artery bypass grafting (CABG) before admission. Cerebrovascular disease was defined based on relevant neurologic dysfunction before admission or previous stroke. Pericardial tamponade was diagnosed by echocardiography. The details of total arch replacement and FET implantation have been described elsewhere by our team (Sun et al., 2011; Ma et al., 2013). In brief, the arch was opened under moderate hypothermia arrest (21∼28°C). An open stent-graft was deployed into the descending aorta. The arch was replaced with a four-branched vascular graft.

D-dimer Measurement

Within 24 h after admission, whole-blood samples were drawn into blood collection tubes containing sodium citrate (3.2%, 109 mmol/L) as the anticoagulant (9:1 ratio of blood:anticoagulant) to measure prothrombin time (PT), activated partial thromboplastin time (APTT), fibrin degradation products (FDP), and D-dimer. Venous blood was immediately sent to the clinical laboratory center of the Anzhen hospital. Plasma PT, APTT, FDP, and D-dimer were measured using the commercially available automated latex immunoturbidimetric assay (Werfen ACL TOP 700, United States) (Di Nisio et al., 2007; Wang et al., 2018). Routine blood tests and some biochemical indicators were determined by standard quantitative assay techniques, according to the manufacturers' instructions. All assays were run in duplicate.

Data Collected for Analysis

Clinical, operative, perfusion, and postoperative data have been retrospectively collected in a department database, and further data were extracted from operation reports, perfusion reports, intraoperative computerized records, and review of medical records. Data were compiled via the Empower Dataweb data collection management system (X&Y Solutions, Inc., Boston, MA, United States). The current study was approved by the Human Subjects Review Committee at Anzhen Hospital (Approval No. 2017058X). Follow-up data were obtained from medical records and telephone calls.

Statistical Analysis

Categorical variables were presented as frequencies or percentages, whereas continuous variables were expressed as means ± standard deviations (normal distribution) or medians and interquartile ranges (skewed distribution). First, we grouped D-dimer levels in tertiles. The significant differences between the means and proportions of the tertiles in baseline characteristics were analyzed using a Student's *t*-test or Mann–Whitney *U* test for continuous variables, as appropriate, and a chi-square test for categorical variables (**Table 1**). Second, univariate Cox regression analyses were used to evaluate the association between each significant variable and 90-day postoperative adverse events (**Supplementary Table**). Third, multivariate Cox regression models (**Table 2**) were used to examine whether D-dimer levels had an independent effect on 90-day postoperative adverse events. We simultaneously showed the results from unadjusted, minorly adjusted, and fully adjusted analyses. The covariates, when added to this model, changed the matched odds ratio by at least 10% (Kernan et al., 2000) and covariates of known clinical importance were adjusted. We expanded D-dimer levels 10 times and labeled them per 10 ug/mL change. Trend tests were based on D-dimer level tertiles as continuous variables. Fourth, survival estimates and cumulative event rates were compared using the Kaplan–Meier method by using the time-to-first event for each endpoint among D-dimer level tertiles. The log-rank test was used to compare the Kaplan–Meier hazard ratios (HR) for 90-day postoperative adverse events, and their corresponding 95% confidence intervals (CIs). Finally, subgroup analysis was done to find whether potential risk factors were influencing the results. The interactions of subgroups were inspected by multivariate adjusted Cox regression models (**Table 3**). All analyses were performed using Empower (R) ([1]X&Y Solutions, Inc.) and R[2].

RESULTS

From July 1, 2017, to December 31, 2018, 510 consecutive patients received aortic arch surgery at the cardiac surgery center in the Beijing Anzhen Hospital. We excluded patients who underwent hemi-arch replacement (n = 31), had chronic aortic disease (n = 69), underwent redo-sternotomy (n = 19), or did not have FET implantation (n = 40) (**Figure 1**).

Demographic Characteristics

The final analysis included 347 patients with acute type A aortic dissection who underwent total arch replacement and FET implantation (**Figure 1**). The median D-dimer value was 1.95 ug/mL, with an interquartile range of 0.77–3.16 ug/mL. The baseline demographic, clinical, operative, and perfusion characteristics are presented in **Table 1**. At admission, the mean age of the 347 patients was 48 years (48.07 ± 10.56), 275 (79.25%) were men. On echocardiography, the mean LVEF was 62.49 ± 5.43 and severe aortic regurgitation was identified in 51 (15.32%) patients at presentation. Moreover, 280 (80.69%) patients had previous hypertension, 13 (3.75%) had previous diabetes mellitus, 58 (16.71%) had chronic kidney dysfunction (CKD), 23 (6.63%) had coronary artery disease, and 20 (5.76%) had cerebrovascular disease. At admission, 26 (7.49%) patients presented with lower-extremity ischemia, 14 (4.03%) with acute cardiac tamponade, 8 (2.31%) with acute visceral ischemia, and 1 (0.32%) with spinal cord injury.

At the time of presentation, no difference was found in the patients' sex, BMI, LVEF, and clinical status regarding diabetes mellitus, hypertension, coronary artery disease, cerebrovascular

[1]http://www.empowerstats.com

[2]http://www.R-project.org

TABLE 1 | Baseline characteristics of patients according to D-dimer tertiles.

Characteristics	Total *n* = 347	Lowest tertile (T1) *n* = 116	Median tertile (T2) *n* = 115	Highest tertile (T3) *n* = 116	*P*-value
D-Dimer (ug/ml)	1.95 (0.77–3.16)	0.51 (0.33–0.77)	1.95 (1.26–2.28)	6.27 (3.16–13.27)	<0.001
Age, *y*	48.07 ± 10.56	46.43 ± 10.69	47.43 ± 11.39	50.34 ± 9.17	0.013
Sex (men),%	275 (79.25%)	90 (77.59%)	94 (81.74%)	91 (78.45%)	0.714
BMI (kg/m2)	26.75 ± 4.35	27.00 ± 5.04	26.85 ± 4.22	26.39 ± 3.69	0.552
Smoking history	175 (51.47%)	54 (47.79%)	66 (57.39%)	55 (49.11%)	0.290
Comorbidities					
Diabetes mellitus	13 (3.75%)	3 (2.59%)	5 (4.35%)	5 (4.31%)	0.722
Hypertension	280 (80.69%)	89 (76.72%)	94 (81.74%)	97 (83.62%)	0.388
Coronary artery disease	23 (6.63%)	6 (5.17%)	8 (6.96%)	9 (7.76%)	0.720
Acute cardiac tamponade	14 (4.03%)	3 (2.59%)	2 (1.74%)	9 (7.76%)	0.073
Cerebrovascular disease	20 (5.76%)	7 (6.03%)	7 (6.09%)	6 (5.17%)	0.959
Acute visceral ischemia	8 (2.31%)	0 (0.00%)	3 (2.61%)	5 (4.31%)	0.088
Lower-extremity ischemia	26 (7.49%)	2 (1.72%)	9 (7.83%)	15 (12.93%)	0.003
Spinal cord injury	1 (0.32%)	0 (0.00%)	1 (0.94%)	0 (0.00%)	1.000
Marfan syndrome	3 (0.86%)	2 (1.72%)	1 (0.87%)	0 (0.00%)	0.552
Chronic kidney disease	58 (16.71%)	10 (8.62%)	22 (19.13%)	26 (22.41%)	0.013
LVEF%	62.49 ± 5.43	62.06 ± 6.27	62.47 ± 5.01	62.93 ± 4.91	0.492
Severe aortic regurgitation	51 (15.32%)	22 (19.82%)	14 (12.96%)	15 (13.16%)	0.502
WBC (g/L)	11.60 ± 4.06	9.53 ± 3.63	12.07 ± 4.09	13.21 ± 3.56	<0.001
NE(*10−9/L)	9.61 ± 4.04	7.33 ± 3.68	10.10 ± 3.97	11.39 ± 3.37	<0.001
Creatinine (μmol/L)	91.79 ± 50.96	83.02 ± 45.94	96.93 ± 64.17	95.45 ± 38.75	0.074
APTT (sec)	29.68 ± 4.15	29.67 ± 4.72	29.03 ± 3.70	30.32 ± 3.90	0.064
PT (sec)	12.76 ± 2.52	12.73 ± 3.01	12.47 ± 1.33	13.08 ± 2.83	0.183
Aortic root procedure					0.200
Ascending aorta replacement	183 (52.89%)	60 (51.72%)	71 (61.74%)	52 (45.22%)	
Bentall's procedure	138 (39.88%)	47 (40.52%)	40 (34.78%)	51 (44.35%)	
Aortic root repair	23 (6.65%)	8 (6.90%)	4 (3.48%)	11 (9.57%)	
Other	2 (0.58%)	1 (0.86%)	0 (0.00%)	1 (0.87%)	
Concomitant procedures (CABG and valve surgery)	32 (9.22%)	14 (12.07%)	9 (7.83%)	9 (7.76%)	0.430
Lowest nasopharygeal temperature (.C)	24.31 ± 1.54	24.34 ± 1.38	24.40 ± 1.70	24.19 ± 1.53	0.578
Lowest bladder temperature (.C)	25.68 ± 1.67	25.59 ± 1.38	25.93 ± 1.85	25.52 ± 1.72	0.137
Times					
Cross-clamp time (min)	115.45 ± 28.84	113.55 ± 28.95	111.22 ± 25.23	121.54 ± 31.21	0.017
CPB time (min)	207.63 ± 50.61	201.17 ± 44.88	206.20 ± 45.47	215.52 ± 59.47	0.091
MHCAT (min)	27.18 ± 9.81	28.28 ± 9.61	27.12 ± 9.62	26.16 ± 10.16	0.258

The data are shown as mean ± standard deviation, median (Q1, Q3), or n (%). BMI, body mass index; LVEF, left ventricular ejection fraction; WBC, white blood cell; NE, neutrophils; APTT, activated partial thromboplastin time; PT, prothrombin time; CABG, coronary artery bypass grafting; CPB, cardiopulmonary bypass; MHCAT, Moderate hypothermia circulatory arrest time; CI, confidence interval, HR, hazard ratio.

disease, the type of aortic root procedure, and concomitant procedures. However, lower-extremity ischemia and CKD were more common among those with higher D-dimer. Further, higher white blood cell counts and longer cross-clamp times were also associated with higher D-dimer.

D-dimer Levels and 90-day Postoperative Adverse Events in Patients With Acute Type A Aortic Dissection Undergoing Arch Replacement and FET

Sixty-five (18.7%) patients developed 90-day postoperative mortality and PND, consisting of 51 (14.7%) patient deaths and 14 (4.0%) patients with PND.

The results of univariate analyses of 90-day postoperative adverse events are summarized in the **Supplementary Table**. Univariate analyses showed that age, history of coronary artery disease, history of cerebrovascular disease, cardiopulmonary bypass time, cross-clamp time, and D-dimer values were associated with a significant increase in the incidence of 90-day postoperative adverse events. We performed a multivariate Cox regression analysis to further explore D-dimer as a prognostic marker. In the multivariable analysis shown in **Table 2**, D-dimer level was the independent risk factor for 90-day postoperative adverse events in Model I (HRadj 1.26 per 10 ug/ml increase, 95% CI: 1.09–1.45; P = 0.002), after adjusting for age, sex, and BMI. This was also true in Model II (HRadj 1.19 per 10 ug/ml increase, 95% CI: 1.01–1.41; P = 0.039) after adjusting

TABLE 2 | Multivariable cox regression analyses of 90-day postoperative adverse events in patients with acute type A aortic dissection undergoing arch replacement and FET.

	Non-adjusted		Adjust I		Adjust II	
	HR 95% CI	***P*-value**	**HR 95% CI**	***P*-value**	**HR 95% CI**	***P*-value**
D-dimer ug/ml per 10 ug/ml	1.28 (1.11, 1.48)	0.001	1.26 (1.09, 1.45)	0.002	1.19 (1.01, 1.41)	0.039
D-dimer tertile						
Lowest tertile (T1)	Reference		Reference		Reference	
Median tertile (T2)	2.13 (1.03, 4.38)	0.041	2.01 (0.97, 4.17)	0.058	1.58 (0.73, 3.39)	0.242
Highest tertile (T3)	3.30 (1.66, 6.55)	0.001	3.16 (1.59, 6.29)	0.001	2.41 (1.15, 5.06)	0.019
P for trend		0.0004		0.001		0.015

CI, confidence interval, HR, hazard ratio. The median (range) D-dimer was 0.51 ug/ml (0.33–0.77 ug/m) in the lowest tertile, 1.95 ug/m (1.26–2.28 ug/m) in the median tertile, and 6.27 ug/m (3.16–13.27 ug/m) in the highest tertile. Non-adjusted model adjust for: None. Adjust I model adjust for: age, sex, and BMI. Adjust II model adjust for: age, sex, and BMI; the history of coronary artery disease and cerebrovascular disease, lower-extremity ischemia, acute visceral ischemia, chronic kidney disease; WBC; cross-clamp time, cardiopulmonary bypass time.

TABLE 3 | Effects of D-dimer on 90-day postoperative adverse events in each subgroup by multivariable Cox model.

CPB per 10 min	**No. of participants**	**HR (95% CI)**	***P*-value**	***P* for interaction**
Age tertiles (year)				0.814
≤43	106	1.14 (0.84, 2.38)	0.197	
44–52	128	1.19 (0.90, 1.58)	0.231	
≥53	113	1.25 (1.04, 1.50)	0.015	
Sex				0.831
Male	275	1.25 (1.05, 1.49)	0.011	
Female	72	1.38 (1.07, 1.79)	0.014	
BMI tertiles				0.534
≤24	104	1.76 (1.36, 2.27)	<0.0001	
24–27	117	1.12 (0.89, 1.42)	0.332	
≥27	124	1.30 (0.89, 1.88)	0.170	
Cerebrovascular disease				0.105
No	327	1.19 (0.99, 1.43)	0.064	
Yes	20	7.03 (1.10, 44.98)	0.039	
Coronary artery disease				0.885
No	324	1.26 (1.08, 1.48)	0.004	
Yes	23	1.24 (0.87, 1.76)	0.236	
Acute visceral ischemia				0.072
No	339	1.33 (1.15, 1.54)	0.0001	
Yes	8	–&	–&	
Lower-extremity ischemia				0.655
No	321	1.31 (1.12, 1.54)	0.001	
Yes	26	1.06 (0.73, 1.56)	0.750	
eGFR				0.558
<60	58	1.33 (1.08, 1.65)	0.008	
≥60	289	1.18 (0.95, 1.46)	0.139	

**Adjusted for age, sex, BMI, the history of coronary artery disease and cerebrovascular disease, lower-extremity ischemia, acute visceral ischemia, chronic kidney disease except the subgroup variable. BMI, body mass index; CABG, coronary artery bypass grafting; CI, confidence interval; HR, hazard ratio. &The model failed because of the small sample size.*

for age, sex, BMI, history of coronary artery disease, history of cerebrovascular disease, lower-extremity ischemia, acute visceral ischemia, chronic kidney disease, WBC, cross-clamp time, and cardiopulmonary bypass time. Kaplan–Meier survival analysis (**Figure 2**) showed a significant difference among patients stratified by D-dimer level tertiles; specifically, D-dimer values in the highest tertile had more 90-day postoperative adverse events compared with the median and lowest tertiles ($P = 0.0014$).

Subgroup Analysis Between D-Dimer Level and 90-day Postoperative Adverse Events in Patients With Acute Type A Aortic Dissection Undergoing Arch Replacement and FET

To evaluate the potential influence of other factors, a sub-analysis was conducted stratifying patients by age

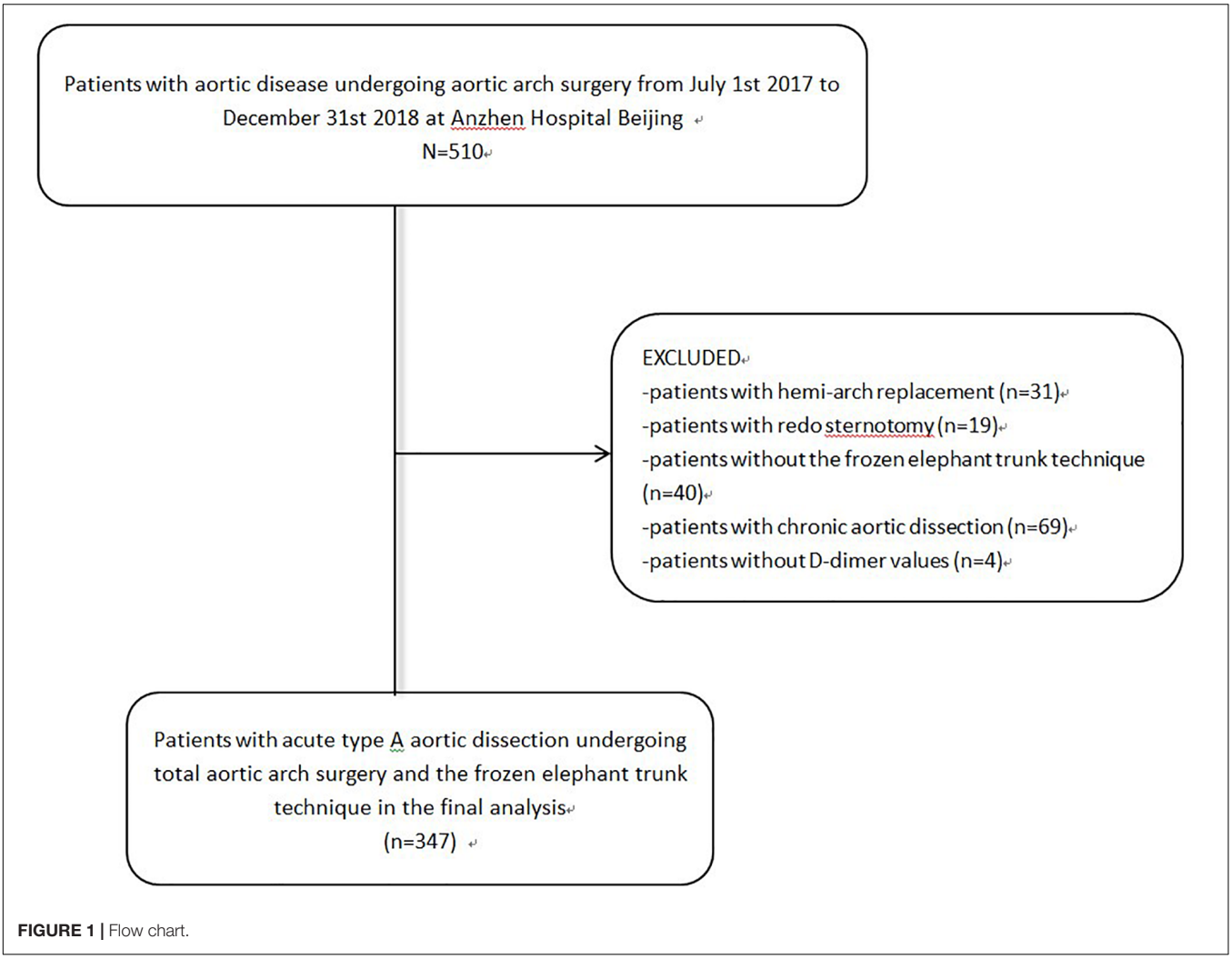

FIGURE 1 | Flow chart.

tertiles, sex, BMI tertiles, history of cerebrovascular disease, history of coronary artery disease, acute visceral ischemia, lower-extremity ischemia, and chronic kidney disease, as presented in **Table 3**. Notably, all subgroups demonstrated a similar overall relationship between D-dimer level and 90-day postoperative adverse events in patients with acute type A aortic dissection undergoing arch replacement and FET.

DISCUSSION

The results of this study show that serum D-dimer level upon admission is independently associated with 90-day postoperative adverse events in patients with acute type A aortic dissection undergoing arch surgery with FET. For every 10 ug/mL increase in plasma D-dimer concentration, the risk of 90-day postoperative adverse events increased by 19%, after adjusting for multiple factors. To the best of our knowledge, this is the first study to show an association between D-dimer level and 90-day postoperative adverse events in patients with acute type A aortic dissection undergoing arch surgery with FET.

D-dimer is a degradation product of cross-linked fibrin. Elevated D-dimer levels are generally thought to be the result of intravascular activation of the coagulation system and secondary fibrinolysis. Several studies have shown that D-dimer is a good diagnostic test for diverse thrombotic conditions, such as ischemic stroke (Nezu et al., 2018), venous thromboembolism (Faller et al., 2017), pulmonary embolism (van der Hulle et al., 2013), and aortic dissection (Mussa et al., 2016). In addition to its high diagnostic value for thrombotic disease, recent studies have also reported its relationship with short-term and long-term prognosis of these diseases (Kim et al., 2015; Vele et al., 2016; Faller et al., 2017). Additionally, several studies have shown an association in the general population (Di Castelnuovo et al., 2013). For type A aortic dissection, high levels of tissue factors are released from the aortic wall injury, after which marked coagulation activation and subsequent marked enhancement of fibrinolysis occur (Weber et al., 2003). This pathophysiological process elevates serum D-dimer levels in patients with

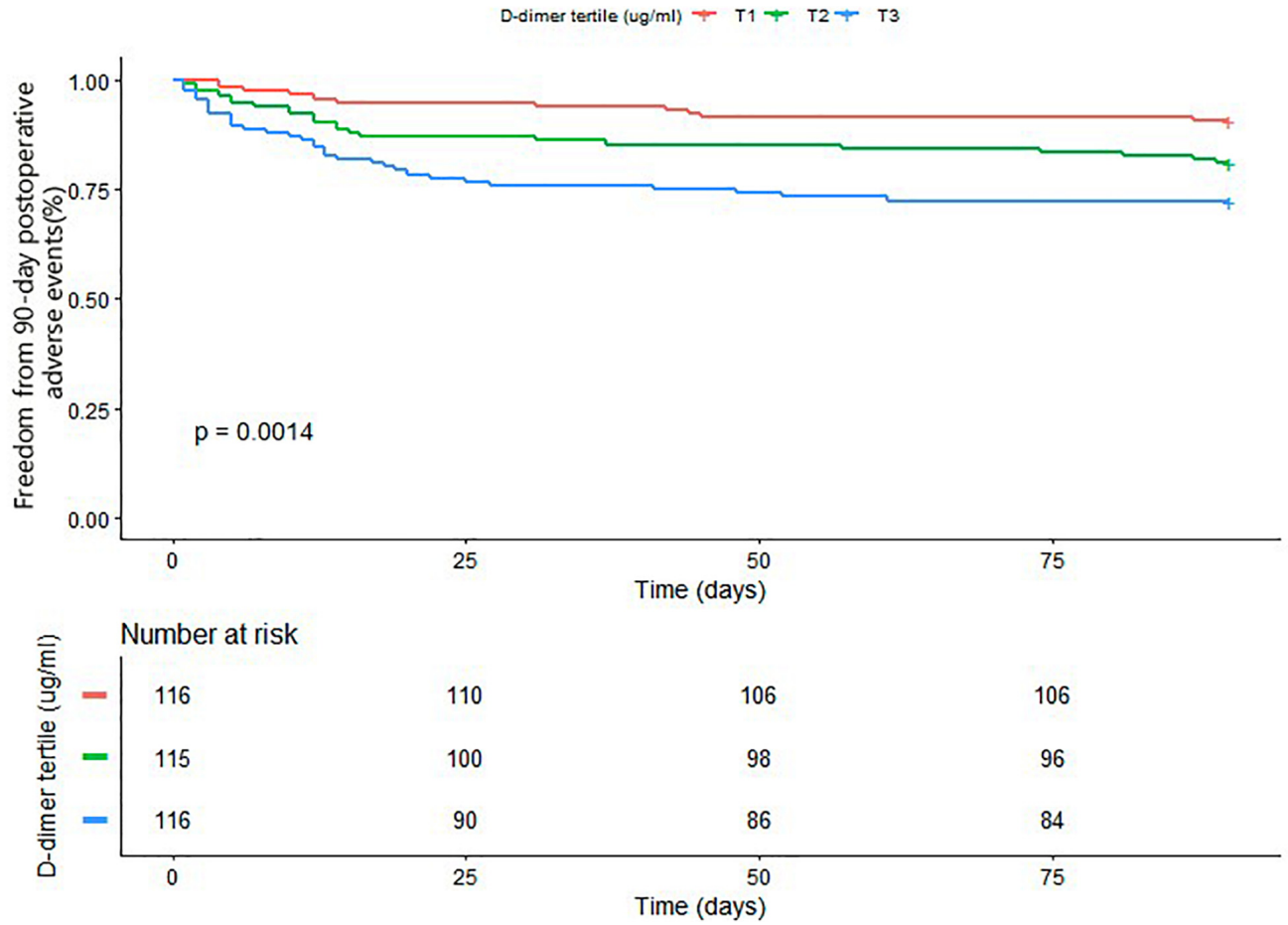

FIGURE 2 | Kaplan–Meier analysis of freedom from 90-day postoperative adverse events based on D-dimer tertile (Log-rank, $P = 0.0014$).

type A aortic dissection. The role of D-dimer in predicting short-term and long-term outcomes in patients with type A aortic dissection has been reported in previous cohort studies (Weber, 2005; Ohlmann et al., 2006; Wen et al., 2013; Huang et al., 2015). Nevertheless, these studies were made in only a limited number of patients. Further, there was significant heterogeneity in the study population, including dissection of different pathological types, as well as dissection patients treated with drugs and surgery. Additionally, for dissection patients undergoing surgery treatment, no surgical-related variables were collected. Thus, there are very few studies that focus on the relationship between D-dimer and 90-day postoperative adverse events in patients with acute type A aortic dissection undergoing arch replacement and FET.

The present study confirmed that D-dimer remains an independent predictor of 90-day postoperative adverse events in patients with type A aortic dissection despite surgical treatment. Although the mechanism of this relationship is not yet clear, some possible explanations may clarify its existence. Firstly, D-dimer concentrations may reflect the anatomical extent of the dissection, which represents the extent of the aortic injury (Weber et al., 2003; Ohlmann et al., 2006). Secondly, plasma D-dimer concentration reflects the volume of intraluminal thrombus, which is the biologically active material that takes part in the evolution of the dissection. It contains neutrophils, released pro-inflammatory cytokines, and proteolytic enzymes, which are associated with the destruction of the aortic wall and the progression of the dissection (Vele et al., 2016). Another study indicated that D-dimer values in mild to moderate traumatic brain injury predict hematoma expansion (Sugimoto et al., 2017). Finally, D-dimer also activates inflammatory cytokines and causes advanced blood coagulation or progression of dissection status. These factors might contribute to the association of high D-dimer concentrations with 90-day postoperative adverse events in patients with type A aortic disease undergoing arch replacement and FET.

In our center, over the past 10 years, although arch replacement with FET under moderate hypothermic circulatory arrest (MHAC) plus ante-grade cerebral perfusion has already become a standard procedure for aortic dissection (Sun et al., 2011; Ma et al., 2013), arch replacement is still a challenging procedure (Leontyev et al., 2016; Mussa et al., 2016). Some

previous studies analyzed pre- and intraoperative predictors of early death and PND after arch replacement (Khaladj et al., 2008; Martens et al., 2016; Liu et al., 2017). Liu et al. (2017) found that the history of cerebrovascular diseases was a strong predictor of adverse outcome following arch replacement in 626 consecutive patients in China. Khaladj et al. (2008) found that advanced age and multiple comorbidities (renal insufficiency, coronary heart disease, and reoperation) were risk factors for adverse outcomes in 501 patients undergoing aortic arch surgery. However, these studies did not collect variables of preoperative coagulation status and there was high heterogeneity of selected patients. Considering that preoperative clinical status is a strong risk factor for surgical prognosis in previous studies (Khaladj et al., 2008; Liu et al., 2017), we not only adjusted based on these potential confounding factors in multiple regression models, but we also performed subgroup analysis according to the preoperative clinical status in the current study. Our results also indicate that the relationship between D-dimer and 90-day postoperative adverse events remained unchanged (**Table 3**).

Limitations

There are several limitations in this study. First, this study is a retrospective design from a single center, and our results may not be extendable to patients in other centers. Second, we measured D-dimer only on admission, and a series of measurements after arch replacement might be more valuable for evaluation of the association between D-dimer level and 90-day postoperative adverse events. Third, for the treatment of acute type A aortic dissection, aortic arch replacement combined with FET is a preferred choice at our center, while other centers may select more conventional procedures. This might lead to differences in study results. Fourth, this study lacks data on aortic computed tomography angiography (CTA). Because our center is the largest referral center for aortic disease in China, we only referred to the images from the local hospitals, as we can't repeat the imaging examination for patients with type A aortic dissection given a limited time. Post-operative CTA was also not collected in every patient. The relationship between the level of D-dimer and CTA was not analyzed. Finally, other coagulation factors and tissue factors, such as factor II, V, VII, VIII, IX et al., were not collected because it was not the routine items of the clinical practice in the Beijing Anzhen Hospital (Capital Medical University of Beijing, China).

CONCLUSION

D-dimer is easily available in routine medical practice. Our results show that increased D-dimer levels at admission were associated with 90-day postoperative adverse events in patients with type A aortic dissection undergoing arch surgery with FET. This indicates that such high-risk patients deserve close medical monitoring.

DATA AVAILABILITY STATEMENT

The datasets generated for this study are available on request to the corresponding author.

ETHICS STATEMENT

The studies involving human participants were reviewed and approved by the Beijing Anzhen Hospital. The patients/participants provided their written informed consent to participate in this study.

AUTHOR CONTRIBUTIONS

All authors listed have made a substantial, direct and intellectual contribution to the work, and approved it for publication.

ACKNOWLEDGMENTS

We would like to thank Chen Chang-zhong MD, Ph.D. and Chen Xinlin MD, Ph.D. (Department of Epidemiology and Biostatistics, X&Y Solutions Inc., Boston, MA, United States) and for their helpful review and comments about the manuscript. We also thank the Dr. Jie Liu from the Chinese PLA General Hospital for his advice and support.

SUPPLEMENTARY MATERIAL

The Supplementary Material for this article can be found online at: https://www.frontiersin.org/articles/10.3389/fphys.2019.01627/full#supplementary-material

REFERENCES

Akutsu, K., Sato, N., Yamamoto, T., Morita, N., Takagi, H., Fujita, N., et al. (2005). A rapid bedside D-dimer assay (cardiac D-dimer) for screening of clinically suspected acute aortic dissection. *Circ. J.* 69, 397–403. doi: 10.1253/circj.69.397

Bayes-Genis, A., Mateo, J., Santaló, M., Oliver, A., Guindo, J., Badimon, L., et al. (2000). D -Dimer is an early diagnostic marker of coronary ischemia in patients with chest pain. *Am. Heart. J.* 140, 379–384. doi: 10.1067/mhj.2000.108823

Daily, P. O., Trueblood, H. W., Stinson, E. B., Wuerflein, R. D., and Shumway, N. E. (1970). Management of acute aortic dissections. *Ann. Thorac. Surg.* 3, 237–247.

Di Castelnuovo, A., de Curtis, A., Costanzo, S., Persichillo, M., Olivieri, M., Zito, F., et al. (2013). Association of D-dimer levels with all-cause mortality in a healthy adult population: findings from the MOLI-SANI study. *Haematologica* 98, 1476–1480. doi: 10.3324/haematol.2012.083410

Di Nisio, M., Squizzato, A., Rutjes, A. W., Buller, H. R., Zwinderman, A. H., and Bossuyt, P. M. (2007). Diagnostic accuracy of D-dimer test for exclusion of venous thromboembolism: a systematic review. *J. Thromb. Haemost.* 5, 296–304. doi: 10.1111/j.1538-7836.2007.02328.x

Faller, N., Limacher, A., Méan, M., Righini, M., Aschwanden, M., Beer, J. H., et al. (2017). Predictors and causes of long-term mortality in elderly patients with acute venous thromboembolism: a prospective cohort study. *Am. J. Med.* 130, 198–206. doi: 10.1016/j.amjmed.2016.09.008

Hagan, P. G., Nienaber, C. A., Isselbacher, E. M., Bruckman, D., Karavite, D. J., Russman, P. L., et al. (2000). The International Registry of Acute Aortic Dissection (IRAD): new insights into an old disease. *JAMA* 283, 897–903.

Huang, B., Yang, Y., Lu, H., Zhao, Z., Zhang, S., Hui, R., et al. (2015). Impact of d-Dimer levels on admission on inhospital and long-term outcome in patients with type A acute Aortic dissection. *Am. J. Cardiol.* 115, 1595–1600. doi: 10.1016/j.amjcard.2015.02.067

Kernan, W. N. I, Viscoli, C. M., Brass, L. M., Broderick, J. P., Brott, T., Feldmann, E., et al. (2000). Phenylpropanolamine and the risk of hemorrhagic stroke. *N. Engl. J. Med.* 343, 1826–1832.

Khaladj, N., Shrestha, M., Meck, S., Peterss, S., Kamiya, H., Kallenbach, K., et al. (2008). Hypothermic circulatory arrest with selective antegrade cerebral perfusion in ascending aortic and aortic arch surgery: a risk factor analysis for adverse outcome in 501 patients. *J. Thorac. Cardiovasc. Surg.* 135, 908–914. doi: 10.1016/j.jtcvs.2007.07.067

Kim, Y. D., Song, D., Nam, H. S., Lee, K., Yoo, J., Hong, G. R., et al. (2015). D-dimer for prediction of long-term outcome in cryptogenic stroke patients with patent foramen ovale. *Thromb. Haemost.* 114, 614–622. doi: 10.1160/TH14-12-1040

Leontyev, S., Tsagakis, K., Pacini, D., Di Bartolomeo, R., Mohr, F. W., Weiss, G., et al. (2016). Impact of clinical factors and surgical techniques on early outcome of patients treated with frozen elephant trunk technique by using EVITA open stent-graft: results of a multicentre study. *Eur. J. Cardio-Thorac.* 49, 660–666. doi: 10.1093/ejcts/ezv150

Levey, A. S., Stevens, L. A., Schmid, C. H., Zhang, Y. L., Castro, A. F., Feldman, H. I., et al. (2009). A new equation to estimate glomerular filtration rate. *Ann. Intern. Med.* 9, 604–612.

Liu, H., Chang, Q., Zhang, H., and Yu, C. (2017). Predictors of adverse outcome and transient neurological dysfunction following Aortic arch replacement in 626 consecutive patients in China. *Heart Lung Circ.* 26, 172–178. doi: 10.1016/j.hlc.2016.02.004

Ma, W., Zheng, J., Liu, Y., Zhu, J., and Sun, L. (2013). Dr. Sun's procedure for type A aortic dissection: total arch replacement using tetrafurcate graft with stented elephant trunk implantation. *AORTA* 1, 59–64. doi: 10.12945/j.aorta.2013.13.015

Martens, A., Beckmann, E., Kaufeld, T., Umminger, J., Fleissner, F., Koigeldiyev, N., et al. (2016). Total aortic arch repair: risk factor analysis and follow-up in 199 patients. *Eur. J. Cardio-Thorac.* 50, 940–948. doi: 10.1093/ejcts/ezw158

Mussa, F. F., Horton, J. D., Moridzadeh, R., Nicholson, J., Trimarchi, S., and Eagle, K. A. (2016). Acute aortic dissection and intramural Hematoma. *JAMA* 316, 754–763. doi: 10.1001/jama.2016.10026

Nezu, T., Kitano, T., Kubo, S., Uemura, J., Yamashita, S., Iwanaga, T., et al. (2018). Impact of D-dimer levels for short-term or long-term outcomes in cryptogenic stroke patients. *J. Neurol.* 265, 628–636. doi: 10.1007/s00415-018-8742-x

Ohlmann, P., Faure, A., Morel, O., Petit, H., Kabbaj, H., Meyer, N., et al. (2006). Diagnostic and prognostic value of circulating D-Dimers in patients with acute aortic dissection. *Crit. Care Med.* 34, 1358–1364. doi: 10.1097/01.ccm.0000216686.72457.ec

Shao, N., Xia, S., Wang, J., Zhou, X., Huang, Z., Zhu, W., et al. (2014). The role of D-dimers in the diagnosis of acute aortic dissection. *Mol. Biol. Rep.* 41, 6397–6403. doi: 10.1007/s11033-014-3520-z

Sugimoto, K., Suehiro, E., Shinoyama, M., Sadahiro, H., Haji, K., Fujiyama, Y., et al. (2017). D-Dimer elevation as a blood biomarker for detection of structural disorder in mild traumatic brain injury. *J. Neurotraum.* 34, 3245–3248. doi: 10.1089/neu.2017.5240

Sun, L., Qi, R., Zhu, J., Liu, Y., and Zheng, J. (2011). Total arch replacement combined with stented elephant trunk implantation. *Circulation* 123, 971–978. doi: 10.1161/CIRCULATIONAHA.110.015081

Suzuki, T., Distante, A., Zizza, A., Trimarchi, S., Villani, M., Counselman, F., et al. (2009). Diagnosis of acute aortic dissection by D-Dimer. *Circulation* 119, 2702–2707. doi: 10.1161/CIRCULATIONAHA.108.833004

Ten Cate, J. W., Timmers, H., and Becker, A. E. (1975). Coagulopathy in ruptured or dissecting aortic aneurysms. *Am. J. Med.* 59, 171–176. doi: 10.1016/0002-9343(75)90351-4

van der Hulle, T., den Exter, P. L., Erkens, P. G. M., van Es, J., Mos, I. C. M., Ten Cate, H., et al. (2013). Variable D-dimer thresholds for diagnosis of clinically suspected acute pulmonary embolism. *J. Thromb. Haemost.* 11, 1986–1992. doi: 10.1111/jth.12394

Vele, E., Kurtcehajic, A., Zerem, E., Maskovic, J., Alibegovic, E., and Hujdurovic, A. (2016). Plasma D-dimer as a predictor of the progression of abdominal aortic aneurysm. *J. Thromb. Haemost.* 11, 2298–2303. doi: 10.1111/jth.13487

Wang, Y., Tan, X., Gao, H., Yuan, H., Hu, R., Jia, L., et al. (2018). Magnitude of soluble ST2 as a novel biomarker for acute aortic dissection. *Circulation* 137, 259–269. doi: 10.1161/CIRCULATIONAHA.117.030469

Weber, T. (2005). Plasma concentrations of D-dimer predict mortality in acute type A aortic dissection. *Heart* 92, 836–837. doi: 10.1136/hrt.2005.072959

Weber, T., Gler, S. H., Auer, J., Berent, R., Lassnig, E., Kvas, E., et al. (2003). D-dimer in acute aortic dissection. *Chest* 123, 1375–1378.

Wen, D., Du, X., Dong, J., Zhou, X., and Ma, C. (2013). Value of D-dimer and C reactive protein in predicting inhospital death in acute aortic dissection. *Heart* 99, 1192–1197. doi: 10.1136/heartjnl-2013-304158

Conflict of Interest: The authors declare that the research was conducted in the absence of any commercial or financial relationships that could be construed as a potential conflict of interest.

frontiers in Physiology

ORIGINAL RESEARCH
published: 23 January 2020
doi: 10.3389/fphys.2019.01611

Topologic and Hemodynamic Characteristics of the Human Coronary Arterial Circulation

*Janina C. V. Schwarz, Monique G. J. T. B. van Lier, Jeroen P. H. M. van den Wijngaard, Maria Siebes and Ed VanBavel**

Department of Biomedical Engineering and Physics, Amsterdam UMC, University of Amsterdam, Amsterdam, Netherlands

Background: Many processes contributing to the functional and structural regulation of the coronary circulation have been identified. A proper understanding of the complex interplay of these processes requires a quantitative systems approach that includes the complexity of the coronary network. The purpose of this study was to provide a detailed quantification of the branching characteristics and local hemodynamics of the human coronary circulation.

Methods: The coronary arteries of a human heart were filled post-mortem with fluorescent replica material. The frozen heart was alternately cut and block-face imaged using a high-resolution imaging cryomicrotome. From the resulting 3D reconstruction of the left coronary circulation, topological (node and loop characteristics), topographic (diameters and length of segments), and geometric (position) properties were analyzed, along with predictions of local hemodynamics (pressure and flow).

Results: The reconstructed left coronary tree consisted of 202,184 segments with diameters ranging from 30 μm to 4 mm. Most segments were between 100 μm and 1 mm long. The median segment length was similar for diameters ranging between 75 and 200 μm. 91% of the nodes were bifurcations. These bifurcations were more symmetric and less variable in smaller vessels. Most of the pressure drop occurred in vessels between 200 μm and 1 mm in diameter. Downstream conductance variability affected neither local pressure nor median local flow and added limited extra variation of local flow. The left coronary circulation perfused 358 cm^3 of myocardium. Median perfused volume at a truncation level of 100 to 200 μm was 20 mm^3 with a median perfusion of 5.6 ml/min/g and a high local heterogeneity.

Conclusion: This study provides the branching characteristics and hemodynamic analysis of the left coronary arterial circulation of a human heart. The resulting model can be deployed for further hemodynamic studies at the whole organ and local level.

Keywords: human, coronary circulation, hemodynamics, myocardial perfusion, modeling, branching patterns, scaling laws

OPEN ACCESS

Edited by:
Kelvin Kian Loong Wong,
The University of Adelaide, Australia

Reviewed by:
Junmei Zhang,
National Heart Centre Singapore, Singapore
Stephen Michael Moore,
IBM Research, Australia

***Correspondence:**
Ed VanBavel
e.vanbavel@amsterdamumc.nl

Specialty section:
This article was submitted to Computational Physiology and Medicine, a section of the journal Frontiers in Physiology

Received: *18 July 2019*
Accepted: *23 December 2019*
Published: *23 January 2020*

Citation:
Schwarz JCV, van Lier MGJTB, van den Wijngaard JPHM, Siebes M and VanBavel E (2020) Topologic and Hemodynamic Characteristics of the Human Coronary Arterial Circulation. Front. Physiol. 10:1611. doi: 10.3389/fphys.2019.01611

INTRODUCTION

The coronary arterial circulation consists of a myriad of vessel segments, starting at the main stem and right coronary artery and repeatedly branching toward the smallest arterioles that connect to the capillary bed. This system, covering around a 500-fold range in diameters in humans, normally allows for adequate matching of local perfusion to the oxygen needs. Thus, coronary autoregulation ensures by adjusting vasomotor tone that local perfusion at rest increases with, among others, oxygen demand, and is relatively insensitive to changes in systemic pressure (Mosher et al., 1964; Goodwill et al., 2017). It is generally believed that also the coronary artery structure adapts to allow for optimal perfusion capacity, although the concepts and mechanisms here are far less clear (Seiler et al., 1992; Kassab, 2005). This system is challenged in coronary artery disease (CAD), where proximal stenoses cause flow impairment. In addition, downstream coronary arteries and arterioles may also be affected by CAD, resulting in endothelial dysfunction and, consequently, impaired regulatory capacity and reduced ability for structural adaptation.

Many processes have been identified that contribute to functional and structural regulation in the coronary circulation. For acute autoregulation, these include effects of local metabolites released from the cardiomyocytes, the myogenic response to changes in local pressure, and flow-dependent dilation (Dole, 1987). In addition, conducted vasomotor responses may further integrate the local responses (Palao et al., 2018). Structural adaption may include hypoxia-driven angiogenesis, flow-dependent remodeling, and pressure-induced changes in wall-to-lumen ratio (Hoefer et al., 2013; Silvestre et al., 2013; Zimarino et al., 2014). We also demonstrated in a range of *in vitro* and *in vivo* settings that vasomotor tone itself is a drive for structural changes in arterial caliber (Bakker et al., 2002; VanBavel et al., 2006).

It has long been realized that proper understanding of the interplay of all of these processes requires a quantitative systems approach that includes the complexity of the coronary network. Accordingly, several previous studies provided detailed descriptions of such networks, based mostly on porcine coronary arterial casts (VanBavel and Spaan, 1992; Kassab et al., 1993; Kassab and Fung, 1994; Kaimovitz et al., 2010). Yet, data on human coronary branching patterns are extremely scarce (Zamir and Chee, 1986; Zamir, 1999; van Lier et al., 2016).

The purpose of the current study therefore was to provide a detailed quantification of the branching characteristics of the human coronary circulation. These data were obtained from a human heart in which coronary arteries were filled with casting material, followed by sectioning in a 3D imaging cryomicrotome, 3D reconstruction, and *post hoc* image processing (Spaan et al., 2005). Our analysis included topological (e.g., node and loop characteristics), topographic (diameters and length of segments) and geometric (position) data along with predictions of local hemodynamics (pressure and flow). These data allow evaluation of the relevance of previous animal studies and provide a base for a systems analysis of human coronary flow regulation.

MATERIALS AND METHODS

Human Heart

The data in this study were derived from a post-mortem human heart obtained at the Department of Pathology of the Academic Medical Center, University of Amsterdam, Netherlands. Heart weight was 330 gram. The patient was an 84-year-old female suffering from amyotrophic lateral sclerosis (ALS). Cause of death was listed as euthanasia. The patient history included atrial tachycardia, mitral stenosis, abdominal aortic aneurysm, atherosclerosis, and hypertension. However, the patient had never suffered any major cardiovascular events, and the heart had a normal appearance, without evidence of contracture. The patient's relatives gave written consent to use this heart for research.

Vascular Cast and Imaging

A 3D-representation of the coronary vasculature was obtained utilizing the cryomicrotome imaging procedure described previously (Spaan et al., 2005; van Horssen et al., 2014). In brief, after removing the heart, the left circumflex, left anterior descending artery, and right coronary artery were cannulated, flushed with calcium-free buffer and thereafter filled with fluorescent vascular cast material (UV-Blue, VasQtec, Switzerland, suspended in Batson's no. 17, Polysciences, United States; infusion pressure 90 mmHg). The vascular filling protocol was optimized to fill down to arterioles of around 15 μm in diameter to avoid background fluorescence via capillary filling. After the cast material had hardened, the heart was suspended in a carboxymethylcellulose sodium solvent (Brunschwig Chemie, Netherlands) blackened with 5% Indian ink (Royal Talens, Netherlands) and frozen at −20°C. To acquire a 3D digital reproduction, the frozen sample was sectioned with a slice thickness of 30 μm, matching the in-plane image resolution. After every slice, the remaining block surface, rather than the slice itself, was imaged twice for two optical settings. This automated procedure thereby yielded two co-registered image stacks, each containing 4200 4096 × 4096 16-bit images: a stack with reflection images and a stack of fluorescent images optimized for the vascular cast (excitation, 365 nm and emission, 505 nm) (**Figure 1A**).

Vessel Segmentation and Quantification

As a next step, the topological tree was extracted from the digital reproduction of the fluorescent vascular cast. For this, dark current artifacts were eliminated and optical blurring was corrected by deconvolving the images with a system-specific point-spread function (Matlab; The MathWorks Inc., Natick, MA, United States) (Schwarz et al., 2017). Subsequently, the vessels were segmented (**Figure 1B**) in three steps. First, the major coronary arteries were manually segmented in Amira (FEI Visualization Sciences Group, France) using a fourfold down-sampled image stack. Secondly, arterioles and arteries were enhanced by multi-scale vesselness filtering. For vessels smaller than 300 μm the original resolution was used; larger vessels were enhanced at half the original resolution. Thirdly, the centerline

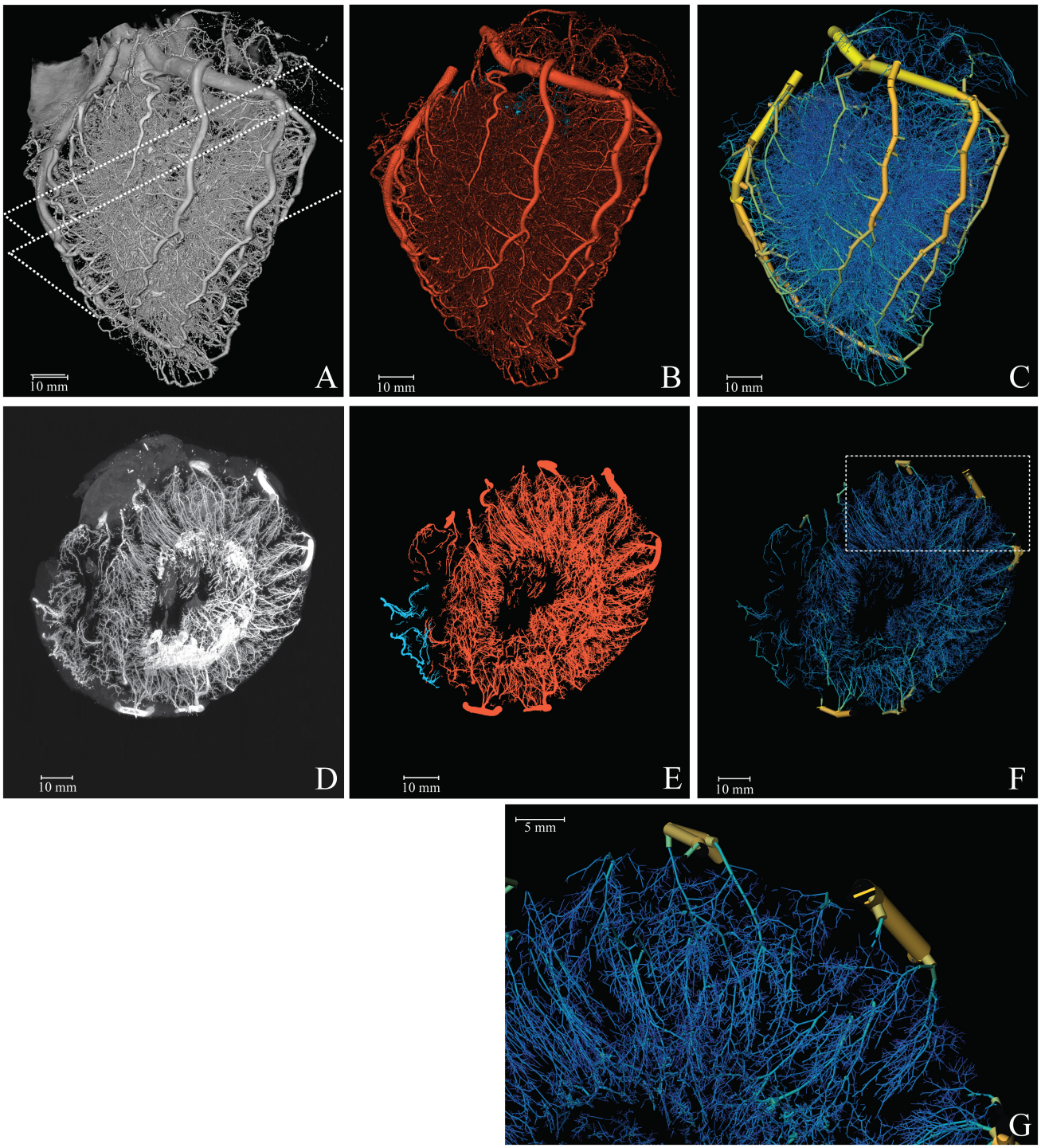

FIGURE 1 | Reconstruction of the coronary vasculature. **(A)** Raw data. Dashed lines indicate the 1 cm slab (transversal, parallel to the cutting plane) used for the MIP. **(B)** Segmented vasculature. **(C)** Reconstructed tree with color coded diameter (yellow = 4 mm, blue = 50 μm). **(D)** 1 cm MIP of raw data. **(E)** 1 cm MIP of segmented data (red, left; blue, right circulation). **(F)** 3D visualization of a 1 cm slab parallel to the cutting plane. **(G)** Magnification of the reconstructed vasculature (area indicated in **F**).

representation of the entire arterial vasculature was obtained by thresholding the result of the second step and subsequent merging with the skeleton of the manually segmented large vessels from step 1. The resulting image stack was up-sampled to full resolution, after which the centerlines were obtained by 3D-skeletonization (Lee et al., 1994). We visually inspected

the results and compared these with the original image data. Obvious artifacts resulting from cast interruption or cutting debris were corrected.

Every point on a centerline was classified according to the number of neighboring points. Points with a single neighbor were classified as terminal node. Points with two neighbors were considered to be mid-segmental points. Points with three or more neighbors in the skeleton reflected internal nodes connecting multiple segments.

The diameter at each point was estimated using a full width at half maximum algorithm on the normal plane. Segments were defined as the centerline path between two nodes. Internal segments connect two internal nodes, while terminal segments connect an internal and terminal node. Segment diameters were determined as the mean of the diameters of the segment's mid-segment points. Spurious terminal segments and triangular loops were eliminated based on quality measures for the diameter, including the condition that the segment length should be larger than the segment diameter. Diameters of internal segments that were underestimated, e.g., due to cast artifacts, were corrected by interpolation from diameters of neighboring segments. The results were stored in graph notation, a means to study relations and processes in networks, representing the vasculature as a set of nodes and cylindrical segments with associated information on its characteristics and its neighboring nodes and segments. For every node, the proximity to its coronary root was calculated. Segment description included their path length, mean diameter, as well as myocardial region (**Figure 1C**).

In order to study vessel branching, bifurcations were identified. For every bifurcation, the three connected segments were classified into mother and daughter segments based on flow direction.

The symmetry (S) of the daughters was defined as the ratio of the smaller (d_S) to the larger (d_L) diameter.

$$S = d_S/d_L \tag{1}$$

As a second parameter, the relation between mother (M) and her daughters was represented by the increase in total cross-sectional area:

$$A = \frac{d_L^2 + d_S^2}{d_M^2} \tag{2}$$

For analysis, segments, and bifurcations were grouped into ten classes based on (mother) diameter (d_M).

Extension of the Measured Tree Toward the Terminal Microcirculation

The extracted coronary vascular network terminates at 30 μm segments, since this was the resolution of the imaging technique, or at larger diameters where cast material had insufficiently filled the arterial bed. In order to estimate hemodynamic properties of the human coronary circulation, extrapolation toward the terminal arterioles is required. Notably, distributions of downstream conductances distal to the extracted end segments are needed. These were obtained by simulating segments smaller than 30 μm based on interpolation and extrapolation of the extracted vascular network. These *in silico* trees were generated as follows. Starting with an initial segment with a diameter between 300 and 400 μm, two daughter segments were created with symmetry stochastically drawn from the symmetry distribution observed in this human heart coronary network for segments of the same diameter class. Their diameters were set to match the area growth for their symmetry and mother diameter as expected from the data. Segment lengths were randomly assigned based on the segment-length-to-diameter distribution of their diameter class. For diameters below 30 μm, extrapolated branching characteristics were used. This procedure was iterated until the capillary domain (5.0–7.5 μm) was reached. For every segment, the total conductance of its distal network was calculated. Fifty trees in total were generated for this purpose, resulting in a distribution of downstream conductances for segments in the range between 30 μm and 400 μm. These predictions were then imputed to the recorded tree. Finally, hemodynamics in the extracted coronary tree was determined for 1000 simulations of the stochastic terminal conductances.

Computational Hemodynamic Modeling

Blood was modeled as an incompressible, isotropic homogeneous fluid. To account for the Fåhraeus-Lindqvist effect, an empirical diameter-dependent relationship derived by Pries et al. was used to model blood viscosity (μ), assuming a constant hematocrit $H_d = 0.4$ (Pries et al., 1994; Secomb and Pries, 2013):

$$\mu = \left[1 + \left(\mu^*_{0.45} - 1\right)\frac{(1-H_d)^C - 1}{(1-0.45)^C - 1}\left(\frac{d}{d-1.1}\right)^2\right] \times \left(\frac{d}{d-1.1}\right)^2 \tag{3}$$

with

$$\mu^*_{0.45} = 6e^{-0.085d} + 3.2 - 2.44\mathrm{e}^{-0.06\mathrm{d}^{0.645}}$$

$$C = \left(0.8 + \mathrm{e}^{-0.075\mathrm{d}}\right)\left(-1 + \frac{1}{1 + 10^{-11}d^{12}}\right) + \frac{1}{1 + 10^{-11}d^{12}}$$

The fully developed, laminar axisymmetric steady-state flow through a segment was modeled based on Poiseuille's law including the above Fåhraeus-Lindqvist effect. For a segment with nodes i and j, the flow ($Q_{i\to j}$) through and the conductance (G_{ij}) of the segment are:

$$Q_{i\to j} = G_{ij}(P_i - P_j) \tag{4}$$

$$G_{ij} = \frac{\pi d_{ij}^4}{128\mu_{ij}l_{ij}} \tag{5}$$

where P_i is the pressure at node i, μ_{ij} is the blood viscosity, d_{ij} is the diameter and l_{ij} the length of the segment between nodes i and j. Applying Kirchhoff's current law, i.e., conservation of mass at every junction, $\sum_{i\in N_j} Q_{i\to j} = 0$, where N_j is the set of neighbor nodes, yields a system of linear equations that can be solved via matrix inversion for a given set of flow or pressure boundary conditions. We used a coronary inlet pressure

of 90 mmHg and capillary pressure of 20 mmHg. Wall shear stress was estimated under the premise of non-accelerating flow such that the frictional forces with the wall balance the force from the pressure gradient in every segment (Munson et al., 2013).

$$\tau_{ij} = \frac{\left(P_i - P_j\right) d_{ij}}{4 l_{ij}} \quad (6)$$

Perfusion was derived by relating the flow through 100–200 μm segments to the weight of their perfusion territory. The perfusion territories were determined in 3D by Voronoi tessellation. Voxels within the heart belong to the Voronoi cell of the closest terminal node. The union of all Voronoi cells perfused by a single 100–200 μm segment was taken as its perfusion territory.

Statistical Analysis

The difference between two daughter symmetry classes was tested using a Mann Whitney *U*-test. Differences between multiple diameter classes and myocardial regions were tested using a one-way Kruskal-Wallis analysis followed by a Dunn's multiple comparison test. A two-way ANOVA followed by Bonferroni's correction for multiple comparisons was employed to assess differences in area growth. Statistical analyses were performed using GraphPad Prism (GraphPad Software, Inc., La Jolla, CA, United States). Least-squares regression in Matlab was used for testing the agreement between hemodynamic results, for analyzing the relation between diameter, symmetry, and area growth (linear fit) and for determining the power laws (non-linear fit). A $p < 0.05$ was considered statistically significant.

RESULTS

Coronary Arterial Topology

Figure 1A provides a 3D visualization of the coronary arterial cast (raw data), as acquired with the imaging cryomicrotome, while **Figures 1B,C** show the results of the segmentation in single color and diameter-encoded color, respectively. **Figures 1D–G** provide maximum intensity projections of a transversal section and a magnification. Visual inspection of the raw data revealed nearly complete filling of the arterial tree down to 30 μm, covering the expected perfusion territory. Vascular density appeared highest in the subendocardium and lowest in the subepicardium. While **Figure 1** depicts both the left and right coronary circulation, the remainder of the study focused on the left coronary circulation.

The reconstructed left coronary tree consisted of 202,184 segments with diameters ranging from 30 μm in small arterioles to 4 mm for the epicardial arteries. **Table 1** gives an overview of distribution of these segments over diameter classes and myocardial regions. Taking the class sizes into account, the data show increased density of smaller segments, as expected, which levels off below 60 μm diameter. We attribute this to incomplete filling of vessels smaller than 60 μm. Terminal segment density increased strongly from subepicardium to subendocardium, in accordance with visual inspection of the transversal sections of **Figure 1**. The distributions of terminal segment diameters in the three myocardial regions were very comparable, indicating that the increased subendocardial density is not a result of better filling of the distal vessels in this region.

The reconstructed coronary network was not a simple tree with only bifurcations. Rather, 91% of the nodes were bifurcations, 8% were trifurcations (connecting four segments) and less than 1% connected more than four segments. The network also contained arcades or loops: an analysis based on graph theory revealed 3,202 such loops.

As shown in **Figure 2A**, segment length exhibited a large range, from 60 μm for distal vessels to around 2 mm for the main coronaries, with a strongly skewed distribution. Most segments were between 100 μm and 1 mm long. While the segments with smallest diameter were also the shortest, median segment length was remarkably similar in the diameter range between 75 and 200 μm (**Figure 2B**). Subepicardial terminal segments were longer than midmyocardial and subendocardial ones (**Table 1**, $p < 0.001$).

Figure 3A depicts the symmetry of the bifurcations, reflected by the ratio of daughter segment diameters, in the various mother diameter classes. Very asymmetric branches generally reflected consecutive segments of large vessels having small side branches. Here, d_L is expected to be close to d_M and indeed, the d_L/d_M-ratio was significantly larger for such asymmetric nodes ($p < 0.001$). For all diameter classes, in particular for segments larger than 150 μm, node symmetry was highly variable. With decreasing diameter, the nodes became more symmetric, and the dispersion in symmetry decreased slightly, as illustrated by the histograms in **Figures 3B,C**.

The area growth at bifurcations was also highly variable. For segments larger than 400 μm, on average the cross-sectional area remained stable (median area growth: 1.02). For most other bifurcations, the total cross-sectional area of the daughters was larger than the cross-sectional area of their mother segment. Linear regression showed that area growth (A) increased with decreasing mother diameter (d_M) and increasing symmetry (S): ($A = -0.66\, d_M + 0.34\, S + 1.13,\ d_M \in [75, 600]\ 10^{-6} m$). Even though all coefficients in the fit were highly significant ($p < 0.001$), the low $r^2 = 0.047$ indicates that mother diameter and daughter asymmetry account only little (4.7%) for the encountered variability. **Figure 4** shows this relationship, where the data are grouped in order to comprehensively visualize the effect of both mother diameter as well as symmetry.

Prediction of Distal Arterial Conductance

The fifty *in silico* trees, generated from the above described relationships for segment length, daughter symmetry and area growth, on average consisted of 1.22 ± 0.05 million segments. For all trees, there was a linear relation between the log-transformed segment diameter and distal arterial conductance. As the linear regressions were very similar for all trees (coefficient of variation for both coefficients below 0.5%), all *in silico* data were pooled (**Figure 5A**, turquoise area). For the smallest segments with diameter less than 12 μm, the distal arterial conductance was more variable than for larger segments. Moreover, distal conductance became less dependent on diameter. The increase in distal arterial

TABLE 1 | Segment distribution.

	Number of segments (n, %)		LV density of terminal segments (n/cm^3, %)		
Diameter class	**All**	**Terminal**	**Subepicardium**	**Midmyocardium**	**Subendocardium**
30–45 μm	8,047 (4.0)	6,695 (6.6)	12.2 (7.2)	20.9 (5.8)	34.9 (7.3)
45–60 μm	22,204 (11.0)	20,760 (20.6)	37.4 (22.2)	65.5 (18.3)	104.2 (21.9)
60–75 μm	32,500 (16.1)	27,545 (27.3)	46.2 (27.4)	90.3 (25.2)	136.3 (28.6)
75–90 μm	33,605 (16.6)	22,872 (22.7)	38.0 (22.6)	83.0 (23.2)	106.8 (22.4)
90–105 μm	27,816 (13.8)	12,860 (12.7)	21.9 (13.0)	52.0 (14.5)	50.2 (10.5)
105–120 μm	19,444 (9.6)	5,428 (5.4)	7.9 (4.7)	23.9 (6.7)	21.6 (4.5)
120–150 μm	24,598 (12.2)	3,274 (3.2)	3.4 (2.0)	15.3 (4.3)	14.8 (3.1)
150–200 μm	19,718 (9.8)	1,204 (1.2)	1.1 (0.7)	5.5 (1.5)	6.2 (1.3)
200–400 μm	12,665 (6.3)	321 (0.3)	0.3 (0.2)	1.5 (0.4)	1.6 (0.3)
≥400 μm	1,587 (0.8)	2 (0.0)	0.0 (0.0)	0.0 (0.0)	0.0 (0.0)
Total	202,184 (100.0)	100,961 (100.0)	168.4 (100.0)	357.8 (100.0)	476.6 (100.0)
Diameter. median (μm)	92.3	72.4	71.2	75.4	70.6
Diameter. interdecile range (μm)	54.3–179	47.8–105	47.4–101	48.9–110	46.7–103
Length. median (μm)	441	443	473	453	391

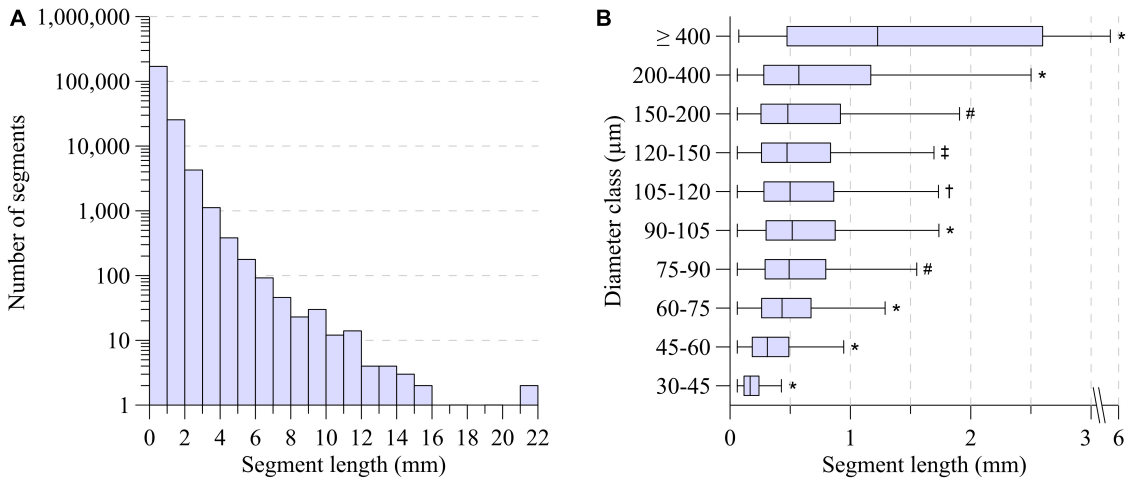

FIGURE 2 | (A) Segment length distribution. **(B)** Segment length-diameter relation for ten diameter classes. Boxplot indicates median (black line); the bottom and top edges of the box indicate the 25th and 75th percentiles. Whiskers indicate 1.5 IQR. Outliers are not shown. *Significant different from all ($P < 0.001$). #Significant different from 30 to 45, 45 to 60, 60 to 75, 90 to 105, 200 to 400, ≥400 ($P < 0.001$). †Significant different from 30 to 45, 45 to 60, 60 to 75, 90 to 105, 120 to 150, 200 to 400, ≥400 ($P < 0.001$). ‡Significant different from 30 to 45, 45 to 60, 60 to 75, 90 to 105, 105 to 120, 200 to 400, ≥400 ($P < 0.001$).

conductance (in m^3/(Pa · s)) for larger vessels was well predicted by the allometric relation $G_{is} = 1.64 \cdot 10^{-3}\, d^{2.49}$ (d in m; $r^2 = 0.98$, $p < 0.001$).

Pressure and Flow Distributions

Hemodynamics in the reconstructed arterial network with stochastically extended downstream conductances were determined in 1,000 simulations of this whole network. **Supplementary Figure 1** provides a 3D rendering of the median parameter values derived from the hemodynamic simulations across the segmented vascular segments.

The coefficient of variation of the conductance downstream of a specific end segment over these simulations was 0.11 (median over all end segments). We questioned to what extent this variation in chosen downstream conductances affects the calculated pressure and flow in the complete left coronary network. **Table 2** summarizes this analysis. In the stochastic model, pressure in individual segments varied marginally between the simulations, whereas the median coefficient of variation for flow was 7.4%. Hemodynamic simulations with deterministically assigned distal arterial conductances yielded flow and pressure values that fully agreed with the median values of all stochastic simulations. This was the case for two choices for downstream conductance in each measured end segment: based on the power fit above or based on the median value of downstream conductance for similar-sized segments (diameter within 2.5%) in the *in silico* data. This analysis thus reveals that downstream conductance variability affects neither local pressure or its variability, nor median local flow, and adds limited extra variation of local flow in the various diameter classes. For these

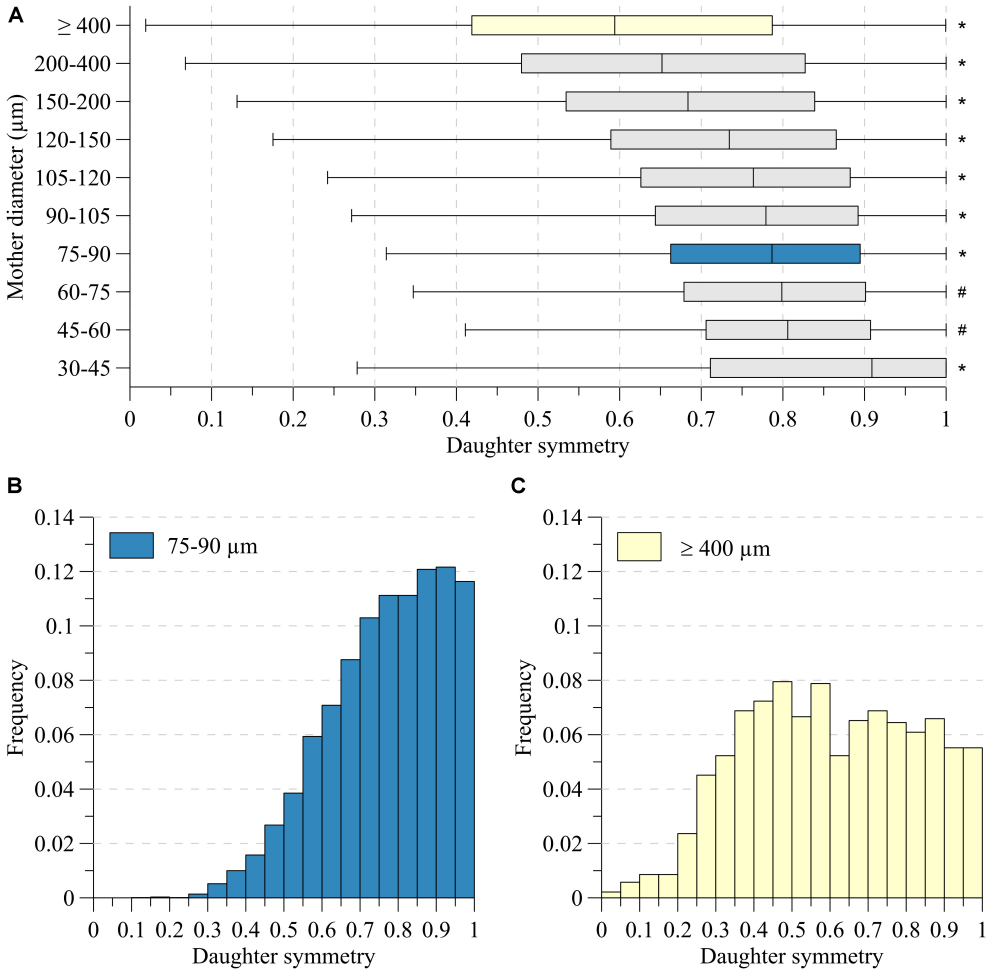

FIGURE 3 | Daughter symmetry for **(A)** ten mother diameter classes. **(B)** Distributions for mother diameter 75–90 µm (blue) and **(C)** ≥400 µm (yellow). *Significant different from all ($P < 0.05$). #Significant different from 30 to 45, 75 to 90, 90 to 105, 105 to 120, 120 to 150, 150 to 200, 200 to 400, ≥400 ($P < 0.05$).

reasons, further analysis was based on the deterministic model for distal conductance, using the median values in the 2.5% diameter intervals.

The brown line in **Figure 5A** represents the median distal arterial conductance for the reconstructed human left coronary tree with extrapolated microcirculation. This line closely matches the *in silico* results by design for small diameters, mostly reflecting terminal segments, yet also agrees well for larger segments [$G = 1.58 \cdot 10^{-4}\, d^{-2.22}$, d in m, G in $m^3/(Pa \cdot s)$], $r^2 = 0.81$; for internal segments the exponent was: 2.18).

Figure 5B shows the pressure as a function of segment diameter. Most of the pressure drop occurred in vessels between 200 µm and 1 mm in diameter whereas only little pressure drop was seen in larger arteries. Despite this trend, the pressure differed greatly between segments of similar diameter. The pressure-diameter relation was $P = 5.40 \cdot 10^3\, d^{0.60}$ ($d \in [250,\ 800]\ 10^{-6}$ m, P in mmHg, $r^2 = 0.14$).

Blood flow varied with diameter by about a fivefold interquartile range as indicated by the brown area in **Figure 5C**. Arteries larger than 1 mm carried a median of 36.6 ml/min, about 3,000-times as much blood per vessel as 100 µm segments. An allometric fit of flow ($Q = a\, d^{\gamma}$) over the whole diameter range predicts an exponent γ of 2.53 ($Q = 5.07 \cdot 10^8\, d^{2.53}$, d in m, Q in ml/min, $r^2 = 0.83$).

As shown in **Figure 5D**, centerline velocity followed the same trend as blood flow and increased with increasing diameter. The diameter velocity relation was; $v = 3.00 \cdot 10^4\, d^{0.89}$ (d in m, v in cm/s, $r^2 = 0.21$). Centerline velocity along the epicardial arteries decreased with branching.

The brown area in **Figure 5E** visualizes the high variability of wall shear stress, particularly for segments between 100 µm and 1 mm. For larger segments, the variation decreased. For segments smaller than 300 µm, median wall shear stress leveled off around 5 Pa.

Local Myocardial Perfusion

The left coronary circulation perfused in total 358 cm^3 of myocardium. Truncating the measured tree in the range of 100–200 µm resulted in 4,954 segments perfusing as many territories. The median perfused volume of these truncated segments was

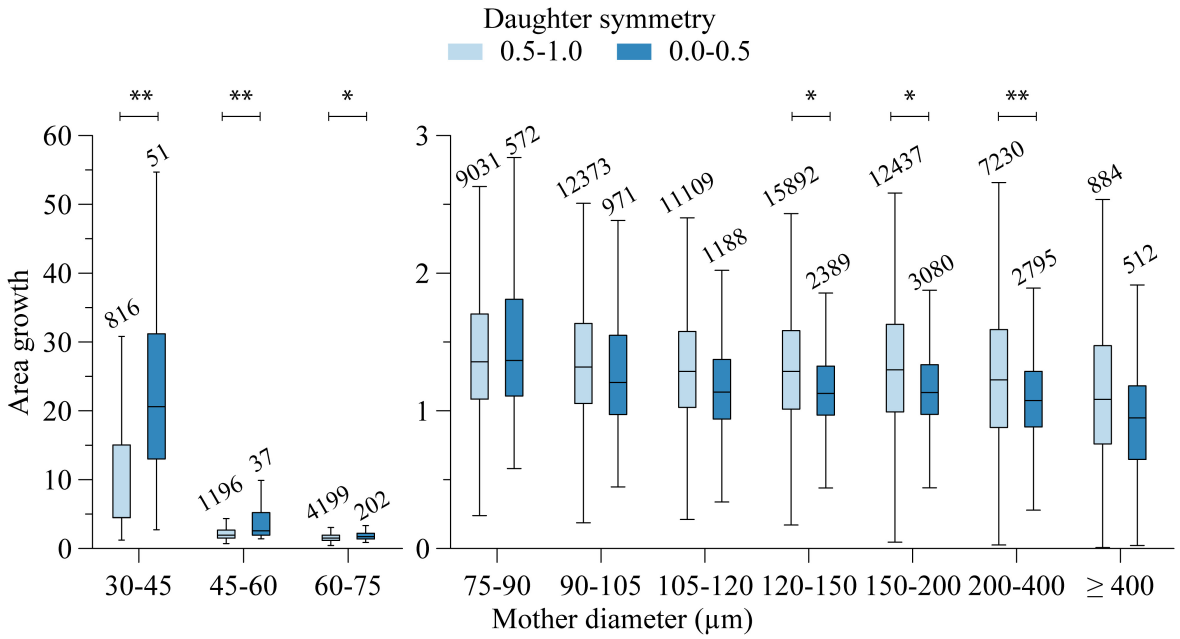

FIGURE 4 | Area growth and mother diameter relation. Per mother diameter class, data are grouped in two daughter symmetry classes. Numbers above the bars indicate group size. Significant difference: $^{**}P < 0.001$, $^{*}P < 0.01$.

20.2 mm^3 (interquartile range: 7.2–56.5 mm^3) with a median perfusion of 5.6 ml/min/g (flow per weight of the perfusion territory), yet with high local heterogeneity (interquartile range: 2.6–10.8 ml/min/g, **Figure 6**). Despite the higher vascular density, subendocardial perfusion in the left ventricle free wall was lower than midmyocardial and subepicardial perfusion. Septal perfusion from the left coronaries tended to drop from the left toward the right ventricular layer.

DISCUSSION

In this study, we extensively quantified the branching characteristics of the human coronary circulation, and used these data to predict local hemodynamics, including pressure, flow and wall shear stress, and their variation along the vascular network. These data add to previous work on various animal species and provide a base for a systems analysis of human coronary flow distribution and regulation.

Previous Data

To the best of our knowledge, no extensive studies have been made on branching patterns and related hemodynamics in the human coronary circulation. Available anatomical studies address specific research questions and provide only limited data that do not allow a translation toward global coronary hemodynamics. This includes the vascularization of the anterior papillary muscle, perfused by the LCA versus RCA (Zajaczkowski et al., 2018), the impact of branching on wave propagation (Rivolo et al., 2016), the effect of side branches on coronary flow (Wiwatanapataphee et al., 2012), and branching patterns of only the large coronary arteries (Hutchins et al., 1976; Seiler et al., 1992; van der Waal et al., 2009; Schoenenberger et al., 2012; Cardenes et al., 2013; Gupta et al., 2013; Medrano-Gracia et al., 2017; Ormiston et al., 2018). In an initial study, we analyzed the presence of collateral connections within and between the perfusion territories in the human heart (van Lier et al., 2016).

While human data are rare, several animal studies do provide quantitative data on coronary artery and microvascular branching patterns. Thus, VanBavel and Spaan analyzed the branching patterns in corrosion casts of porcine hearts, covering the major arteries down to precapillary arterioles (VanBavel and Spaan, 1992). In that work, "branching rules" were derived that relate diameter and length of individual segments, as well as the diameters of mother and daughter segments in nodes. A combination of actual data for the larger vessels and computer-generated distal branches was then used for the assessment of local pressures, flows and their dispersion. A shortcoming in that work was the limitation to topology, ignoring the 3D distribution over the myocardium. More extensive work came from the group of Kassab, who in a series of studies described these characteristics in the arterial, capillary, and venous coronary bed of pigs, also based on corrosion casts, followed by extensive modeling and hemodynamic analyses (Kassab et al., 1993, 1999; Kassab and Fung, 1994; Kalsho and Kassab, 2004; Kassab, 2005; Mittal et al., 2005a,b; Kaimovitz et al., 2008; Namani et al., 2018). Following initial work on manual segmentation of the coronary vasculature based on corrosion casts, our lab has developed an imaging cryomicrotome that allows for extensive 3D recording of branching structures (Spaan et al., 2005) and applied this technique for the

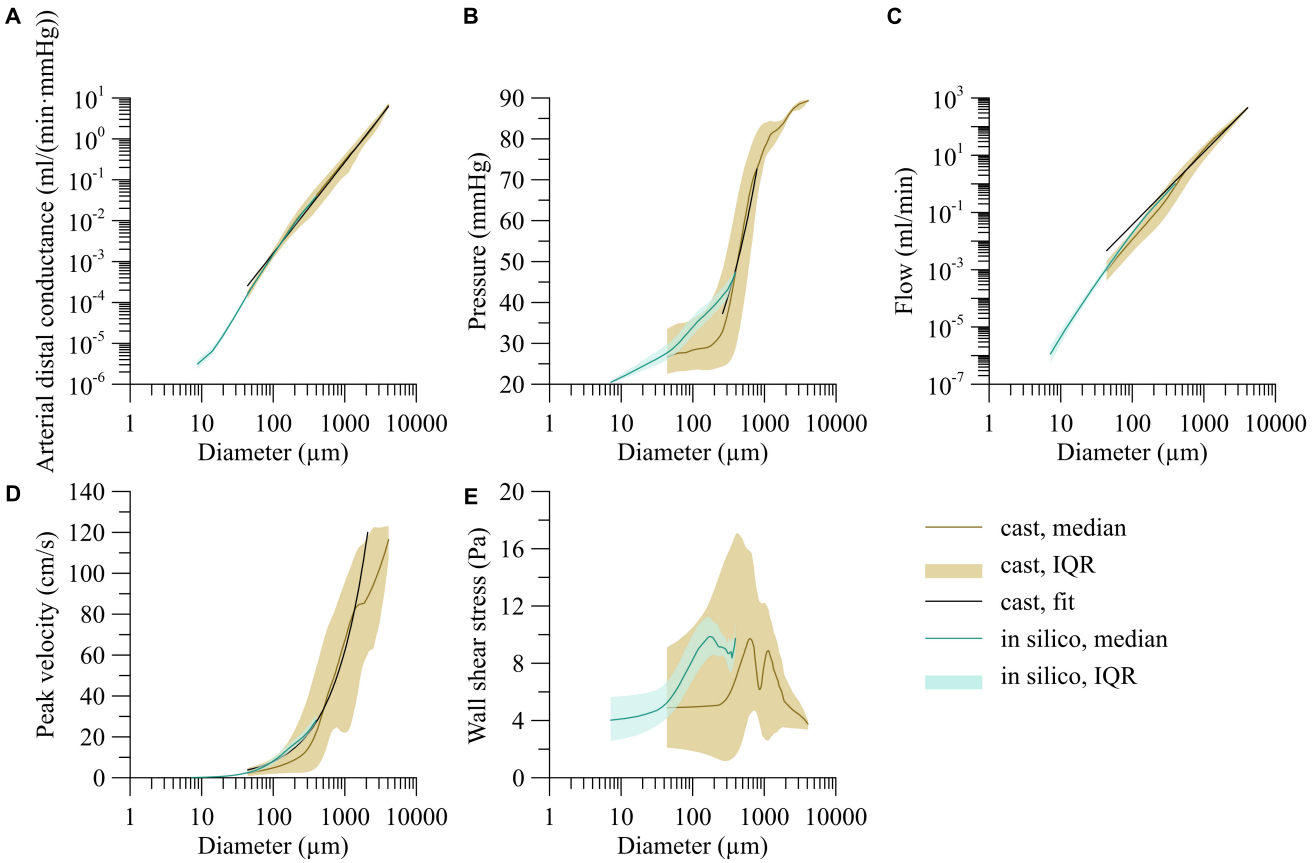

FIGURE 5 | Dependency of hemodynamic parameters on segment diameter for the trees stochastically generated based on the branching characteristics of the human vasculature (*in silico*) and the reconstructed human coronary circulation with extrapolated microcirculation (heart). **(A)** Arterial distal conductance-diameter relation, **(B)** pressure-diameter relation, **(C)** flow-diameter relation, and **(D)** centerline velocity-diameter relation. **(E)** Wall shear stress-diameter relation. Lines indicate the median; areas indicate the interquartile range.

study of network characteristics in several species and organs (van Horssen et al., 2010, 2014, 2016; van den Wijngaard et al., 2011; Hakimzadeh et al., 2014; Bedussi et al., 2015; Schwarz et al., 2017), culminating in the current work on the human heart.

Topology

The branching characteristics were described in terms of segmental diameter-length relations in addition to symmetry and area growth at branch points, as was previously done in porcine hearts (VanBavel and Spaan, 1992). Segmental length was intrinsically variable, reflecting the stochastic nature of the network. There was no clear correlation between segment length and diameter as already has been previously noted for the human right coronary artery (Zamir, 1999). Our previous porcine data predict a mean length of 275 and 619 μm in, respectively, the 90–105 and 200–400 μm diameter class, as compared to the currently observed mean values of 675 and 908 μm. However, in the same animal model Kassab et al. (1993) observed values that are closer to our findings in the current study. The differences between the porcine data may be explained by differences in filling by the casting material. Since very asymmetric nodes occur regularly, the exclusion of very small unfilled side branches would affect a substantial part of the diameter-length relation. Also symmetry was intrinsically variable. Yet, branching was more symmetric and very asymmetric nodes occurred far less in the current human heart as compared to porcine hearts. For example, for large mother diameters (>500 μm) the median observed symmetry ratio was 0.59, in contrast to values below 0.40 for porcine data (VanBavel and Spaan, 1992; Kalsho and Kassab, 2004; Rivolo et al., 2016). Despite the same trend of increasing symmetry with decreasing diameter, this difference was found for all diameter classes, and at least for the larger diameter classes this cannot be attributed to the 30 μm resolution in the current study.

The absence of growth of cross-sectional area in the largest diameter class (mother diameter ≥400 μm) is in accordance with previous observations on human (Zamir, 1999) and porcine data (VanBavel and Spaan, 1992; Kaimovitz et al., 2008), as well as observations from angiographic imaging of the epicardial arteries (Hutchins et al., 1976; Seiler et al., 1992; Schoenenberger et al., 2012; Ormiston et al., 2018). Nodes originating from smaller vessels did show growth of cross-sectional area, implying a decreasing flow velocity toward the microcirculation, as was to

TABLE 2 | Stochastic variation.

	Variability				Agreement with median			
	CV		MAD		Power fit		Median G	
	Median	P95	Median	P95	PCC	β	PCC	β
Pressure	0.004	0.011	0.10 mmHg	0.36 mmHg	1.000	0.997	1.000	1.000
Flow	0.074	0.104	<0.001 ml/min	<0.01 ml/min	1.000	1.008	1.000	0.999
Wall shear stress	0.074	0.104	0.21 Pa	1.13 Pa	0.999	0.994	1.000	1.000

Variability of outcome over the 1000 simulations (Variability) and agreement with deterministic models (Agreement with median). CV, coefficient of variation over the 1000 simulations; MAD, mean absolute deviation over the 1000 simulations; P95, 95-percentile; power fit: comparison to a deterministic model based on a power fit of distal conductance on end segment diameter. Median G, comparison to a deterministic model taking the median distal conductances in 2.5% diameter classes; PCC, Pearson's correlation coefficient; β, unstandardized coefficient.

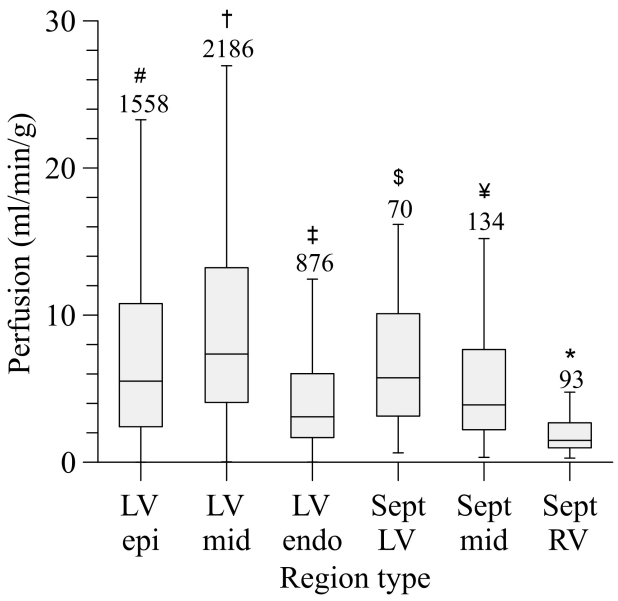

FIGURE 6 | Perfusion distribution per myocardial region. LV, left ventricular free wall; RV, right ventricular free wall; Sept, septum; epi, subepicardium; mid, midmyocardium; endo, subendocardium. Outliers are not shown. Numbers above the bars indicate group size. *Sept RV, significant different from all ($P < 0.001$); #LV epi, significant different from LV mid; LV endo, Sept RV ($P < 0.001$). †LV mid, significant different from LV epi; LV endo, Sept mid; Sept RV ($P < 0.001$). ‡LV endo, significant different from LV epi, LV mid, Sept RV ($P < 0.001$), and Sept LV ($P < 0.01$); $Sept LV, significant different from Sept RV ($P < 0.001$) and LV endo ($P < 0.01$). ¥Sept mid, significant different from LV mid, Sept RV ($P < 0.001$).

be expected. If the diameters of a node would adhere to a scaling law (Eq. 6), area growth (A) at that node would be directly related to the daughter symmetry S by:

$$d_M^\gamma = d_L^\gamma + d_S^\gamma \tag{7}$$

$$A = \frac{1 + S^2}{(1 + S^\gamma)^{2/\gamma}} \tag{8}$$

Implying that growth in cross-sectional area increases with increasing daughter symmetry for $\gamma > 2$ ($\frac{\partial A}{\partial S} = f(S, \gamma)\ \left(S^2 - S^\gamma\right)$, $f(S, \gamma) > 0, S \leq 1$). In our study, symmetric bifurcations indeed tended to show a larger area growth than asymmetric nodes, agreeing with previous observations in the human (Zamir and Chee, 1986) and in the porcine heart (Rivolo et al., 2016). A comparison with prior findings reveals that area growth tends to be higher in the present human heart as compared with similar sized arteries in the porcine hearts (VanBavel and Spaan, 1992), rat and human hearts (Zamir and Chee, 1986), while the variability in area growth was less in the human hearts. Area growth, however, tended to be smaller in the human heart in comparison to values observed in the human cerebral vasculature (Cassot et al., 2010) and in mice hearts (Feng et al., 2018) while following the same general trend of increasing area growth for smaller segments. Estimates of area growth are intrinsically sensitive to precision of diameter measurements, with random errors causing a strong upward bias in the estimate. This holds even more strongly for misclassification of mother versus daughter segments in nodes, and such bias may underlie the high growth in the smallest diameter classes.

Hemodynamic Predictions

We initially aimed to derive hemodynamic parameters throughout the network by solving the Poiseuille and Kirchhoff equations with assumptions on distal boundary conditions, such as diameter-defined flow or back pressure. Such attempts resulted in highly variable estimates for local pressure and flow that were at variance with the assumed boundary conditions. A better strategy therefore was to assume a diameter-dependent downstream conductance for each outflow segment in the casted vasculature. The generation of this relation by constructing and imputing simulated networks, based on observed and extrapolated branching characteristics and taking variability into account, allowed the hemodynamic analysis of the full, hybrid network.

A comparison of the recorded and imputed part of these networks (brown and blue lines and areas in **Figure 5**) reveals that the imputed data demonstrated less variability. We conclude from this that we did not fully cover the properties of the recorded data. Aspects that were not included in the simulated parts of the network include arcading segments, trifurcations, and possible deeper correlations in the data, such as correlations between area growth in successive nodes. Such deeper correlations are difficult to discern and quantitate, and we do not expect that

including them would strongly affect the predictions of the hemodynamic profiles.

It is now commonly accepted that the major part of the pressure drop occurs over the arterial system, with substantial contribution of arterioles and small arteries. Direct recordings of this pressure distribution are very limited and do not include human hearts. In a classical study in the porcine heart at diastolic arrest and vasodilation, Chilian et al. demonstrated that pressure in 80–120 μm vessels has dropped to 60% and 80% of the perfusion pressure in the subendocardium and subepicardium, respectively (Chilian, 1991). VanBavel and Spaan indeed predicted this range of pressures in their network analysis (VanBavel and Spaan, 1992). However, the current human study predicts a median pressure in 100 μm vessels around 32% of systemic pressure, suggesting that far more of the pressure dissipation occurs in vessels much larger than 100 μm (mainly between 200 μm and 1 mm). This could have been caused by arcades and trifurcations in the data. Also, the presence of daughter segments with a larger diameter compared to their mother could have contributed to this finding. The *in silico* data, with a more standardized vascular pattern, suggest that most of the pressure drop occurs in the range of 30 μm to 300 μm.

The hemodynamic parameters reported in this study for a vasodilated arterial network were slightly higher than measurements in human subjects during hyperemia. Flow velocities in the range of 10–30 cm/s are reported in angiographically normal epicardial coronary arteries at rest and 60–100 cm/s at hyperemia and are highly variable between individuals (Kern et al., 1990; Ofili et al., 1995). Flow velocities tend to be lower in the left anterior descending and left circumflex coronary artery compared with the left main coronary artery (Kern et al., 1990). The high flow velocities found in our study were associated with high levels of perfusion (median: 5.6 ml/min/g). Perfusion as measured with positron emission tomography typically increases from 0.6–1.2 ml/min/g at rest to values between 1.9 and 5.0 ml/min/g during hyperemia, with higher values found in females (Sdringola et al., 2011; Murthy et al., 2018). In animal models, regional differences in perfusion were reported with generally equal or higher perfusion at the subendocardium compared to the subepicardium (Feigl, 1983). For the human heart in the present study we found the opposite. Since the simulations were based on data obtained in a diastolic heart, the results resemble hemodynamics in a diastolically arrested heart. Furthermore, the influence of cardiac contraction and myocardial tone were not taken into account in our hemodynamic model. In the beating heart, systolic flow in notably the subendocardium is impaired by the contracting surrounding myocardium (Hoffman and Spaan, 1990). In a model study, Namani et al. showed that not only is flow higher under passive conditions than under autoregulation, but that ignoring the interaction between vessels and the surrounding myocardium indeed results in increased flow and thus perfusion estimates (Namani et al., 2018). Bache et al. found an increase in the subendocardium/subepicardium perfusion ratio with decreasing heart rate at maximal vasodilation (Bache and Cobb, 1977). This together with topology artifacts, ignoring extra resistance in bifurcations or possibly a comparatively low prescribed capillary pressure could have influenced our hemodynamic calculations.

Allometric Description of Topology and Hemodynamics

Allometric (power law) relations have regularly been used to describe relations between physiological and anatomical parameters (Thompson, 1942), including the coronary circulation (Kassab, 2005; Molloi and Wong, 2007; Le et al., 2008; Huo and Kassab, 2009b,a, 2016). The arguably best known relation is "Murray's law" (Murray, 1926) that, based on cost minimization principles, relates flow in a blood vessel to the cube of its diameter. In Poiseuille flow, this relates to wall shear stress being constant along the vasculature. Murray's law certainly is not universally valid, and alternative allometric relations have been derived from various optimality principles, including space-filling requirements (Cohn, 1954; West et al., 1997), relating properties of stems to corresponding crowns (Huo and Kassab, 2009a), optimization of total conductance (Razavi et al., 2014), and application of constructional laws (Miguel, 2016). The postulated scaling exponent typically ranges between 2 and 3.

Our observation of constant cross-sectional area in the larger coronaries is in accordance with several other studies (VanBavel and Spaan, 1992; Mittal et al., 2005b), suggesting an exponent close to 2 rather than 3 for large coronaries. The scaling exponent γ can be derived from area growth by fitting Equation 7 or alternatively by fitting any reformulation of Equation 6. There are various possible optimization strategies, resulting in different estimates for γ, which are furthermore strongly influenced by extreme values. It was therefore difficult to thoroughly quantitate γ based on branching. In general, the scaling exponent increased with decreasing diameters, typically from a value close to 2 for the large segments toward values larger than 3 for small segments. Rivolo et al. also observed the same trend in the porcine heart, with a γ increasing from approximately 2.25 for large vessels to values around 4 for vessels smaller than 100 μm (Rivolo et al., 2016). For the human heart in the present study, the scaling exponent in the diameter-flow relation decreased from 3.21 in the smallest vessels to 2.55 in the major vessels, and shear stress depended biphasically on diameter, having its peak at 630 μm. Van der Giessen et al. found an exponent of 2.55 based on biplanar angiography of human epicardial arteries for the flow-diameter relation (van der Giessen et al., 2011), which matches our results. The exponents in the human heart appear to be higher than the ones observed in porcine hearts. VanBavel and Spaan also described non-constant exponents, increasing from 2.35 for segments larger than 200 μm to 2.82 for diameters smaller than 40 μm (VanBavel and Spaan, 1992). Mittal et al. used morphometric data of the entire porcine coronary arterial tree down to the first capillary branch to conduct hemodynamic analysis and determined a flow–diameter power law relation with exponent 2.2 (Mittal et al., 2005a). Despite these deviations

from Murray's and other invariant scaling laws, downstream conductance scaled with diameter to the power 2.22 over a large range. Common to all invariant allometric relations is that they postulate a general optimality principle. However, as derived by Uylings, different exponents are ideal for different flow types (ranging between 2.33 for turbulent to 3.0 for laminar flow) (Uylings, 1977). Similar effects have been shown for rheological variation (Miguel, 2016) and flow pulsatility (Rivolo et al., 2016). Flow in the coronaries is pulsatile and near-Newtonian whereas laminar, non-pulsatile flow subject to shear-rate dependent viscosity is characteristic for the small vasculature. These differences together with other influences mainly affecting the larger vessels such as areas of low or oscillating wall shear stress (Schoenenberger et al., 2012) and wave reflections (Reneman et al., 2006; Rivolo et al., 2016) may lead to shifting optimal branch relations as we have observed. Altogether, while it is tempting to use allometric descriptors, reality seems a bit more complex and the deviations may lead to substantial differences in physiological parameters such as shear stress and local pressure.

Limitations

A series of image processing steps was required to translate the image stack to a network representation. These included segmentation of the arterial bed, 3D skeletonization, and diameter estimation. This was a major challenge, due to the large difference in vascular diameter between the major branches and the 30 μm smallest vessels that were included. Manual and automated correction was needed. The choices here were based on comparison of the original images to the vascular network representations as well as on common sense. Thus, a few interruptions in cast filling of the major vessels needed to be corrected manually. Very short triangular loops were clearly the result of errors in skeletonization and were pruned to simple paths. Likewise, spurious side branches were removed and some regularization of diameter along vascular paths was included. Since as many as 202,184 segments were included in the final representation, some level of error in the topology and diameters remains unavoidable. However, while it remains necessary to further test and improve the procedures, we do believe that the current work provides an adequate translation from the image stack to the graph representation.

The heart was imaged at 30 μm resolution. Moreover, care was taken not to fill the vessels toward the capillary bed, as this would have resulted in strong background fluorescence. Meanwhile, data on the more distal arterioles were needed for the hemodynamics analysis. We therefore extrapolated branching characteristics when simulating the network toward 5.0–7.5 μm segments. Future work should provide branching characteristics of also the smallest arterioles. While it will not be feasible to fully cover such branching in the whole heart, microscopic data from much smaller tissue samples could be imputed into the simulated networks, improving reliability of the hemodynamic analysis.

The current study is based on a single heart from an elderly patient having atherosclerosis and may not be representative for a normal heart from a person in the same age category or for a healthy young heart. Even though Chen et al. showed in a mice model that the scaling exponent is not affected by aging (Chen et al., 2015), we acknowledge that this may limit the current work. Yet, human hearts rarely become available for this purpose and the whole procedure from filling to graph representation is extremely labor- and computer-intensive. While it will not be feasible to perform studies such as the present one on large numbers of human hearts, inclusion of more hearts is needed to draw conclusions on reproducibility and dependence on age, sex and morbidities. The current study provides a pipeline for doing this work, and with further optimization, automation of the procedures, and improved computer power the inclusion of more samples should become feasible in the near future.

Further limitations of the work include the assumption of Poiseuille flow, the exclusion of the capillary and venous bed in the hemodynamics calculations, and the exclusion of the wave transformation effect. We presume that these assumptions have not substantially altered our main findings. We also were not able to analyze the right coronary artery perfusion territory due to insufficient quality of the vascular filling and subsequent segmentation.

Future Work and Application of the Current Data

An important next step will be the direct quantification of also the most distal vessels, as well as improved routines for image processing and imputation strategies based on a deeper analysis of the data, in addition to extension of the data set.

It has become clear over the years that CAD is not limited to the epicardial vessels. Rather, intra-myocardial arteries and arterioles are also affected, as evidenced by impaired endothelial responsiveness and alterations in vascular structure, caliber and resistance (Crea et al., 2014). Moreover, the vasculature adapts, for better or worse, to the presence of a proximal stenosis and the associated reduced pressure, vascular tone, and hyperemic flow (Siebes et al., 2004; Verhoeff et al., 2005; Sorop et al., 2008). Local perfusion and perfusion reserve are known to be heterogeneous in animal models and healthy humans (Bassingthwaighte et al., 1989; Austin et al., 1990; Chareonthaitawee et al., 2001), with heterogeneity increasing at smaller length scales. Depending on the adaptation of the coronary bed, developing CAD and its effects on the microcirculation may well affect such dispersion of local perfusion and reserve, leading to local ischemic zones. A framework such as presented here could help understanding the relation between microvascular structure and function and the local perfusion and perfusion reserve. We therefore foresee application of the current data and analyses in systems approaches of the coronary circulation, leading to new experimentally testable hypotheses on microvascular adaptation in CAD. In addition, the current study may add to the modeling required *in silico* clinical trials on new drugs and devices, in extension to the current *in silico* work on drug-eluting stents (Karanasiou et al., 2018) and in analogy to work currently done in acute ischemic stroke (Konduri et al., 2018).

Conclusion

We have presented a processing pipeline and extensive data on branching characteristics and predicted hemodynamics of the human coronary circulation. Our findings provide a base for further modeling, including incorporation of vasomotor responsiveness, structural adaptation and their effects on the balance between oxygen demand and supply in health and CAD.

DATA AVAILABILITY STATEMENT

The datasets generated for this study are available on request to the corresponding author.

AUTHOR CONTRIBUTIONS

JS, ML, and EV designed the study. JS, JW, and EV developed the methods and software. JS and ML carried out the study and statistical analysis. All authors critically reviewed the manuscript and approved the final version.

SUPPLEMENTARY MATERIAL

The Supplementary Material for this article can be found online at: https://www.frontiersin.org/articles/10.3389/fphys.2019.01611/full#supplementary-material

REFERENCES

Austin, R. E. Jr., Aldea, G. S., Coggins, D. L., Flynn, A. E., and Hoffman, J. I. (1990). Profound spatial heterogeneity of coronary reserve. Discordance between patterns of resting and maximal myocardial blood flow. *Circ. Res.* 67, 319–331. doi: 10.1161/01.res.67.2.319

Bache, R. J., and Cobb, F. R. (1977). Effect of maximal coronary vasodilation on transmural myocardial perfusion during tachycardia in the awake dog. *Circ. Res.* 41, 648–653. doi: 10.1161/01.res.41.5.648

Bakker, E. N., van der Meulen, E. T., van den Berg, B. M., Everts, V., Spaan, J. A., and VanBavel, E. (2002). Inward remodeling follows chronic vasoconstriction in isolated resistance arteries. *J. Vasc. Res.* 39, 12–20. doi: 10.1159/00004 8989

Bassingthwaighte, J. B., King, R. B., and Roger, S. A. (1989). Fractal nature of regional myocardial blood flow heterogeneity. *Circ. Res.* 65, 578–590. doi: 10.1161/01.res.65.3.578

Bedussi, B., van Lier, M. G., Bartstra, J. W., de Vos, J., Siebes, M., VanBavel, E., et al. (2015). Clearance from the mouse brain by convection of interstitial fluid towards the ventricular system. *Fluids Barriers CNS* 12:23. doi: 10.1186/s12987-015-0019-5

Cardenes, R., Diez, J. L., Duchateau, N., Pashaei, A., and Frangi, A. F. (2013). Model generation of coronary artery bifurcations from CTA and single plane angiography. *Med. Phys.* 40:013701. doi: 10.1118/1.4769118

Cassot, F., Lauwers, F., Lorthois, S., Puwanarajah, P., Cances-Lauwers, V., and Duvernoy, H. (2010). Branching patterns for arterioles and venules of the human cerebral cortex. *Brain Res.* 1313, 62–78. doi: 10.1016/j.brainres.2009.12.007

Chareonthaitawee, P., Kaufmann, P. A., Rimoldi, O., and Camici, P. G. (2001). Heterogeneity of resting and hyperemic myocardial blood flow in healthy humans. *Cardiovasc. Res.* 50, 151–161. doi: 10.1016/s0008-6363(01)00202-4

Chen, X., Niu, P., Niu, X., Shen, W., Duan, F., Ding, L., et al. (2015). Growth, ageing and scaling laws of coronary arterial trees. *J. R. Soc. Interface* 12:20150830. doi: 10.1098/rsif.2015.0830

Chilian, W. M. (1991). Microvascular pressures and resistances in the left ventricular subepicardium and subendocardium. *Circ. Res.* 69, 561–570. doi: 10.1161/01.res.69.3.561

Cohn, D. L. (1954). Optimal systems: I. The vascular system. *Bull. Math. Biophys.* 16, 59–74. doi: 10.1007/bf02481813

Crea, F., Camici, P. G., and Bairey Merz, C. N. (2014). Coronary microvascular dysfunction: an update. *Eur. Heart J.* 35, 1101–1111. doi: 10.1093/eurheartj/eht513

Dole, W. P. (1987). Autoregulation of the coronary circulation. *Prog. Cardiovasc. Dis.* 29, 293–323. doi: 10.1016/s0033-0620(87)80005-1

Feigl, E. O. (1983). Coronary physiology. *Physiol. Rev.* 63, 1–205. doi: 10.1152/physrev.1983.63.1.1

Feng, Y., Wang, X., Fan, T., Li, L., Sun, X., Zhang, W., et al. (2018). Bifurcation asymmetry of small coronary arteries in juvenile and adult mice. *Front. Physiol.* 9:519. doi: 10.3389/fphys.2018.00519

Goodwill, A. G., Dick, G. M., Kiel, A. M., and Tune, J. D. (2017). Regulation of coronary blood flow. *Compr. Physiol.* 7, 321–382. doi: 10.1002/cphy.c160016

Gupta, T., Saini, A., and Sahni, D. (2013). Terminal branching pattern of the right coronary artery in left-dominant hearts: a cadaveric study. *Cardiovasc. Pathol.* 22, 179–182. doi: 10.1016/j.carpath.2012.08.001

Hakimzadeh, N., van Horssen, P., van Lier, M. G., van den Wijngaard, J. P., Belterman, C., Coronel, R., et al. (2014). Detection and quantification methods of monocyte homing in coronary vasculature with an imaging cryomicrotome. *J. Mol. Cell. Cardiol.* 76, 196–204. doi: 10.1016/j.yjmcc.2014.08.019

Hoefer, I. E., den Adel, B., and Daemen, M. J. (2013). Biomechanical factors as triggers of vascular growth. *Cardiovasc. Res.* 99, 276–283. doi: 10.1093/cvr/cvt089

Hoffman, J. I., and Spaan, J. A. (1990). Pressure-flow relations in coronary circulation. *Physiol. Rev.* 70, 331–390. doi: 10.1152/physrev.1990.70.2.331

Huo, Y., and Kassab, G. S. (2009a). A scaling law of vascular volume. *Biophys. J.* 96, 347–353. doi: 10.1016/j.bpj.2008.09.039

Huo, Y., and Kassab, G. S. (2009b). The scaling of blood flow resistance: from a single vessel to the entire distal tree. *Biophys. J.* 96, 339–346. doi: 10.1016/j.bpj.2008.09.038

Huo, Y., and Kassab, G. S. (2016). Scaling laws of coronary circulation in health and disease. *J. Biomech.* 49, 2531–2539. doi: 10.1016/j.jbiomech.2016.01.044

Hutchins, G. M., Miner, M. M., and Boitnott, J. K. (1976). Vessel caliber and branch-angle of human coronary artery branch-points. *Circ. Res.* 38, 572–576. doi: 10.1161/01.res.38.6.572

Kaimovitz, B., Huo, Y., Lanir, Y., and Kassab, G. S. (2008). Diameter asymmetry of porcine coronary arterial trees: structural and functional implications. *Am. J. Physiol. Heart Circ. Physiol.* 294, H714–H723. doi: 10.1152/ajpheart.00818.2007

Kaimovitz, B., Lanir, Y., and Kassab, G. S. (2010). A full 3-D reconstruction of the entire porcine coronary vasculature. *Am. J. Physiol. Heart Circ. Physiol.* 299, H1064–H1076. doi: 10.1152/ajpheart.00151.2010

Kalsho, G., and Kassab, G. S. (2004). Bifurcation asymmetry of the porcine coronary vasculature and its implications on coronary flow heterogeneity. *Am. J. Physiol. Heart Circ. Physiol.* 287, H2493–H2500. doi: 10.1152/ajpheart.00371.2004

Karanasiou, G. S., Tachos, N. S., Sakellarios, A., Conway, C., Pennati, G., Petrini, L., et al. (2018). In silico analysis of stent deployment- effect of stent design. *Conf. Proc. IEEE Eng. Med. Biol. Soc.* 2018, 4567–4570. doi: 10.1109/EMBC.2018.8513205

Kassab, G. S. (2005). Functional hierarchy of coronary circulation: direct evidence of a structure-function relation. *Am. J. Physiol. Heart Circ. Physiol.* 289, H2559–H2565. doi: 10.1152/ajpheart.00561.2005

Kassab, G. S., and Fung, Y. C. (1994). Topology and dimensions of pig coronary capillary network. *Am. J. Physiol.* 267(1 Pt 2), H319–H325. doi: 10.1152/ajpheart.1994.267.1.H319

Kassab, G. S., Le, K. N., and Fung, Y. C. (1999). A hemodynamic analysis of coronary capillary blood flow based on anatomic and distensibility data. *Am. J. Physiol.* 277, H2158–H2166. doi: 10.1152/ajpheart.1999.277.6.H2158

Kassab, G. S., Rider, C. A., Tang, N. J., and Fung, Y. C. (1993). Morphometry of pig coronary arterial trees. *Am. J. Physiol.* 265(1 Pt 2), H350–H365.

Kern, M. J., Tatineni, S., Gudipati, C., Aguirre, F., Ring, M. E., Serota, H., et al. (1990). Regional coronary blood flow velocity and vasodilator reserve in

patients with angiographically normal coronary arteries. *Coron. Artery Dis.* 1, 579–589.

Konduri, P., Bucker, A., Broers, A., Berkhemer, O., Bot, J., Yoo, A., et al. (2018). "Risk factors for infarct growth in patients with acute ischemic stroke," in *Proceedings of the 4th European Stroke Organisation Conference: European Stroke Journal*, Gothenburg, 403.

Le, H. Q., Wong, J. T., and Molloi, S. (2008). Allometric scaling in the coronary arterial system. *Int. J. Cardiovasc. Imaging* 24, 771–781. doi: 10.1007/s10554-008-9303-7

Lee, T. C., Kashyap, R. L., and Chu, C. N. (1994). Building skeleton models via 3-D medial surface axis thinning algorithms. *Comput. Vis. Graph. Image Process.* 56, 462–478. doi: 10.1006/cgip.1994.1042

Medrano-Gracia, P., Ormiston, J., Webster, M., Beier, S., Ellis, C., Wang, C., et al. (2017). A study of coronary bifurcation shape in a normal population. *J. Cardiovasc. Transl. Res.* 10, 82–90. doi: 10.1007/s12265-016-9720-2

Miguel, A. F. (2016). Toward an optimal design principle in symmetric and asymmetric tree flow networks. *J. Theor. Biol.* 389, 101–109. doi: 10.1016/j.jtbi.2015.10.027

Mittal, N., Zhou, Y., Linares, C., Ung, S., Kaimovitz, B., Molloi, S., et al. (2005a). Analysis of blood flow in the entire coronary arterial tree. *Am. J. Physiol. Heart Circ. Physiol.* 289, H439–H446. doi: 10.1152/ajpheart.00730.2004

Mittal, N., Zhou, Y., Ung, S., Linares, C., Molloi, S., and Kassab, G. S. (2005b). A computer reconstruction of the entire coronary arterial tree based on detailed morphometric data. *Ann. Biomed. Eng.* 33, 1015–1026. doi: 10.1007/s10439-005-5758-z

Molloi, S., and Wong, J. T. (2007). Regional blood flow analysis and its relationship with arterial branch lengths and lumen volume in the coronary arterial tree. *Phys. Med. Biol.* 52, 1495–1503. doi: 10.1088/0031-9155/52/5/018

Mosher, P., Ross, J. Jr., McFate, P. A., and Shaw, R. F. (1964). Control of coronary blood flow by an autoregulatory mechanism. *Circ. Res.* 14, 250–259. doi: 10.1161/01.res.14.3.250

Munson, B. R., Okiishi, T. H., Huebsch, W. W., and Rothmayer, A. P. (2013). *Fundamentals of Fluid Mechanics*. Hoboken, NJ: J. Wiley & Sons.

Murray, C. D. (1926). The physiological principle of minimum work: I. The vascular system and the cost of blood volume. *Proc. Natl. Acad. Sci. U.S.A.* 12, 207–214. doi: 10.1073/pnas.12.3.207

Murthy, V. L., Bateman, T. M., Beanlands, R. S., Berman, D. S., Borges-Neto, S., Chareonthaitawee, P., et al. (2018). Clinical quantification of myocardial blood flow using PET: joint position paper of the SNMMI cardiovascular council and the ASNC. *J. Nucl. Med.* 59, 273–293. doi: 10.2967/jnumed.117.201368

Namani, R., Kassab, G. S., and Lanir, Y. (2018). Integrative model of coronary flow in anatomically based vasculature under myogenic, shear, and metabolic regulation. *J. Gen. Physiol.* 150, 145–168. doi: 10.1085/jgp.201711795

Ofili, E. O., Kern, M. J., St Vrain, J. A., Donohue, T. J., Bach, R., al-Joundi, B., et al. (1995). Differential characterization of blood flow, velocity, and vascular resistance between proximal and distal normal epicardial human coronary arteries: analysis by intracoronary Doppler spectral flow velocity. *Am. Heart J.* 130, 37–46. doi: 10.1016/0002-8703(95)90233-3

Ormiston, J. A., Kassab, G., Finet, G., Chatzizisis, Y. S., Foin, N., Mickley, T. J., et al. (2018). Bench testing and coronary artery bifurcations: a consensus document from the European Bifurcation Club. *Eurointervention* 13, e1794–e1803. doi: 10.4244/EIJ-D-17-00270

Palao, T., van Weert, A., de Leeuw, A., de Vos, J., Bakker, E., and van Bavel, E. (2018). Sustained conduction of vasomotor responses in rat mesenteric arteries in a two-compartment in vitro set-up. *Acta Physiol.* 224:e13099. doi: 10.1111/apha.13099

Pries, A. R., Secomb, T. W., Gessner, T., Sperandio, M. B., Gross, J. F., and Gaehtgens, P. (1994). Resistance to blood flow in microvessels in vivo. *Circ. Res.* 75, 904–915. doi: 10.1161/01.res.75.5.904

Razavi, M. S., Shirani, E., Salimpour, M. R., and Kassab, G. S. (2014). Constructal law of vascular trees for facilitation of flow. *PLoS One* 9:e116260. doi: 10.1371/journal.pone.0116260

Reneman, R. S., Arts, T., and Hoeks, A. P. (2006). Wall shear stress–an important determinant of endothelial cell function and structure–in the arterial system in vivo. Discrepancies with theory. *J. Vasc. Res.* 43, 251–269. doi: 10.1159/000091648

Rivolo, S., Hadjilucas, L., Sinclair, M., van Horssen, P., van den Wijngaard, J., Wesolowski, R., et al. (2016). Impact of coronary bifurcation morphology on wave propagation. *Am. J. Physiol. Heart Circ. Physiol.* 311, H855–H870. doi: 10.1152/ajpheart.00130.2016

Schoenenberger, A. W., Urbanek, N., Toggweiler, S., Seelos, R., Jamshidi, P., Resink, T. J., et al. (2012). Deviation from Murray's law is associated with a higher degree of calcification in coronary bifurcations. *Atherosclerosis* 221, 124–130. doi: 10.1016/j.atherosclerosis.2011.12.040

Schwarz, J. C., van Lier, M. G., Bakker, E. N., de Vos, J., Spaan, J. A., VanBavel, E., et al. (2017). Optimization of vascular casting for three-dimensional fluorescence cryo-imaging of collateral vessels in the ischemic rat hindlimb. *Microsc. Microanal.* 23, 77–87. doi: 10.1017/S1431927617000095

Sdringola, S., Johnson, N. P., Kirkeeide, R. L., Cid, E., and Gould, K. L. (2011). Impact of unexpected factors on quantitative myocardial perfusion and coronary flow reserve in young, asymptomatic volunteers. *JACC Cardiovasc. Imaging* 4, 402–412. doi: 10.1016/j.jcmg.2011.02.008

Secomb, T. W., and Pries, A. R. (2013). Blood viscosity in microvessels: experiment and theory. *C. R. Phys.* 14, 470–478. doi: 10.1016/j.crhy.2013.04.002

Seiler, C., Kirkeeide, R. L., and Gould, K. L. (1992). Basic structure-function relations of the epicardial coronary vascular tree. Basis of quantitative coronary arteriography for diffuse coronary artery disease. *Circulation* 85, 1987–2003. doi: 10.1161/01.cir.85.6.1987

Siebes, M., Verhoeff, B. J., Meuwissen, M., de Winter, R. J., Spaan, J. A., and Piek, J. J. (2004). Single-wire pressure and flow velocity measurement to quantify coronary stenosis hemodynamics and effects of percutaneous interventions. *Circulation* 109, 756–762. doi: 10.1161/01.CIR.0000112571.06979.B2

Silvestre, J. S., Smadja, D. M., and Levy, B. I. (2013). Postischemic revascularization: from cellular and molecular mechanisms to clinical applications. *Physiol. Rev.* 93, 1743–1802. doi: 10.1152/physrev.00006.2013

Sorop, O., Merkus, D., de Beer, V. J., Houweling, B., Pistea, A., McFalls, E. O., et al. (2008). Functional and structural adaptations of coronary microvessels distal to a chronic coronary artery stenosis. *Circ. Res.* 102, 795–803. doi: 10.1161/CIRCRESAHA.108.172528

Spaan, J. A., ter Wee, R., van Teeffelen, J. W., Streekstra, G., Siebes, M., Kolyva, C., et al. (2005). Visualisation of intramural coronary vasculature by an imaging cryomicrotome suggests compartmentalisation of myocardial perfusion areas. *Med. Biol. Eng. Comput.* 43, 431–435. doi: 10.1007/bf02344722

Thompson, D. W. (1942). *On Growth and Form*. Cambridge: University Press.

Uylings, H. B. (1977). Optimization of diameters and bifurcation angles in lung and vascular tree structures. *Bull. Math. Biol.* 39, 509–520. doi: 10.1007/bf02461198

van den Wijngaard, J. P., Schulten, H., van Horssen, P., Ter Wee, R. D., Siebes, M., Post, M. J., et al. (2011). Porcine coronary collateral formation in the absence of a pressure gradient remote of the ischemic border zone. *Am. J. Physiol. Heart Circ. Physiol.* 300, H1930–H1937. doi: 10.1152/ajpheart.00403.2010

van der Giessen, A. G., Groen, H. C., Doriot, P. A., de Feyter, P. J., van der Steen, A. F., van de Vosse, F. N., et al. (2011). The influence of boundary conditions on wall shear stress distribution in patients specific coronary trees. *J. Biomech.* 44, 1089–1095. doi: 10.1016/j.jbiomech.2011.01.036

van der Waal, E. C., Mintz, G. S., Garcia-Garcia, H. M., Bui, A. B., Pehlivanova, M., Girasis, C., et al. (2009). Intravascular ultrasound and 3D angle measurements of coronary bifurcations. *Catheter. Cardiovasc. Interv.* 73, 910–916. doi: 10.1002/ccd.21965

van Horssen, P., Siebes, M., Hoefer, I., Spaan, J. A., and van den Wijngaard, J. P. (2010). Improved detection of fluorescently labeled microspheres and vessel architecture with an imaging cryomicrotome. *Med. Biol. Eng. Comput.* 48, 735–744. doi: 10.1007/s11517-010-0652-8

van Horssen, P., van den Wijngaard, J. P., Brandt, M. J., Hoefer, I. E., Spaan, J. A., and Siebes, M. (2014). Perfusion territories subtended by penetrating coronary arteries increase in size and decrease in number toward the subendocardium. *Am. J. Physiol. Heart Circ. Physiol.* 306, H496–H504. doi: 10.1152/ajpheart.00584.2013

van Horssen, P., van Lier, M. G., van den Wijngaard, J. P., VanBavel, E., Hoefer, I. E., Spaan, J. A., et al. (2016). Influence of segmented vessel size due to limited imaging resolution on coronary hyperemic flow prediction from arterial crown volume. *Am. J. Physiol. Heart Circ. Physiol.* 310, H839–H846. doi: 10.1152/ajpheart.00728.2015

van Lier, M. G., Oost, E., Spaan, J. A., van Horssen, P., van der Wal, A. C., vanBavel, E., et al. (2016). Transmural distribution and connectivity of coronary collaterals within the human heart. *Cardiovasc. Pathol.* 25, 405–412. doi: 10.1016/j.carpath.2016.06.004

VanBavel, E., Bakker, E. N., Pistea, A., Sorop, O., and Spaan, J. A. (2006). Mechanics of microvascular remodeling. *Clin. Hemorheol. Microcirc.* 34, 35–41.

VanBavel, E., and Spaan, J. A. (1992). Branching patterns in the porcine coronary arterial tree. Estimation of flow heterogeneity. *Circ. Res.* 71, 1200–1212. doi: 10.1161/01.res.71.5.1200

Verhoeff, B. J., Siebes, M., Meuwissen, M., Atasever, B., Voskuil, M., de Winter, R. J., et al. (2005). Influence of percutaneous coronary intervention on coronary microvascular resistance index. *Circulation* 111, 76–82. doi: 10.1161/01.CIR.0000151610.98409.2F

West, G. B., Brown, J. H., and Enquist, B. J. (1997). A general model for the origin of allometric scaling laws in biology. *Science* 276, 122–126. doi: 10.1126/science.276.5309.122

Wiwatanapataphee, B., Wu, Y. H., Siriapisith, T., and Nuntadilok, B. (2012). Effect of branchings on blood flow in the system of human coronary arteries. *Math. Biosci. Eng.* 9, 199–214. doi: 10.3934/mbe.2012.9.199

Zajaczkowski, M. A., Gajic, A., Kaczynska, A., Zajaczkowski, S., Kobiela, J., Kaminski, R., et al. (2018). Individual variability of vascularization of the anterior papillary muscle within the right ventricle of human heart. *PLoS One* 13:e0205786. doi: 10.1371/journal.pone.0205786

Zamir, M. (1999). On fractal properties of arterial trees. *J. Theor. Biol.* 197, 517–526. doi: 10.1006/jtbi.1998.0892

Zamir, M., and Chee, H. (1986). Branching characteristics of human coronary arteries. *Can. J. Physiol. Pharmacol.* 64, 661–668. doi: 10.1139/y86-109

Zimarino, M., D'Andreamatteo, M., Waksman, R., Epstein, S. E., and De Caterina, R. (2014). The dynamics of the coronary collateral circulation. *Nat. Rev. Cardiol.* 11, 191–197. doi: 10.1038/nrcardio.2013.207

Conflict of Interest: The authors declare that the research was conducted in the absence of any commercial or financial relationships that could be construed as a potential conflict of interest.

Advantages of publishing in Frontiers

OPEN ACCESS
Articles are free to read for greatest visibility and readership

FAST PUBLICATION
Around 90 days from submission to decision

HIGH QUALITY PEER-REVIEW
Rigorous, collaborative, and constructive peer-review

TRANSPARENT PEER-REVIEW
Editors and reviewers acknowledged by name on published articles

Frontiers
Avenue du Tribunal-Fédéral 34
1005 Lausanne | Switzerland

Visit us: www.frontiersin.org
Contact us: frontiersin.org/about/contact

REPRODUCIBILITY OF RESEARCH
Support open data and methods to enhance research reproducibility

DIGITAL PUBLISHING
Articles designed for optimal readership across devices

FOLLOW US
@frontiersin

IMPACT METRICS
Advanced article metrics track visibility across digital media

EXTENSIVE PROMOTION
Marketing and promotion of impactful research

LOOP RESEARCH NETWORK
Our network increases your article's readership